

UC San Diego

Research Theses and Dissertations

Title

Gravity-Driven Intrusions in Stratified Fluids

Permalink

<https://escholarship.org/uc/item/2kc9f99n>

Author

Maurer, Benjamin D.

Publication Date

2011

Peer reviewed

UNIVERSITY OF CALIFORNIA, SAN DIEGO

Gravity-driven intrusions in stratified fluids

A dissertation submitted in partial satisfaction of the
requirements for the degree
Doctor of Philosophy

in

Oceanography

by

Benjamin Dudley Maurer

Committee in charge:

Professor Paul F. Linden, Chair
Professor Sarah T. Gille
Professor W. Ken Melville
Professor Sutanu Sarkar
Professor Kraig B. Winters

2011

UMI Number: 3444438

All rights reserved

INFORMATION TO ALL USERS

The quality of this reproduction is dependent upon the quality of the copy submitted.

In the unlikely event that the author did not send a complete manuscript and there are missing pages, these will be noted. Also, if material had to be removed, a note will indicate the deletion.



UMI 3444438

Copyright 2011 by ProQuest LLC.

All rights reserved. This edition of the work is protected against unauthorized copying under Title 17, United States Code.



ProQuest LLC
789 East Eisenhower Parkway
P.O. Box 1346
Ann Arbor, MI 48106-1346

Copyright
Benjamin Dudley Maurer, 2011
All rights reserved.

The dissertation of Benjamin Dudley Maurer is approved,
and it is acceptable in quality and form for publication
on microfilm and electronically:

Chair

University of California, San Diego

2011

DEDICATION

To my brothers and best friends, Adrian and Grayson.

EPIGRAPH

*From the smallest necessity to the highest religious abstraction,
from the wheel to the skyscraper,
everything we are and everything we have
comes from one attribute of man -
the function of his reasoning mind.
-Ayn Rand*

*To those who do not know mathematics
it is difficult to get across a real feeling
as to the beauty, the deepest beauty, of nature...
If you want to learn about nature, to appreciate nature,
it is necessary to understand the language that she speaks in.
-Richard Feynman*

TABLE OF CONTENTS

Signature Page	iii
Dedication	iv
Epigraph	v
Table of Contents	vi
List of Figures	viii
List of Tables	xvi
Acknowledgements	xvii
Vita and Publications	xix
Abstract of the Dissertation	xx
Chapter 1 Thesis outline and Scope	1
Chapter 2 Introduction	4
2.0.1 Previous work	6
Chapter 3 Intrusion-generated internal waves	11
3.1 Abstract	11
3.2 Introduction	11
3.3 Methods	17
3.3.1 Laboratory Experiments	17
3.3.2 Numerical Simulations	20
3.4 Results	23
3.5 Discussion	33
Chapter 4 Adjacent continuous stratifications	38
4.1 Abstract	38
4.2 Introduction	38
4.3 Model	41
4.4 Methods	44
4.4.1 Laboratory Experiments	44
4.4.2 Numerical Simulations	45
4.5 Results	47
4.6 Role of internal stratification	51
4.7 Discussion and conclusions	56

Chapter 5	Adjacent discrete stratifications	62
5.1	Abstract	62
5.2	Introduction	62
5.3	Model	66
5.4	Methods	69
5.4.1	Numerical simulations	69
5.4.2	Laboratory Experiments	70
5.5	Results	71
5.5.1	Five interleaving interfacial gravity currents . . .	71
5.5.2	Ten interleaving interfacial gravity currents . . .	72
5.6	Discussion	82
Chapter 6	Conclusions and summary of present contribution	87
Bibliography	90

LIST OF FIGURES

Figure 2.1:	Schematic representations of (top to bottom) boundary, interfacial, and intrusive gravity currents. The density of the current ρ_i relative to that of the ambient fluid ρ_a, ρ_L, ρ_U and the stable density structure of the ambient fluid determine the type of gravity current produced. Boundary gravity currents occur when $\rho_i > \rho_a$ or $\rho_i < \rho_a$. Interfacial gravity currents require sharp density interfaces in the ambient fluid and an intrusion density between the densities of the upper and lower layers $\rho_L > \rho_i > \rho_U$. Intrusive gravity currents propagate into continuously stratified environment along an isopycnal where $\rho_i = \rho_a(z_N)$	5
Figure 2.2:	Image of ash cloud from the eruption of the Eyjafjallajökull volcano in Iceland showing multiple gravity-driven intrusions spreading from the volcanic plume, © Ólafur Sigurjónsson [1]. .	7
Figure 3.1:	Schematic showing (above) the initial conditions of lock-release, and (below) the resulting flow. At time, $t = 0$, the lock fluid of density ρ_i is separated by a gate from a linearly stratified ambient fluid of density, $\rho_a(z)$, and buoyancy frequency, N . Once the gate has been removed, the intrusion travels along the level of neutral buoyancy, h , where $\rho_i = \rho_a(z)$ with velocity U	13
Figure 3.2:	Schematic showing the block approximation (following Yih [2]) for the slumping of the lock fluid at time t . The half-height thickness of the gravity current was shown to be accurate for well-mixed intrusions into a linearly stratified ambient by Maurer <i>et al.</i> [3].	14
Figure 3.3:	Images of laboratory experiment ΔN^2 fields overlaid with density field contours at $tN = 15$ for (top to bottom) $h/H = 0.09, 0.21, 0.31, 0.42, 0.47$. The square of the perturbation buoyancy frequency, $\Delta N^2 > 0.90$, is shown in black, and density contours have been drawn every 0.002 g cm^{-3} . The fastest traveling current is $h/H = 0.09$ and the slowest, $h/H = 0.47$	18
Figure 3.4:	Numerical simulation tracer fields overlaid with density field contours at $tN = 15$ for (top to bottom) $h/H = 0.1, 0.2, 0.3, 0.4, 0.5$. Tracer concentration, $C > 95\%$ is shown in white, and density contours are drawn every 0.002 g cm^{-3} . As in the experiments, the fastest current is $h/H = 0.1$, and the slowest is $h/H = 0.5$.	21

Figure 3.5:	A plot of the non-dimensional speeds of the IGCs in experiments (x) and simulations (o). The Bolster <i>et al.</i> [4] theoretical speed (3.4) is plotted for $Fr = 0.266$ (solid line) and $= 0.25$ (dashed line), and theoretical mode-1 (dot-dashed line), mode-2 (dotted line), and mode-3 (gray dotted line) group speeds are also displayed. Note that $h/H \approx 0.3$ represents the intersection between theoretical IGC and mode-2 group speeds, and all intrusions are supercritical to mode-3 group speeds.	24
Figure 3.6:	A plot of the maximum isopycnal displacement versus level of neutral buoyancy, showing both experimental (x) and numerical (o) results. The maximum displacement observed was $\zeta'/H < \frac{1}{3}$, whereas wavelength was too large to be detected, $\lambda \gg L$	25
Figure 3.7:	Intrusions propagating at $h/H = 0.1$ and contours of the upstream ambient density fields for simulations (left) and experiments (right) at $t = 0, 5, 10, 15$ s. Wave motion in the control volume takes the shape of long mode-1 waves.	25
Figure 3.8:	Intrusions propagating at $h/H = 0.3$ and contours of the upstream ambient density fields for simulations (left) and experiments (right) at $t = 0, 5, 10, 15$ s. Wave motion in the control volume takes the shape of long modes 1 and 2 waves.	26
Figure 3.9:	Intrusions propagating at $h/H = 0.5$ and contours of the upstream ambient density fields for simulations (left) and experiments (right) at $t = 0, 5, 10, 15$ s. Wave motion in the control volume takes the shape of long mode-2 waves.	26
Figure 3.10:	$x - t$ diagrams of the non-dimensional cosine decomposition coefficients, \hat{u}/NH , of the numerical simulations for mode-1 (left) and mode-2 (right) and $h/H = 0.1$ (top), $h/H = 0.3$ (middle), $h/H = 0.5$ (bottom). The observed IGC position is plotted by the solid line, while the theoretical wave speed for the relevant mode is overlaid with the dashed line (mode-1) or the dot dashed line (mode-2). Theoretical and observed mode speeds agree well.	28
Figure 3.11:	$x - t$ diagrams of the non-dimensional cosine decomposition coefficients, \hat{u}/NH , of the laboratory experiments for mode-1 (left) and mode-2 (right) and $h/H = 0.09$ (top), $h/H = 0.31$ (middle), and $h/H = 0.47$ (bottom). The observed IGC position is plotted by the solid line, while the theoretical wave speed for the relevant mode is overlaid with the dashed line (mode-1) or the dot dashed line (mode-2). Theoretical and observed mode speeds agree well. The periodic banding in the images is due to surface wave motion.	29

Figure 3.12:	Plots of the horizontally averaged vertical flux of horizontal momentum, $\langle u'w' \rangle$, observed within the upstream control volume in numerical simulations as a function of time and vertical position. The magnitude of the fluxes decreases and the structure of the flux shifts from mode-1 to mode-2 as the level of neutral buoyancy approaches the midplane.	30
Figure 3.13:	Plots of the horizontally averaged vertical flux of horizontal momentum, $\langle u'w' \rangle$, observed within the upstream control volume in laboratory experiments as a function of time and vertical position. The magnitude of the fluxes decreases and the structure of the flux shifts from mode-1 to mode-2 as the level of neutral buoyancy approaches the midplane. Vertical banding in the images is due to surface waves.	31
Figure 3.14:	The ratio of horizontal momentum contained in the upstream waves to the horizontal momentum of the IGC p_{wave}/p_i as a function of time, showing approximately the same amount of momentum in the upstream wave field as in the current.	32
Figure 3.15:	The normalized rate of increase in upstream potential wave energy against the level of neutral buoyancy for experiments (x's) and simulations (o's).	33
Figure 3.16:	The normalized rate of increase in upstream kinetic wave energy against the level of neutral buoyancy for experiments (x's) and simulations (o's).	34
Figure 3.17:	The normalized rate of increase in upstream total wave energy against the level of neutral buoyancy for experiments (x's) and simulations (o's).	34
Figure 4.1:	Schematic showing the initial conditions of lock-release of a linearly stratified intruding fluid of constant buoyancy frequency N_i , into a linearly stratified ambient fluid of buoyancy frequency N_a , where the average densities of both fluids are equal. When the barrier is removed, the intrusion propagates along the level of neutral buoyancy $z_n = H/2$ at a speed that is a function of the stratification ratio $S = N_i^2/N_a^2$	40
Figure 4.2:	Snapshots of the numerical simulations for $S = 0.20$ (left) and $S = 0.80$ (right) for $N_a = 1 \text{ s}^{-1}$ at $N_a t = 10, 20$, and 30 . The dashed gray line denotes the initial position of the gate. The motion of the lock fluid is visualized using a passive tracer. . . .	48
Figure 4.3:	Snapshots of the laboratory experiments for $S = 0.23$ (left) and $S = 0.77$ (right) for $N_a = 1.5 \text{ s}^{-1}$ at the same dimensionless times $N_a t = 10, 20$, and 30 as in figure 4.2. The dashed white line denotes the initial position of the gate. The intrusion fluid is visualized with dye.	49

Figure 4.4:	A comparison between dimensionless intrusion thickness h_i/H , where H is the total fluid depth, as a function of the stratification ratio S for experiments (circles), simulations (crosses) and the thickness assumed in the energy balance model (4.9) (dashed line). The thickness in the experiments was measured at each time as the 10 cm spatial average of intrusion thickness centered 7cm behind the lock gate and the resulting time averages and standard deviations are shown.	49
Figure 4.5:	A comparison between dimensionless intrusive gravity current speed in the experiments (circles), simulations (pluses), and model predictions (curves) as a function of stratification ratio S . The three models of increasing complexity approximate the variation of U_i with S , directly from the potential energy (4.8, dotted line), and scaled by a linear increase in current thickness with S (4.10, dashed line), and incorporating the counterflow (4.13, solid line). U_0 is taken to be the speed of a well-mixed intrusion $U_0 = 0.125N_aH$	50
Figure 4.6:	A comparison of the front shape in laboratory experiments at $N_a = 1.47 \pm 0.02 \text{ s}^{-1}$ for three different stratification ratios, $S = 0, 0.23$ and 0.77 . The presence of stratification within the intrusion generates internal circulation within the intrusion and its thickness increases with increasing S . The shape of an irrotational gravity current given by Benjamin [5] is superimposed on the unstratified intrusion $S = 0$	52
Figure 4.7:	Snapshots of the density contours for $S = 0.20$ and $S = 0.80$ ($N_a = 1 \text{ s}^{-1}$) at $N_at = 5, 10, 15$, and 20 , calculated from the simulation data. The black lines denote density contours evenly spaced across the entire range of intrusion densities, and the corresponding isopycnals in the ambient fluid. The gray lines denote the boundary between the intrusive and the ambient fluids, the black line denotes the initial position of the gate, and the dashed black line denotes the vertical transect described in figure 4.8. Note the pronounced step in the density contours at the transition between the two fluids in the more energetic $S = 0.2$ case, the horizontal gradients in density created within and ahead of the intrusion, and finally the adjustment of the upstream ambient stratification.	54

- Figure 4.8: Vertical transects of the buoyancy frequency, for $S = 0.2$ (left) and $S = 0.8$ (right), taken 5 cm into the ambient fluid from the gate position at $N_a t = 20$ (See figure 4.7). The dash-dotted line and the dotted lines denote the initial buoyancy frequency profiles of the intruding and ambient fluids, N_i and N_a , respectively. The solid line is the instantaneous buoyancy frequency as a function of height at the given x location. Note that the buoyancy frequency of the intruding fluid (closer to the mid-depth) reaches an intermediate value between the N_i and N_a , while the counter-flowing boundary gravity currents also display an increased buoyancy frequency. 55
- Figure 4.9: A comparison between modeled dimensionless intrusive gravity current speed presented in figure 4.5 (dashed line) and speeds predicted based upon a reduced intrusion thicknesses. Energy balance model predictions of intrusion speed where the well-mixed intrusion thicknesses is $0.5H$, $0.4H$, and $0.3H$ ($c = 0.8$ and 0.6) are shown as dashed, dash-dotted, and dotted lines, respectively. Note that relatively large reductions in the thickness of the intrusion results in a less significant increase in predicted speed, and that at lower values of S , this reduced thickness provides an improved fit to the numerical and laboratory data. 59
- Figure 5.1: Schematic showing the initial conditions (above) for a lock-release of a single ‘doubly symmetric’ interfacial gravity current. Here, the ambient fluid is made up of two-layers of equal depth $d = H/2$, and the density of the intruding fluid is the average of the two ambient fluid layer densities $\rho_i = (\rho_L + \rho_U)/2$. At time $t = 0$, the gate is removed, and the IfGC propagates along the interface in the ambient fluids with velocity U (below). The interfacial gravity current is symmetric about the dotted line and behaves as two symmetric boundary currents in a fluid of depth d 64

- Figure 5.2: Schematic showing the initial conditions (above) for a lock-release of ten interleaving interfacial intrusions. In each of the two stably stratified fluids, there are six layers: one of thickness d and five of $2d$. There is a consistent density difference of $\Delta\rho$ between vertically adjacent layers. In the “triply symmetric” case, where $\delta\rho = 0$ each layer density is the average of the densities of its two horizontally adjacent neighbors and there is no bulk density difference between the fluids to the right and left of the gate. We deviate away from this equilibrium case by increasing the density of each of the left-hand fluid layers (left) by a consistent amount $\delta\rho$. At time $t = 0$, the gate is removed, and the layers interleave at constant velocities (below). For the “triply symmetric” case (shown), all currents interleave at the same observed speed. 68
- Figure 5.3: Schematic showing the initial conditions (above) for a lock-release of five interleaving interfacial intrusions. To the left of the gate, there are three layers of thickness $2d$. To the right of the gate, there are two intermediate layers of thickness $2d$ and two-layers at the boundaries of thickness d . There is a consistent density difference of $\Delta\rho$ between vertically adjacent layers. In the “triply symmetric” case, where $\delta\rho = 0$ each layer density is the average of the densities of its two horizontally adjacent neighbors and there is no bulk density difference between the fluids to the right and left of the gate. We deviate away from this equilibrium case by increasing the density of each of the left-hand fluid layers (left) by a consistent amount $\delta\rho$. At time $t = 0$, the gate is removed, and the layers interleave at constant velocities (below). For the “triply symmetric” case (shown), all currents interleave at the same observed speed. 73
- Figure 5.4: Corresponding images from the laboratory experiments and the numerical experiments over the range of $\delta\rho/\Delta\rho$ at $t = 6s$, showing excellent qualitative and quantitative agreement in intrusion shape and evident background shear flow between the experimental results and the numerics. 74

Figure 5.5:	Snapshots of the simulation tracer fields at $t = 7s$. From top to bottom, $\delta\rho/\Delta\rho = [0, 0.05, 0.10, 0.15, 0.20, 0.25, 0.30, 0.35, 0.40, 0.45, 0.50]$. As $\delta\rho/\Delta\rho$ increases, the rightward IfGCs sink relative to the interface along which they propagate, while the leftward propagating IfGCs rise relative to the interface. For intrusions in both directions, the surface of the intruding fluid nearest the interface flattens with increasing density perturbation, while the opposite surface of the intrusion becomes more angled towards the vertical. $\delta\rho/\Delta\rho = 0$ shows interleaving symmetric intrusions of the same velocities in both directions, while $\delta\rho/\Delta\rho = 0.5$ shows step-function profile with height.	76
Figure 5.6:	$x - t$ diagram of the ten $\delta\rho/\Delta\rho = 0.0$ interleaving IfGCs (solid black lines) compared to the theoretical 'triply symmetric' IfGC speed (dashed red lines) predicted from local parameters, $U_{local} = Fr_{\frac{1}{2}} \sqrt{g'_{\Delta} 2d}$ with no background shear flow $u_s = 0$. All five curves in both directions are plotted, but are so close in position that they are indistinguishable.	77
Figure 5.7:	The variation in the observed velocity u_{obs} as a function of the density perturbation $\delta\rho/\Delta\rho$. The theoretical individual current speed U_{local} is marked as the dashed black line. The observed velocity u_{obs} does not display the expected $\sqrt{\delta\rho}$ dependence.	78
Figure 5.8:	Observed velocities u_{obs} of the individual interleaving IfGCs as a function of height. A line is fitted to the IfGC speeds (away from the boundaries) as an estimate of the background shear u_s . The background velocity is observed to increase in magnitude as the difference in the average densities of the two fluids increases. The individual IfGC velocities decrease in their difference from the background shear flow as the density perturbation $\delta\rho/\Delta\rho$ increases.	79
Figure 5.9:	A plot of the fitted shear velocity gradient $\partial u_s / \partial z$ as a function of the density perturbation $\delta\rho/\Delta\rho$. The background shear is observed to vary linearly with the density perturbation.	80
Figure 5.10:	A plot of the fitted shear velocity calculated at $z/H = 0$ (circles) as a function of the density perturbation $\delta\rho/\Delta\rho$. The speed of an analogous gravity current based on (5.1) and the average densities of the two fluids is plotted as a dashed line.	81
Figure 5.11:	A plot of $u_{obs} - u_s$ as a function of $\delta\rho/\Delta\rho$ showing a quadratic decrease in speed with increasing density perturbation.	81

Figure 5.12: Snapshots of the simulation density fields at $t = 7s$, with contour of the passive tracer marking the location of the individual interleaving IfGCs. From top to bottom, $\delta\rho/\Delta\rho = [0, 0.05, 0.10, 0.15, 0.20, 0.25, 0.30, 0.35, 0.40, 0.45, 0.50]$. The “triply symmetric” case shows no displacement of the interfaces. However, simulations of $\delta\rho/\Delta\rho > 0$ show evidence of interfacial waves. The amplitude of these disturbances appears to increase with the density perturbation. 83

LIST OF TABLES

Table 1.1: Scientific contribution of this dissertation.	2
--	---

ACKNOWLEDGEMENTS

Words are not enough to convey my gratitude to the people who have contributed to this work. Nonetheless, I feel I should make what effort I can to thank them here.

I will be forever grateful to Professor Paul Linden. He did not laugh me out of his office in 2003 when, utterly unqualified, I asked to be a part of the graduate MAE program here at the University of California, San Diego. As I've struggled to become something of an engineer, physicist, and oceanographer in the time since, he has supported me as strongly in my failures as in my successes. This has been invaluable. By his example, I am a better scientist, and also a better person. And I am truly thankful for this experience.

I am also deeply indebted to Dr. Claire Debever. She gave me the motivation and courage to become an engineer, and subsequently spent countless selfless and patient hours educating and encouraging me throughout graduate school. She has saved my academic career on innumerable occasions. There is no doubt in my mind that I would not have been able to accomplish this without her.

None of this would have even been a dream had it not been for the love and support of my family. His future children's education was so important to him that my father, Robert, started saving for my college tuition when he was 17 years old. He has only ever loved, encouraged, and supported me as I have tried to understand it all. He also has, to date, given me the best advice I didn't follow: "Get a BS in Applied Mathematics." My mother has never let me convince her that I am anything less than perfect. Her unwavering faith, love, and support have made the difficult times easier. I'm also indebted to my brothers, who consider me the dumbest smart person they know, for their love, levity, and penchant for giving perspective.

I have been fortunate to have supervised some truly exceptional laboratory volunteers, who have advanced my research through their assistance in the laboratory and their insightful questions. I owe gratitude to Matthieu Glatz, Sebastian Romeas, Mathieu Dhinaut, Anson Brune, Alyssa Hardjosokatmoe, Tim Lai, Thiemo Roos, Jessica Lavigne, and Vanessa Lai.

Similarly, I'm grateful for the friendship, support and many illuminating conversations I have had with colleagues. Particularly, Diogo Bolster, in whose footsteps I've closely followed (they say mockery...), Morris Flynn, for his unabated interest in all things gravity-current-related, Stuart Dalziel, for his essential technical expertise, and Bruce Sutherland, whose encouragement, insight, and enthusiasm has literally kept me in the field.

I would also like to thank my doctoral committee members. Professors Gille, Melville, Sarkar, and Winters, who have taken the time from their outstandingly busy schedules to contribute to my academic and professional advancement. I have been flattered by their participation, and have benefited from their insight and attention.

Significant improvements were made to the clarity and coherence of this document through careful editing by Katarzyna Matusik, Dr. Claire Debever, Kara Moriarty, and Professor Sarah Gille. This is tedious work, and I very much appreciate their substantial efforts.

Finally, I would like to thank the friends I have made here at and though UC, San Diego. The memories I have from the relationships we've built are very, very dear to me. Too many are too important for me to list them all here.

Chapter 4 has been published in the *Journal of Fluid Mechanics*, ('Intrusive gravity currents between two stably stratified fluids', 2010, B. D. Maurer, D. T. Bolster, and P. F. Linden (Cambridge University Press) [3]. We also intend to submit chapters 3 and 5 to the *Journal of Fluid Mechanics*. I am the principal investigator and lead author for each of the papers described above.

VITA

1980	Born Sacramento, California
2001	B. A. in Philosophy, University of California, San Diego
2001	B. S. in Biology: Ecology Behavior, and Evolution, University of California, San Diego
2000-2003	Biological Technician, Southwest Fisheries Science Center, La Jolla
2004-2005	Trainee, California Sea Grant, Scripps Institution of Oceanography
2006	M. S. in Applied Ocean Sciences, Department of Mechanical and Aerospace Engineering, University of California, San Diego
2007	Visiting Scholar, Tokyo University of Marine Science and Technology, Tokyo, Japan
2007-2008	Graduate Teaching Assistant, University of California, San Diego
2011	Ph. D. in Oceanography, Scripps Institution of Oceanography

PUBLICATIONS

B.D. Maurer, D. Bolster, P.F. Linden “Intrusions in Adjacent Stratified Fluids”, *J. of Fluid Mech.*, 647, 53-69, 2007.

Conti, S.G., Roux, P., Fauvel, C., Maurer, B. D., and Demer, D.A. “Acoustical monitoring of fish density behavior, and growth rate in a tank”, *Aquaculture*, 626590, 2005.

Conti, S.G., Roux, P., Fauvel, C., Maurer, B. D., Demer, D.A., and Waters, K.R. “Acoustical monitoring of fish behavior in a tank”, *Journal of the Acoustical Society of America*, 116, 2489, 2004.

ABSTRACT OF THE DISSERTATION

Gravity-driven intrusions in stratified fluids

by

Benjamin Dudley Maurer

Doctor of Philosophy in Oceanography

University of California, San Diego, 2011

Professor Paul F. Linden, Chair

All natural fluids stratify. Stable stratifications, in which isobars and isopycnals are parallel, are capable of supporting internal wave motion. Unstable stratification, in which density and pressure gradients are not aligned, results in gravity-driven flow. Gravity currents are a subset of these flows in which horizontal density gradients sharpen and propagate horizontally, transporting mass, momentum, and energy. If the density of the gravity current is within the density extrema of the stably stratified ambient fluid, it propagates as an intrusion at an intermediate height. Through laboratory experiments and numerical simulations, this dissertation explores the influence of stratification on the dynamics of gravity-driven intrusions.

Intrusions require stable stratification in the ambient fluid, which is capable of transporting momentum and energy away from the current in the form of internal waves. We investigate the constant velocity propagation of well-mixed intrusions propagating into a linearly stratified ambient fluid. Varying the level of neutral buoyancy, we quantify the corresponding variation in structure, momentum, and energy of the upstream wave field.

Adjacent stable stratifications of differing vertical density structure necessarily entail horizontal density gradients. These gradients determine the hydrostatic pressure differences driving the ensuing gravity current. We examine the mid-depth, constant velocity propagation of one linearly stratified fluid into another more strongly linearly stratified fluid. Working from the available potential energy of the system and measurements of the intrusion thickness, we develop an energy model to describe the speed of the intrusion in terms of the ratio of the two buoyancy frequencies.

Distinct from adjacent linear stratifications, adjacent discrete stratifications may create flow consisting of interleaving intrusions. Single intrusions into a two-layer ambient fluid are well understood. Limiting our study to an idealized system of multiple intrusions, we attempt to extend the two-layer model to describe the interleaving process. We show that this simple extension fails when the average densities of the two stratifications are unequal, and suggest that this failure is due to the coupling of interfacial waves across constant density layers.

Chapter 1

Thesis outline and Scope

This document describes a subset of research projects I have engaged in as a doctoral student at Scripps Institution of Oceanography. Throughout my tenure, I have worked on a wide variety of problems, including designing calibration protocols for glider-mounted oceanographic instrumentation, developing real-time visualization tools for tow-yo CTD data, conducting *in situ* measurements of ocean water viscosity, processing ocean turbulence microstructure data, and developing and deploying a novel deep sea instrument-mounted video system. However, I feel my most significant scientific contribution has been to the understanding of buoyancy driven flow, specifically the role of stratification in gravity current dynamics. This dissertation describes much of that work, focusing on three broad issues: the generation of waves by buoyancy driven intrusions, the role of stratification in the intruding fluid, and the interleaving of multiple intrusions.

Chapter 3 describes the generation of internal waves by well-mixed intrusive gravity currents propagating at a constant velocity into a linearly stratified ambient fluid. Internal waves are relevant to intrusion dynamics as upstream density perturbations change the local pressure differences experienced by the front and the generation of these perturbations represents a transfer of energy from the current. A range of intrusion propagation heights is investigated for the consequent effect on the structure, momentum, and energy of the wave field generated upstream. Measurements of the internal wave field within this control volume are made from synthetic schlieren laboratory experiments and numerical simulations, and the rate of energy transfer to upstream waves is calculated from linear theory.

Chapter 4 develops a model for the dynamics of an intrusive gravity current driven by two adjacent linearly stratified fluids. Ours is the first investigation we are aware of describing a continuously stratified intrusive gravity current propagating

Table 1.1: Scientific contribution of this dissertation.

Chapter	Journal	Status	Co-Author
3	<i>Journal of Fluid Mechanics</i>	To be submitted	P. F. Linden
4	<i>Journal of Fluid Mechanics</i>	Published	P. F. Linden D. B. Bolster
5	<i>Journal of Fluid Mechanics</i>	To be submitted	P. F. Linden

into a continuously stratified ambient fluid. In the spirit of Cheong *et al.* [6] and Bolster *et al.* [4], dimensional and energy scaling arguments form the basis of a model which is subsequently compared to results from laboratory experiments and numerical simulations. The role of internal stratification within the front is also investigated, and intrusion velocity model is adjusted to account for a dependence on intrusion thickness.

Chapter 5 presents investigations into the interleaving of multiple interfacial gravity currents driven by adjacent discretely stratified fluids. To the best of our knowledge this is the first study to address multiple interleaving interfacial gravity currents. We extend Cheong *et al.*'s [6] model of a single interfacial current to a highly idealized case of interleaving interfacial intrusions. Measurements of the individual current speed from numerical experiments show poor agreement with the two-layer model. We explain the observed discrepancies between the model and our observed results.

Chapter 4 has been published as a journal article, and is reproduced here with minor alterations to improve continuity. Chapters 3 and 5 are intended for publication, and have been written in the style of stand-alone chapters in preparation for submission.

All work presented herein is my own, with the exception of numerical simulations described in chapter 4, which were run by Diogo Bolster, a graduate of the Linden lab whose tenure overlapped mine for a few months. Though Dr. Bolster ran the simulations, I performed all of the post-processing of the data. All other numerical simulations described in this work were set up, run, and processed

solely by me. I also received substantial aid in the execution of laboratory experiments from undergraduate and graduate student volunteers. However, I solely designed, supervised, and interpreted all laboratory experiments presented in this disseration.

Chapter 2

Introduction

Density variations in a gravitational field generate motion except in the special case when the stratification is vertical. Any horizontal variation in density will lead to baroclinic generation of vorticity ($\nabla p \times \nabla \rho \neq 0$) and a gravity-driven flow will ensue.

The most well-known form is a gravity current – a sharp density front that propagates horizontally transporting mass, momentum, and energy along a boundary or isopycnal surface. Simpson & Linden [7] showed that a non-uniform horizontal gradient always sharpen into a gravity current front as the flow evolves in time. This frontogenesis occurs because the baroclinic torque driving the flow is proportional to $|\nabla \rho|$, and therefore larger density gradients travel more rapidly, overtaking smaller gradients and sharpening the front.

Gravity currents propagate along a level of neutral buoyancy, an isopycnal surface of a density equivalent to that of the current. Gravity currents that are heavier or lighter than the ambient fluid propagate along lower or upper surfaces as *boundary* gravity currents. *Intrusions* are those currents that travel along a level of neutral buoyancy at an intermediate height within the ambient fluid. Within this document, intrusions are further divided into *interfacial* gravity currents (IfGCs) which propagate along sharp density interfaces (chapter 5), and *intrusive* gravity currents (IGCs) which propagate at an intermediate depth within a continuously stratified fluid (chapters 3 and 4). Schematics of these flows are presented in figure 2.1.

Gravity-driven intrusions exist only in stratified ambient fluids. Perturbations to the stable stratification of the ambient fluid by the intruding fluid have the potential to propagate away from the intrusion as interfacial or internal waves. In doing so they extract momentum and energy from the current and modify the local

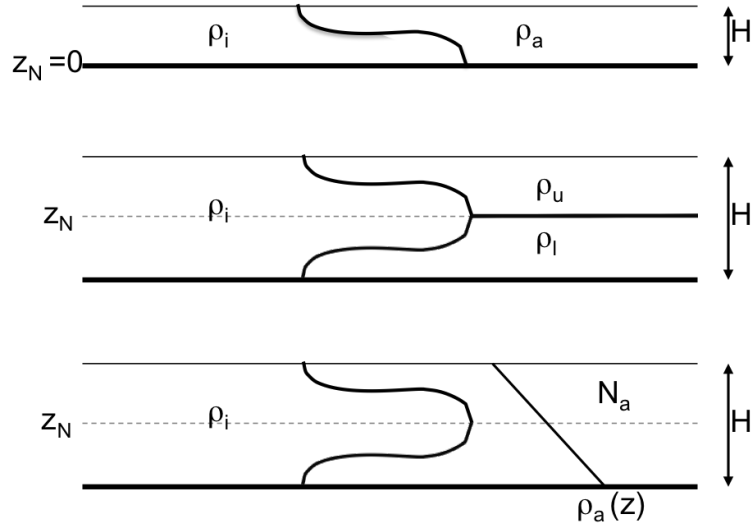


Figure 2.1: Schematic representations of (top to bottom) boundary, interfacial, and intrusive gravity currents. The density of the current ρ_i relative to that of the ambient fluid ρ_a , ρ_L , ρ_U and the stable density structure of the ambient fluid determine the type of gravity current produced. Boundary gravity currents occur when $\rho_i > \rho_a$ or $\rho_i < \rho_a$. Interfacial gravity currents require sharp density interfaces in the ambient fluid and an intrusion density between the densities of the upper and lower layers $\rho_L > \rho_i > \rho_U$. Intrusive gravity currents propagate into continuously stratified environment along an isopycnal where $\rho_i = \rho_a(z_N)$.

environment into which they advance. Chapter 3 explores this transfer of momentum and energy, while chapter 5 highlights the effect of modifying the upstream conditions on the dynamics of the intrusion.

Stratification *within* gravity-driven intrusions also affects the dynamics of the flow. Relative to the well-mixed case, vertical density gradients within an intrusion necessarily decrease horizontal density gradients across the gravity current front, (this is not necessarily true for a boundary current). In turn, this decreases the baroclinic generation of vorticity. This is discussed further in chapter 4.

Intrusions have applications in geophysical, environmental and industrial flows over a wide range of scales. In the ocean, Mediterranean mode water intruding into the Atlantic has spatial scales of hundreds of kilometers horizontally and hundreds of meters vertically. Intrusions along ocean front can occur at vertical scales of a few meters and propagate for a few kilometers (Georgi [8], Alford *et al.* [9]). These intrusions are believed to be responsible for much of the ageostrophic cross-front transport of mass (Griffiths & Hopfinger [10]). In addition to advecting mass (and therefore momentum and energy), intrusions transport sediments, nutrients, and biological material. Sharpening density fronts concentrate these particulates, such as phytoplankton or particulate organic matter in the ocean or locusts or moths in the atmosphere (Simpson [11]).

Gravity-driven intrusions made world news in 2010 with the eruption of Eyjafjallajökull volcano in Iceland. Ash from the volcano rose to a level of neutral buoyancy in the atmosphere as a plume before propagated as a gravity-driven intrusion advected by atmospheric winds in the troposphere (see figure 2.2). This disaster had an enormous economic impact, periodically disrupting air travel across Europe for more than three months.

2.0.1 Previous work

The study of gravity-driven intrusions began with Wu's [12] work in 1969 on the collapse of a mixed region in a stratified fluid. The authors noted that the collapse generated internal waves, studied in more detail later by Amen & Maxworthy [13]. Early experiments of intrusions of constant flux input at their level



Figure 2.2: Image of ash cloud from the eruption of the Eyjafjallajökull volcano in Iceland showing multiple gravity-driven intrusions spreading from the volcanic plume, © Ólafur Sigurjónsson [1].

of neutral buoyancy in a continuously stratified ambient fluid were performed by Manins [14] in 1973, who observed that under these conditions the front propagated at a constant speed. He further showed that this constant speed scaled as a constant Froude number dependent on the buoyancy frequency of the ambient fluid and the thickness of the intrusion. A numerical study in by Kao *et al.* (1978) [15] yielded similar results.

The first theoretical descriptions of intrusions were of interfacial gravity currents. In the style of Benjamin’s [5] (1968) work on constant density boundary gravity currents, Holyer & Huppert (1980) [16] constructed an analytical model by balancing mass, momentum, and energy in a control volume moving at the speed of the current. Their model, however, was shown to be accurate only over a narrow range of parameters by Sutherland *et al.* (2004) [17], who attribute the discrepancy to Holyer & Hupperts neglecting of variations in the upstream conditions.

In the laboratory and numerically, intrusions are often studied in the context of lock-releases, in which a vertical barrier between two fluids of differing stable stratifications is removed, allowing the baroclinic generation of vorticity to drive an intrusion of one fluid along an isopycnal of the other. As with unstratified boundary currents (see Rottman & Simpson [18]), after a brief period of acceleration the initial constant velocity phase of the resulting flow (see e.g. Lowe *et al.* [19]) is comparable to a current supplied by a constant flux of fluid as in Manins’ experiments.

Results from lock-release experiments by Britter & Simpson (1981) [20] and later by de Rooij *et al.* (1999) [21] hinted at the reason Holyer & Huppert’s model was not accurate over a wider range. Britter & Simpson showed that when the current density is the average of the layer densities and the heights of the layers are equivalent, there is no upstream (in the frame of reference of the current) disturbance of the interface. Work by de Rooij *et al.* showed that any break in this symmetry, either by perturbing the density of the IfGC from the average of the layer densities or making the layer depths unequal, upstream interfacial waves are excited by the intrusion.

The first interfacial gravity current model to accurately predict IfGC speed

over a wide range of intrusion densities and layer thicknesses was constructed by Cheong *et al.* in 2006. In the spirit of Yih (1965) [2], the authors calculated the Available Potential Energy (APE) of a lock release system as the hydrostatic pressure difference between fluids (reproduced formally in chapters 3 and 4). Scaling the velocity of the current by the APE and fitting the appropriate limits, Cheong *et al.* heuristically developed a prediction of IfGC speed that was shown to be accurate over the parameter space. The authors noted that the amplitude of the upstream wave was proportional to the departure from the equilibrium conditions of Britter & Simpsons’s experiments.

In the same year, Flynn & Linden [22] developed the first analytic model to accurately predict the propagation of IfGCs in a two-layer fluid. Similar to Holyer & Huppert, the authors employed a Benjamin-style approach, balancing mass, momentum, and energy over a control volume in which the current was stationary. Contrary to previous analyses, however, Flynn & Linden included the deflection of the interface in this balance. Their model admits a physical solution for nearly the entire parameter space, and explains the limited accuracy of models that neglect the upstream wave.

A heuristic model similar to that of Cheong *et al.*, was developed by Bolster *et al.* (2008) who predicted the front speed of well-mixed intrusive gravity currents in a stratified ambient fluid of constant buoyancy frequency. The authors scaled the velocity of intrusions by the Available Potential Energy of the lock-release as it varied with the level of neutral buoyancy. Extending work by Maxworthy *et al.* (2002) [23] on well-mixed boundary currents in a constantly stratified ambient fluid, Bolster *et al.* were able to determine the appropriate limits. As with Cheong *et al.*’s work, the predictions are accurate over the parameter space.

Ungarish & Huppert (2004) [24] show that the primary effect of linear stratification in the ambient fluid is to alter horizontal density gradients across the front, reducing the baroclinic torque available to the flow relative to the unstratified case. Though boundary gravity currents and gravity-driven intrusions do excite internal waves in the ambient stratification, they represent an insignificant portion of the APE (see e.g. Maxworthy *et al.* (2002) [23], Sutherland *et al.* (2007) [25],

Monroe *et al.* (2009)). This result is reflected in the accuracy of APE-scaled models, such as Cheong *et al.*, Bolster *et al.*, and chapter 4 of this dissertation. The significant impact of these waves is instead the modification of the upstream conditions into which the gravity currents propagate. Supercritical waves displace isopycnals ahead of the current, modifying the baroclinic generation of vorticity at the front and thereby modifying the speed of the current. While this has been shown explicitly for interfacial gravity currents (Cheong *et al.* (2006), Flynn & Linden (2006)), it has yet to be proven for intrusive gravity currents.

Using a combination of laboratory experiments and numerical simulations, this dissertation explores the dynamics of constant velocity gravity-driven intrusions in stratified fluids, limiting our focus to intrusions in which the dynamics are governed by the balance of buoyancy and inertial forces. Chapter 3 reports measurements of the internal wave field generated upstream of well-mixed intrusive gravity currents in a constantly stratified ambient fluid. Chapter 4 describes the role of linear stratification in both the ambient and the intruding fluid in the speed of intrusive gravity currents as it relates to the APE of the system and the resulting front speed. And finally, chapter 5 presents our findings on the front speeds of multiple interleaving, interfacial gravity currents.

Chapter 3

Intrusion-generated internal waves

3.1 Abstract

We present an experimental and numerical study of the upstream internal wave field generated by well-mixed intrusive gravity currents (IGCs) propagating into a uniformly stratified ambient fluid during the constant velocity phase of translation. Using synthetic schlieren imaging laboratory techniques and direct numerical simulations, we quantify the wave motion ahead of IGCs traveling at various levels of neutral buoyancy within the ambient stratified fluid. We show that this level of IGC propagation strongly influences the forcing of particular supercritical long-wave modes, and we estimate the associated momentum and energy flux into the upstream wave field. The momentum of the upstream wave field is found to be approximately equal to the momentum within the IGC. The energy flux into the upstream wave field is found to be five to fifteen percent of the rate of Available Potential Energy (APE) transfer into the kinetic energy of the IGC.

3.2 Introduction

Horizontal pressure gradients in a fluid drive flow. Horizontal density gradients in a fluid subject to only gravitational body forces create horizontal pressure gradients. Any non-constant horizontal gradient in fluid density drives a gravity or density current (Simpson & Linden [7]), which takes the shape of a sharply defined front propagating horizontally along a boundary or an isopycnal in ambient fluid.

These currents are referred to as boundary gravity currents (BGCs) or intrusive gravity currents (IGCs), respectively, and represent the transfer of the potential energy stored in horizontal density gradient to the kinetic energy of the propagating current as the fluid re-stratifies to a stable vertical density gradient. In this process, energy is also transferred to wave generation and turbulent dissipation.

This study aims to understand the structure and energetics of upstream internal wave motion generated by high Reynolds number, Boussinesq intrusive gravity currents in a linearly stratified ambient fluid during the initial constant velocity phase of propagation. The Reynolds number can be estimated by the ambient fluid parameters H , the total fluid height, and $N = \sqrt{-\frac{g}{\rho_0} \frac{\partial \rho}{\partial z}}$, the buoyancy frequency, such that $Re_{ambient} = NH^2/\nu$; or by the intruding fluid motion as $Re_{intrusion} = U(H^2/2)/\nu$, where U is the velocity of the intrusion, and ν is the kinematic viscosity. Boundary gravity currents are considered inertial for Reynolds numbers in excess of 500 to 1000 [26].

It is convenient to study gravity currents in the context of a lock release in a rectangular channel, where a vertical gate at L_{lock} initially separates two fluids of height H and densities ρ_i of the intruding lock fluid and $\rho_a(z)$ of the ambient fluid (see Figure 3.1), where z increases upwards from 0 to the total fluid height, H , and x increases rightward from the lock endwall at 0 to the ambient endwall at L . In a channel lock release, cross-channel variations are assumed to be much smaller than streamwise variations, and the flow is therefore considered two-dimensional.

Prior to the removal of the lock gate, all of the energy in the system is stored in the potential energy of the hydrostatic pressure difference between the adjacent fluids. This difference over the height of the fluid determines the initial available potential energy (APE) per area of the system,

$$E_{APE} = g \int_0^H (\rho_i - \rho_a) z dz. \quad (3.1)$$

The gate is then removed at time $t = 0$ and these horizontal pressure differences drive a gravity current into the ambient fluid. If $\rho_i \geq \rho_a(z = H)$ or $\rho_i \leq \rho_a(z = 0)$, results in a BGC. Alternatively, if $\rho_a(z = 0) < \rho_i < \rho_a(z = H)$, then the resulting flow is an IGC propagating along the level of neutral buoyancy, the isopycnal where $\rho_i = \rho_a(h)$ (shown in figure 3.1). After a brief period of acceleration, the gravity

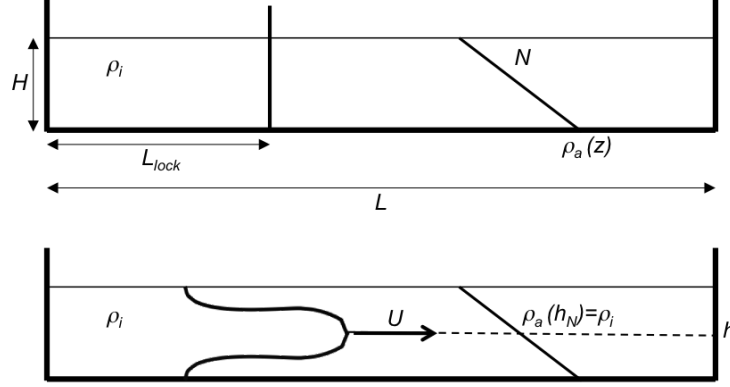


Figure 3.1: Schematic showing (above) the initial conditions of lock-release, and (below) the resulting flow. At time, $t = 0$, the lock fluid of density ρ_i is separated by a gate from a linearly stratified ambient fluid of density, $\rho_a(z)$, and buoyancy frequency, N . Once the gate has been removed, the intrusion travels along the level of neutral buoyancy, h , where $\rho_i = \rho_a(z)$ with velocity U .

current travels at a constant speed, U , until the finite volume of lock fluid becomes relevant to the flow (Rottman & Simpson [18]).

For a well-mixed gravity current propagating at a constant speed into a linearly stratified ambient fluid of height H and a buoyancy frequency N non-dimensional analysis suggest that the current speed be related to these parameters by a constant Froude number (Simpson [11]),

$$U = Fr_0 NH. \quad (3.2)$$

A study by Maxworthy *et al.* [23] found that a boundary gravity current of density $\rho_i = \rho_a(z = 0)$ in a linearly stratified fluid travels at $Fr_0 = 0.25$. These findings were corroborated by Ungarish & Huppert [27] who empirically found $Fr_0 = 0.266$.

Bolster *et al.* [4] extended this analysis to intrusive gravity currents. The authors reasoned that an IGC along $z = H/2$ can be thought of as two symmetric BGCs, reflected about the the midplane of the experiment, and each in fluid of depth $H/2$. In this equilibrium case, $U = \frac{Fr_0}{2} NH$ the authors found that the Froude number does indeed scale accordingly: $Fr = \frac{Fr_0}{2} = 0.125$. Expanding away from the equilibrium case, they noted that the APE of lock releases of a well

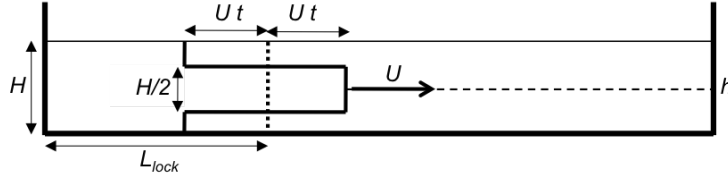


Figure 3.2: Schematic showing the block approximation (following Yih [2]) for the slumping of the lock fluid at time t . The half-height thickness of the gravity current was shown to be accurate for well-mixed intrusions into a linearly stratified ambient by Maurer *et al.* [3].

mixed fluid into a linearly stratified ambient is quadratic in h/H ,

$$E_{APE} = \frac{1}{3} \left((\rho_a(0) - \rho_i)gh^2 + (\rho_i - \rho_a(H))g(H - h)^2 \right). \quad (3.3)$$

Assuming a perfect conversion of APE to the kinetic energy (KE) of the current, Bolster *et al.* [4], fit U^2 to a quadratic expression in h , heuristically determining an expression for gravity current speed in terms of the boundary current Froude number,

$$U = \frac{1}{2}Fr_0 \left(12 \left(\frac{h - \frac{1}{2}H}{H} \right)^2 + 1 \right)^{1/2} NH, \quad (3.4)$$

where $Fr_0 \approx 0.25$, the value from boundary gravity currents. At the limits where $h = H/2$ and $h = 0, H$, the expression for Fr above yields the accepted values $Fr = 0.125$ and 0.25 , respectively. This expression was confirmed through recent experiments and simulations by Monroe *et al.* [28].

The shape and advancement of the current can be estimated from these velocities using an approach introduced by [2], illustrated in Figure 3.2. Well-mixed IGCs into a linearly stratified ambient fluid occupy approximately $H/2$, (Maurer *et al.*[3]). Approximating the intrusion to first order by blocks of fluid, continuity implies that the rate of horizontal advancement U is equivalent to rate of slumping of the lock fluid when the current occupies half the depth of the channel. The momentum of the current can therefore be estimated as,

$$p_i = 2Ut \frac{H}{2} \rho_i U. \quad (3.5)$$

Similarly, the rate of conversion of available potential energy can be estimated as,

$$\frac{d}{dt} \int_{L_{lockt}+Ut}^{L_{lock}-Ut} E_{APE} dx = -2E_{APE}U. \quad (3.6)$$

A stratified ambient fluid is capable of supporting internal wave motion. Indeed, internal wave motion generation by gravity currents has been observed in a number of studies (e.g. Wu [12], Schooley & Hughes [29], Maxworthy *et al.* [23], Sutherland *et al.* [30], White & Helfrich [31], Monroe *et al.* [28]). From the dispersion relation, the angle of wave propagation, θ , relative to the horizontal is defined by $\sin \theta = \omega/N$, where ω is the forcing frequency. The non-periodic upstream motion of a propagating gravity current can be viewed as forcing the wave field at $\omega \approx 0$, from its position at h , with a thickness of $H/2$. In section 3.4, we show that the waves generated are linear, and as such, these disturbances travel upstream in a constantly stratified fluid at

$$c_{g,m}/NH = \frac{1}{m\pi}, m = 1, 2, 3... \quad (3.7)$$

the horizontally propagating internal long-wave group speed.

Both group speed and Froude number vary linearly with NH . As $c_{g,1}/NH = 1/\pi > Fr(h=0, H) = 1/4$, all gravity currents for which $\rho_a(z=H) < \rho_i < \rho_a(z=0)$ are subcritical to mode-1 internal wave propagation. Indeed, Maxworthy *et al.* [23] and White & Helfrich [31] noted strong interactions between the boundary gravity currents where $\rho_i = \rho_a(z=0)$ and the supercritical mode-1 internal waves they generate. As noted by Bolster *et al.* [4], the slowest intrusions, those near the half-height of the fluid, propagate at $Fr \approx 0.125$, which is subcritical to mode-2 internal waves, $c_{g,2}/NH = 1/2\pi$. All intrusions of well mixed fluid into a constantly stratified ambient travel faster than mode-3 linear internal waves (see figure 3.5 which reproduces results from Bolster *et al.* [4]).

The generation of internal wave motion represents a transfer of energy from the kinetic energy of the current. The energy contained in the upstream wave field, E_{wave} is a combination of potential energy $E_{P,wave}$ and kinetic energy $E_{K,wave}$.

According to linear internal wave theory,

$$E_{wave} = E_{P,wave} + E_{K,wave}, \quad (3.8)$$

$$E_{P,wave} = \frac{1}{2}\rho_0 N^2 \zeta'^2, \quad (3.9)$$

$$E_{K,wave} = \frac{1}{2}\rho_0(u'^2 + w'^2). \quad (3.10)$$

where ζ' , u' , and w' are the vertical density displacement, horizontal velocity, and vertical velocity perturbations due to wave motion.

We limit our investigation to internal wave motion within a control volume upstream of intrusive gravity currents. This control volume is defined by the advancing front of the current, the upstream boundaries of the tank or numerical domain and the bottom and top surfaces of the fluid. All observations are conducted in a time window from $t = 0$, the time when the fluid is set into motion, to $t = (L - L_{lock})/c_{g,1}$, the time at which mode-1 perturbations reach the upstream endwall. Because there is no background flow, any perturbations to the upstream density or velocity fields can be attributed to wave motion, and the shrinking spatial dimensions of the control volume do not introduce a bias.

This study deviates from previous work by Monroe *et al.* [28], which focused on the internal waves generated by interactions with the lock endwall in finite volume lock releases. In this work, the length and aspect ratio of the lock is set such that wave motion reflected from within the lock has insufficient time to reach the upstream control volume. We therefore characterize and quantify the wave field generated only by the constant motion of the intrusive gravity current itself. As in Monroe *et al.* [28], however, we also investigate the effect of h over half of the possible range: $0 < h < H/2$, assuming symmetry of dynamics about the midplane of the experiment since the flow is Boussinesq.

In section 3.3, we describe our synthetic schlieren laboratory experiments and two-dimensional direct numeric simulation methodology. We present the observed structure and propagation speed of the internal wave field as well as the associated momentum and energy within the control volume in section 3.4. In section 3.5, we present our conclusions and discuss the implications of this study for current models of propagation of well-mixed intrusive gravity currents into a

linearly stratified ambient fluid and future analytical work.

3.3 Methods

3.3.1 Laboratory Experiments

Laboratory experiments were conducted in a channel with an ambient fluid of constant stratification, $N = 0.96 \pm 0.01 \text{ s}^{-1}$ and five values of neutral buoyancy levels $h/H = \{0.09, 0.21, 0.31, 0.42, 0.47\} \pm 0.02$. The minimum Reynolds number for these flows were $Re_{ambient} \geq 3.8 \times 10^4$ and $Re_{intrusion}(h/H = 0.47) = 2.8 \times 10^3$.

The experimental channel made of transparent 1cm thick acrylic was 183cm long, 23 cm wide, and 30 cm high. The channel was filled to $H = 20 \pm 0.1 \text{ cm}$ with densities ranging from 1.009 and 1.029 g cm^{-3} using the double bucket method (Oster [32]) and sponge floats to create linear stratification. Sodium chloride was added to the water to manipulate fluid density (Schmidt number, $Sc \approx 10^3$).

Once the tank had been linearly stratified, it was divided by adding a vertical gate at a distance $L_{lock} = 40 \text{ cm}$ from the lock endwall. The position of the gate was chosen at a lock aspect ratio of $L_{lock}/H \geq 2$ in order to maximize the internal wave formation and propagation distance within the ambient fluid before being affected by waves reflected from either endwall. With the gate in place, the lock fluid was stirred to homogenize the density ρ_i . To vary h away from the equilibrium case, $h/H = 0.5$, additional sodium chloride was added to the lock fluid before stirring. Lock densities and background ambient buoyancy frequency N were verified by drawing water samples with a syringe every 4cm over the height of the fluid and measuring the densities with an Anton-Paar 5000 DMA density (accuracy of $10^{-6} \text{ g cm}^{-3}$).

Images of the ambient fluid ahead of the lock gate were recorded with a CCD camera (model Jai CV-M4+CL) at 1390 x 1024 pixel resolution, yielding approximately 0.16 to 0.17cm/pixel spatial resolution. The camera was positioned normal to and 567 cm from the front wall. The experiment was illuminated by a vinyl light sheet located 42 cm beyond the back wall of the channel. An opaque mask of randomly distributed transparent dots 0.15cm in diameter and an average

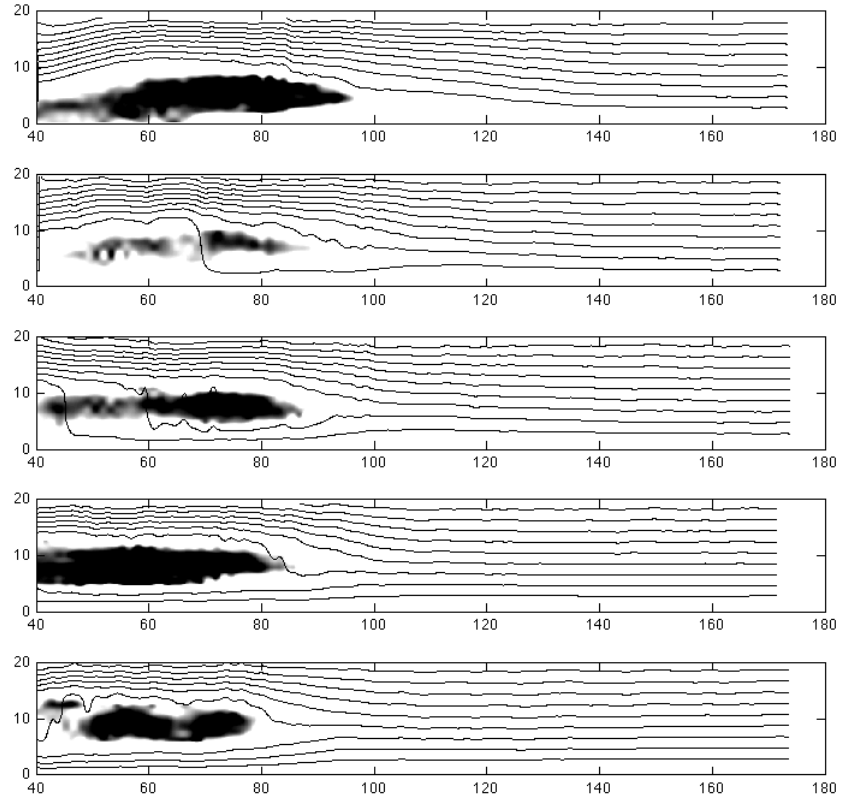


Figure 3.3: Images of laboratory experiment ΔN^2 fields overlaid with density field contours at $tN = 15$ for (top to bottom) $h/H = 0.09, 0.21, 0.31, 0.42, 0.47$. The square of the perturbation buoyancy frequency, $\Delta N^2 > 0.90$, is shown in black, and density contours have been drawn every 0.002 g cm^{-3} . The fastest traveling current is $h/H = 0.09$ and the slowest, $h/H = 0.47$.

distance of 0.45 cm apart was placed directly in front of the light sheet (see Dalziel *et al.* [33] for details). All experiments were conducted beneath a large plastic tarp to isolate it from time varying density gradients in the air between the mask, tank, and camera.

The experiment is started at $t = 0$ by removing the gate vertically, creating vorticity at the gate location and perturbing the free surface of the tank. Turbulence local to the gate position does little to change the IGC dynamics after a short initial transient. The creation and propagation of surface gravity waves, which travel much faster than internal waves, periodically alters the upstream ambient perturbation fields.

Images of the tank and mask were recorded directly onto a PC via Digiflow software (Dalziel [34]) at 24 frames per second. Experimental images were taken only until the theoretical first arrival of mode-1 internal wave motion at the upstream wall, $t = \pi(L - L_{lock})/NH$, preventing the possibility of reflected wave affecting the propagation of the intrusion.

Using the synthetic schlieren processing package within Digiflow, apparent shifts in the image of the mask of random dots were inverted along a light ray path via the experimental geometry to yield the vertical gradient of the perturbation density field $\partial\rho'/\partial z$ (see Dalziel [34] for details). From this field, the perturbations to the square of the buoyancy frequency were then computed as $\Delta N^2 = (g/\rho_0)(\partial\rho'/\partial z)$. Successive images are averaged over 0.5 s, or approximately 1/12 of the internal wave period, minimizing noise in the individual frames. The homogenous density field within the intrusion is identified by ΔN^2 , and the IGC front was determined to be the upstream-most horizontal position where $\Delta N^2(x, z) < -0.90$. The intrusion speed is then estimated by tracking the intrusion through successive frames. The downstream limit of the ambient fluid control volume is also defined by this front position.

Within the ambient fluid, we recover the vertical density perturbation

$\zeta'(x, z, t)$, the vertical velocity $w'(x, z, t)$ and horizontal velocity $u'(x, z, t)$ fields,

$$\zeta' = -\frac{1}{N^2} \int \Delta N^2 dz, \quad (3.11)$$

$$w' = -\frac{1}{N^2} \int \frac{\partial(\Delta N^2)}{\partial t} dz, \quad (3.12)$$

$$u' = \frac{1}{N^2} \int \frac{\partial(\Delta N^2)}{\partial t} dx. \quad (3.13)$$

All integrals were evaluated using Simpson's rule, and time derivatives were taken as the first order central difference across successive video frames. Because the fluid upstream of the intrusion should be unperturbed aside from internal wave motion, we ascribe ζ' , w' , and u' to internal wave motion generated by the intrusion.

To identify the internal wave modes propagating ahead of the current, the horizontal velocity field u' for each frame was decomposed into its cosine coefficients $\hat{u}(x)$ at each horizontal position,

$$\hat{u}_m = \frac{2}{H} \int_0^H u'(z) \cos\left(\frac{m\pi}{H}z\right) dz. \quad (3.14)$$

where m is the mode number. Because the vertical velocity must be null at the upper and lower boundaries, the vertical velocity modes are sine waves in z . By continuity, the horizontal velocity profile in z must be a cosine, and we therefore chose cosine basis functions by which to decompose the horizontal flow. Vectors of the cosine coefficients of the first two modes, $\hat{u}_1(x)$ and $\hat{u}_2(x)$, are stacked to form $x - t$ diagrams, which are used to determine group speed. We then filtered all other modes by reconstituting the velocity field,

$$u_m(z) = \int_0^H \hat{u}_m \cos\left(\frac{m\pi}{H}z\right) dz. \quad (3.15)$$

before evaluating the energy fields.

The potential, kinetic, and total energy of the wave field upstream of the current were then calculated within the control volume by employing (3.9), and (3.10), and (3.8), respectively.

3.3.2 Numerical Simulations

Direct numerical simulations of lock releases were conducted in two-dimensions for a background ambient buoyancy frequency $N = 1.0 \text{ s}^{-1}$ for five equally spaced

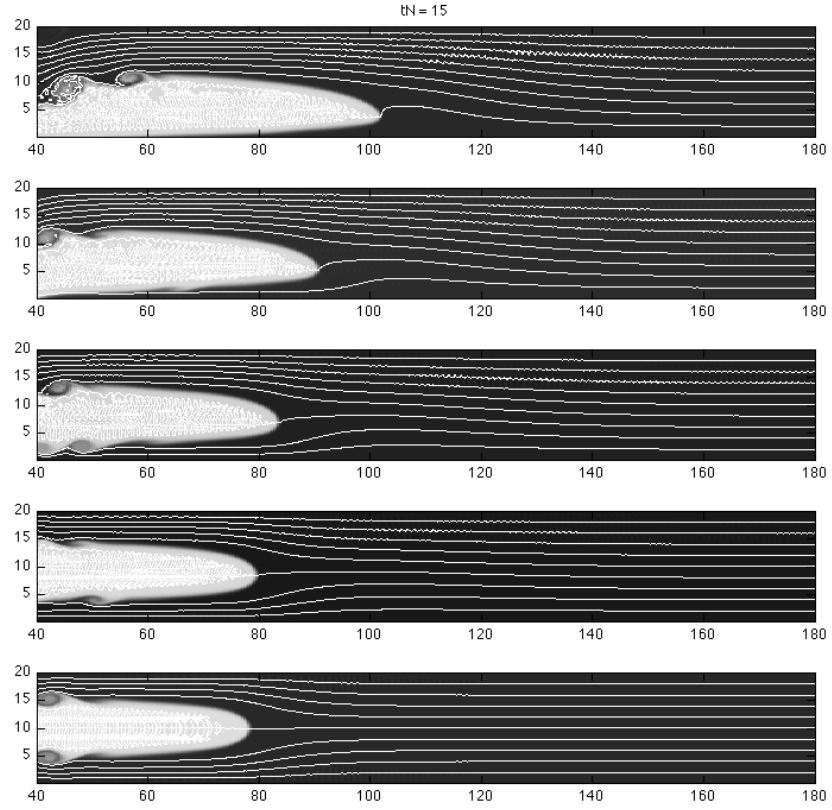


Figure 3.4: Numerical simulation tracer fields overlaid with density field contours at $tN = 15$ for (top to bottom) $h/H = 0.1, 0.2, 0.3, 0.4, 0.5$. Tracer concentration, $C > 95\%$ is shown in white, and density contours are drawn every 0.002 g cm^{-3} . As in the experiments, the fastest current is $h/H = 0.1$, and the slowest is $h/H = 0.5$

values of the neutral buoyancy level h/H between 0.1 and 0.5. The minimum Reynolds numbers for the simulations were $Re_{ambient} = 4 \times 10^4$ and $Re_{intrusion} = 2.8 \times 10^3$.

The simulations were conducted in a two-dimensional domain, of 366 cm length and 20 cm height, discretized into a uniform grid of 1024 x 256 points. The vertical grid spacing of $\Delta x = 0.078$ cm was chosen to be much smaller than the maximum upstream isopycnal displacement observed by Monroe *et al.* [28] of $H/5 = 4$ cm. The full numerical domain was composed of two symmetric 183 x 20 cm lock releases reflected about a vertical line of symmetry with the lock fluid propagating from the center outward (Sutherland *et al.* [30]). The lock fluid occupied $L_{lock} = 40$ cm in each of the two experimental domains and was marked with a passive tracer.

A slightly modified version of the open source DNS algorithm Diablo (full details available at <http://renaissance.ucsd.edu/fccr/software/Diablo.html>) was used to solve the 2-dimensional, incompressible Boussinesq equations subject to no-slip boundary conditions, where the kinematic viscosity $\nu = 0.01 \text{ cm}^2\text{s}^{-1}$ and the Schmidt number $Sc = 1$ (see Härtel *et al.* [35] for justification of the increased molecular diffusivity). The horizontal symmetry allowed periodic boundary conditions and therefore the spectral evaluation of flow variables in the horizontal direction. To minimize Gibbs phenomenon, density steps in the horizontal direction were initially smoothed with a hyperbolic tangent profile. Vertical derivatives were evaluated using second-order centered finite-differences. The flow was advanced with a combination of a third-order, low-storage Runge-Kutta-Wray scheme and a Crank-Nicholson scheme at $\Delta t = 0.001$ s. Only vertical diffusive terms were treated implicitly.

The flow was set into motion at $t = 0$, and the numerics were allowed to progress until the mode-1 waves reached the sides of the domain at $t = \pi(L - L_{lock})(NH)^{-1}$. Surface waves were not an issue due to the lack of a gate or a free surface in the simulated domain.

Field information for density ρ , velocity \mathbf{u} , and tracer concentration C was recorded at 0.5 s intervals over the entire domain for the duration of the numerical

experiment. The position of the IGC front was determined to be the upstream-most point where the concentration, C was 95% of the lock concentration. This position was taken to be the downstream limit to the upstream ambient fluid control volume. Tracking the front position through successive frames provided an estimate of IGC speed.

The horizontal velocity signal, u , was decomposed with cosine basis functions using (3.14). Vectors of the cosine coefficients for each mode were constructed and stacked chronologically to form $x - t$ diagrams. Group speed was determined from the diagram. We then recomposed the velocity field using (3.15), to determine the energy fields.

3.4 Results

After an initial period of acceleration, all well-mixed intrusions generated in the laboratory experiments and numerical simulations were observed to reach a constant speed phase as they propagated along the level of neutral buoyancy for multiple lock lengths. Figures 3.3 and 3.4 illustrate the intrusions at $tN = 15$ over the range of h/H . There is good agreement in shape, propagation level, and speed of the intrusions between the experiments and the simulations.

Comparing the observed intrusion speeds to the Bolster *et al.* [4] prediction for well-mixed intrusions into a linearly stratified ambient fluid in figure 3.5, we find good agreement. Intrusions closest to the half depth of the fluid, $h/H = 0.5$, are the slowest and subcritical to both mode-2 and mode-1 theoretical group speeds. Intrusions nearest the boundaries, $h/H = 0.1$ travel at nearly twice the equilibrium speed, remaining subcritical to mode-1 but supercritical to mode-2.

The maximum isopycnal displacement upstream of the currents is observed to be $\zeta'/H \approx \frac{1}{3}$, (see figure 3.6). Wavelengths were not measured, as no periodic signal in ζ' could be observed within L . We therefore also note $\lambda \gg \zeta'$.

Figures 3.7, 3.8, and 3.9 present a series of snapshots at 5 s intervals of the experiments and simulations of intrusions along $h \approx 0.1$, 0.3, and 0.5, respectively. The density field in the upstream ambient fluid control volume is contoured at

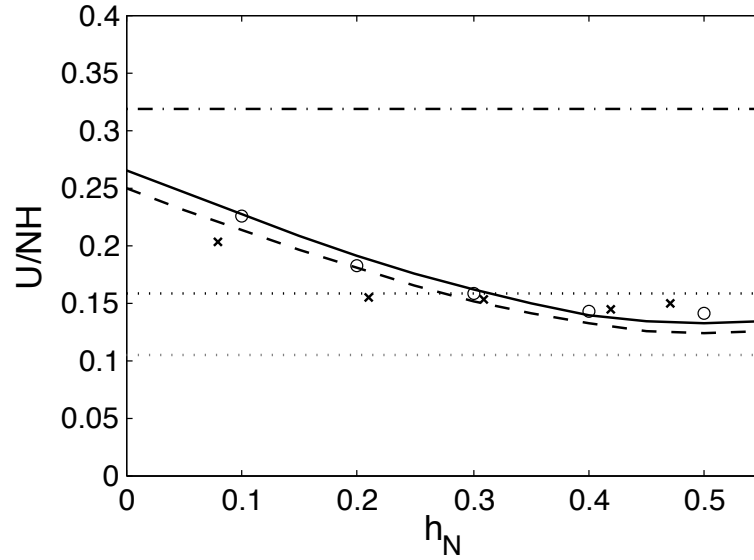


Figure 3.5: A plot of the non-dimensional speeds of the IGCs in experiments (x) and simulations (o). The Bolster *et al.* [4] theoretical speed (3.4) is plotted for $Fr = 0.266$ (solid line) and $= 0.25$ (dashed line), and theoretical mode-1 (dot-dashed line), mode-2 (dotted line), and mode-3 (gray dotted line) group speeds are also displayed. Note that $h/H \approx 0.3$ represents the intersection between theoretical IGC and mode-2 group speeds, and all intrusions are supercritical to mode-3 group speeds.

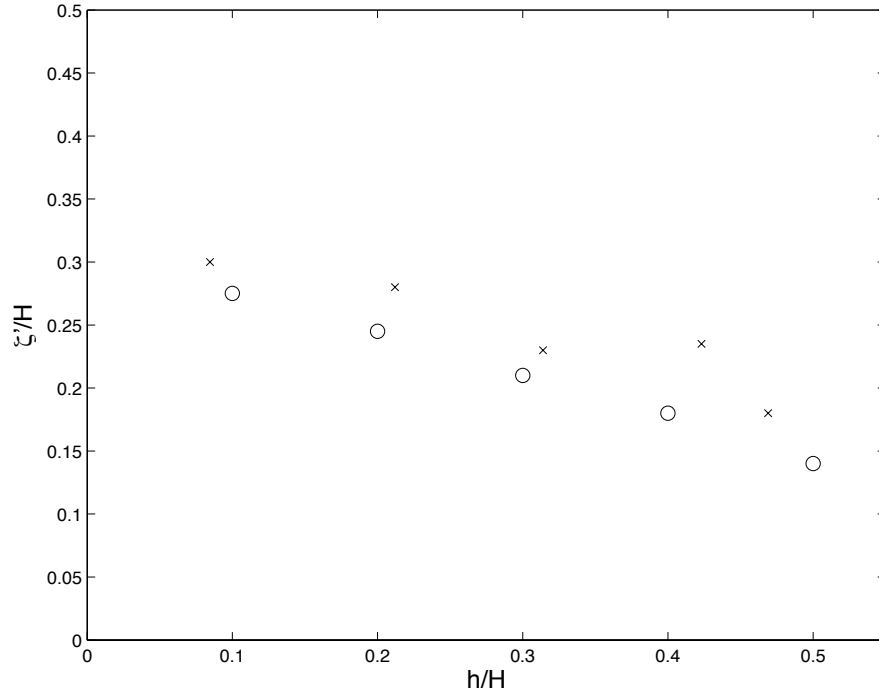


Figure 3.6: A plot of the maximum isopycnal displacement versus level of neutral buoyancy, showing both experimental (x) and numerical (o) results. The maximum displacement observed was $\zeta'/H < \frac{1}{3}$, whereas wavelength was too large to be detected, $\lambda \gg L$.

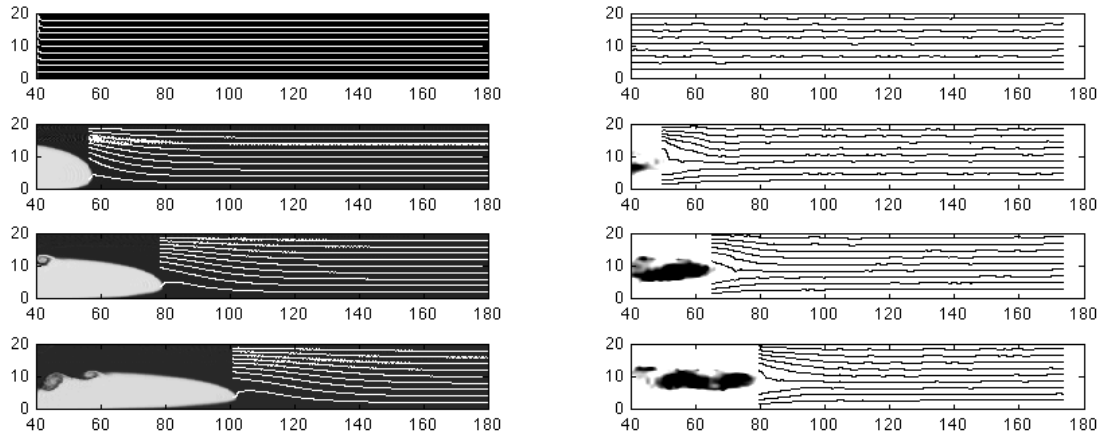


Figure 3.7: Intrusions propagating at $h/H = 0.1$ and contours of the upstream ambient density fields for simulations (left) and experiments (right) at $t = 0, 5, 10, 15$ s. Wave motion in the control volume takes the shape of long mode-1 waves.

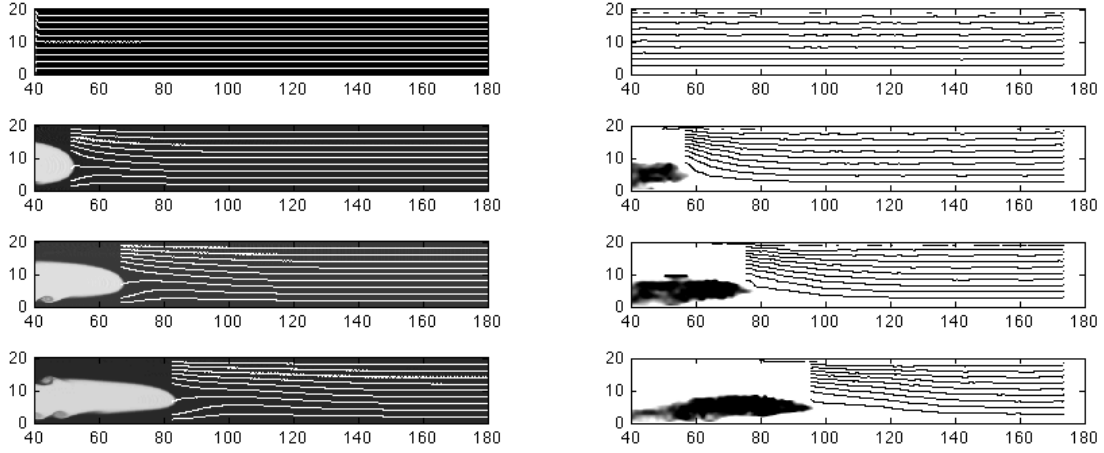


Figure 3.8: Intrusions propagating at $h/H = 0.3$ and contours of the upstream ambient density fields for simulations (left) and experiments (right) at $t = 0, 5, 10, 15$ s. Wave motion in the control volume takes the shape of long modes 1 and 2 waves.

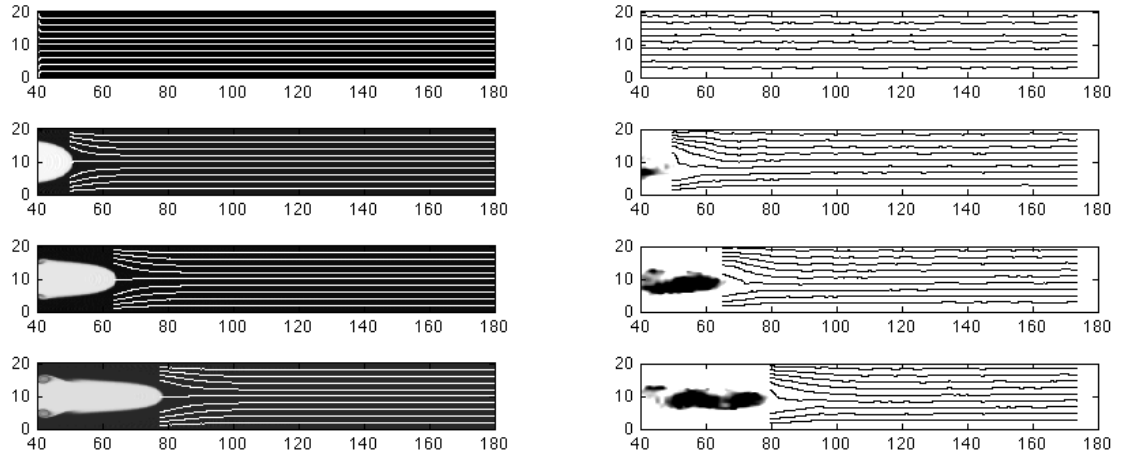


Figure 3.9: Intrusions propagating at $h/H = 0.5$ and contours of the upstream ambient density fields for simulations (left) and experiments (right) at $t = 0, 5, 10, 15$ s. Wave motion in the control volume takes the shape of long mode-2 waves.

regular intervals, and shows clear evidence of perturbations preceding the IGCs. The density perturbations preceding $h = 0.1$ IGCs are only positive in z , and have traveled further by $tN = 15$ than the density perturbations preceding $h = 0.5$ IGCs, which are positive in z above the midplane of the experiment and negative in z below. The density contours in the upstream control volume for the intrusions along $h = 0.3$ (critical to mode-2) show both upward and downward deflection of the isopycnals near the IGC front, but only upward deflections of the current further upstream.

The coefficients of the velocity field vertical cosine decomposition are the maximum fluid velocities associated with each mode. Distance versus time ($x - t$) plots of the non-dimensionalized fluid velocities for the experiments and the numerics are presented in figures 3.11 and 3.10, respectively, and compared to the observed IGC speed and the relevant internal wave mode group speeds. The propagation of the velocity disturbance upstream of the current travels at the theoretical long-wave speeds, marked by the dashed lines. For intrusions near the boundary, ($h = 0.1$), the mode-1 velocity amplitude signal propagates at the predicted mode-1 long-wave group speed, while no mode-2 velocity amplitude signal is seen upstream of the IGC position. For the slower $h = 0.5$ intrusion there is no significant mode-1 signal, and a strong mode-2 signal, which travels at the theoretical long-wave mode-2 group speed. At the point where mode-2 waves are critical to IGC speeds, ($h = 0.3$), there is a mode-1 velocity amplitude less than that of the near-boundary current, but greater than that of midplane current; and there is also a faint mode-2 signal of an amplitude less than that of the midplane intrusions. The observed speeds of the individual modes match predictions by long-wave theory.

The horizontal banding in the experimental images (figures 3.11 and 3.13) is due to surface wave motion, which obeys the dispersion relation, $\omega = \sqrt{gH}$. For our experimental parameters, the lowest seiche mode generated by the gate removal occurs at a period $T = 2.6$ s, with a speed $c_{surface} = 139$ cm/s. These waves generate fluid motion within the stratified fluid, which appears in the $x - t$ plots the horizontal bands spaced at 2.6 s intervals.

The horizontally averaged vertical flux of horizontal momentum, $\langle u'w' \rangle$,

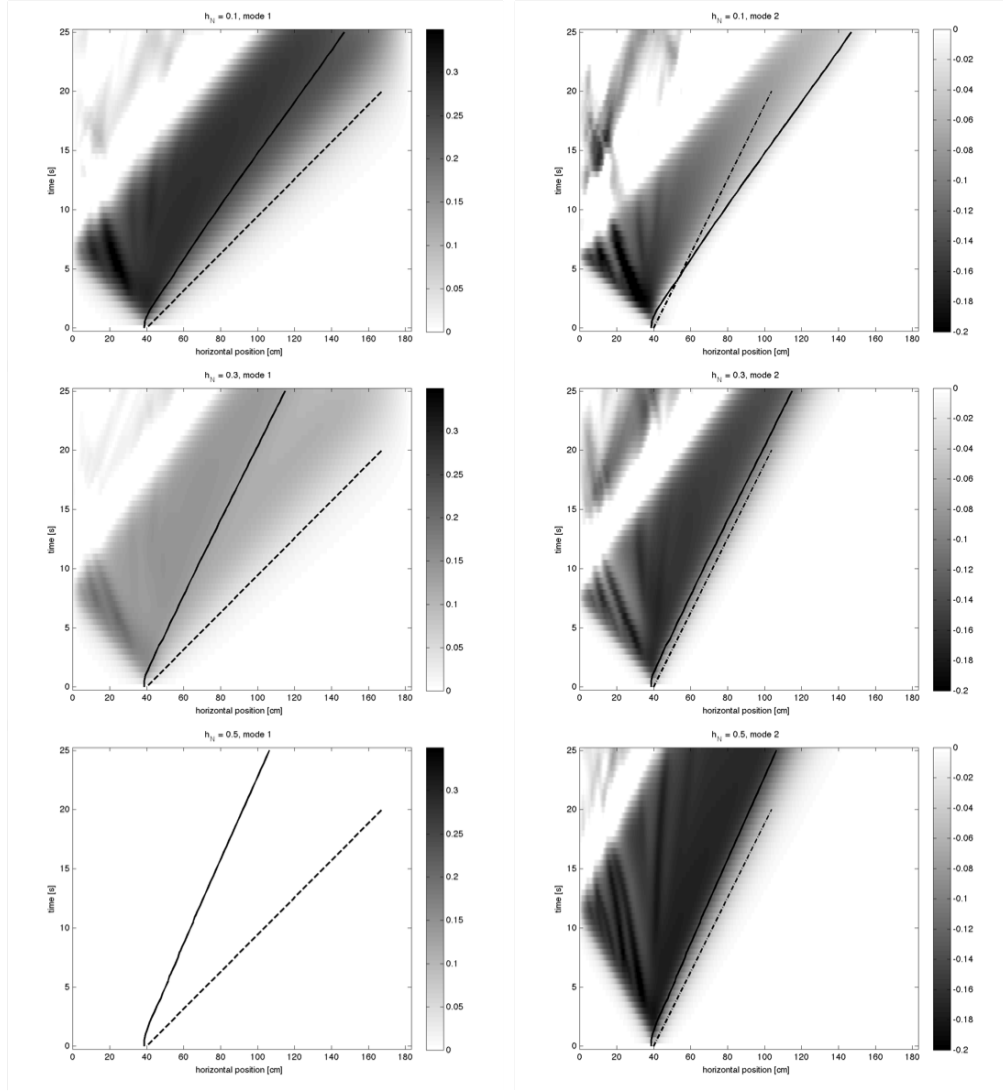


Figure 3.10: $x - t$ diagrams of the non-dimensional cosine decomposition coefficients, \hat{u}/NH , of the numerical simulations for mode-1 (left) and mode-2 (right) and $h/H = 0.1$ (top), $h/H = 0.3$ (middle), $h/H = 0.5$ (bottom). The observed IGC position is plotted by the solid line, while the theoretical wave speed for the relevant mode is overlaid with the dashed line (mode-1) or the dot dashed line (mode-2). Theoretical and observed mode speeds agree well.

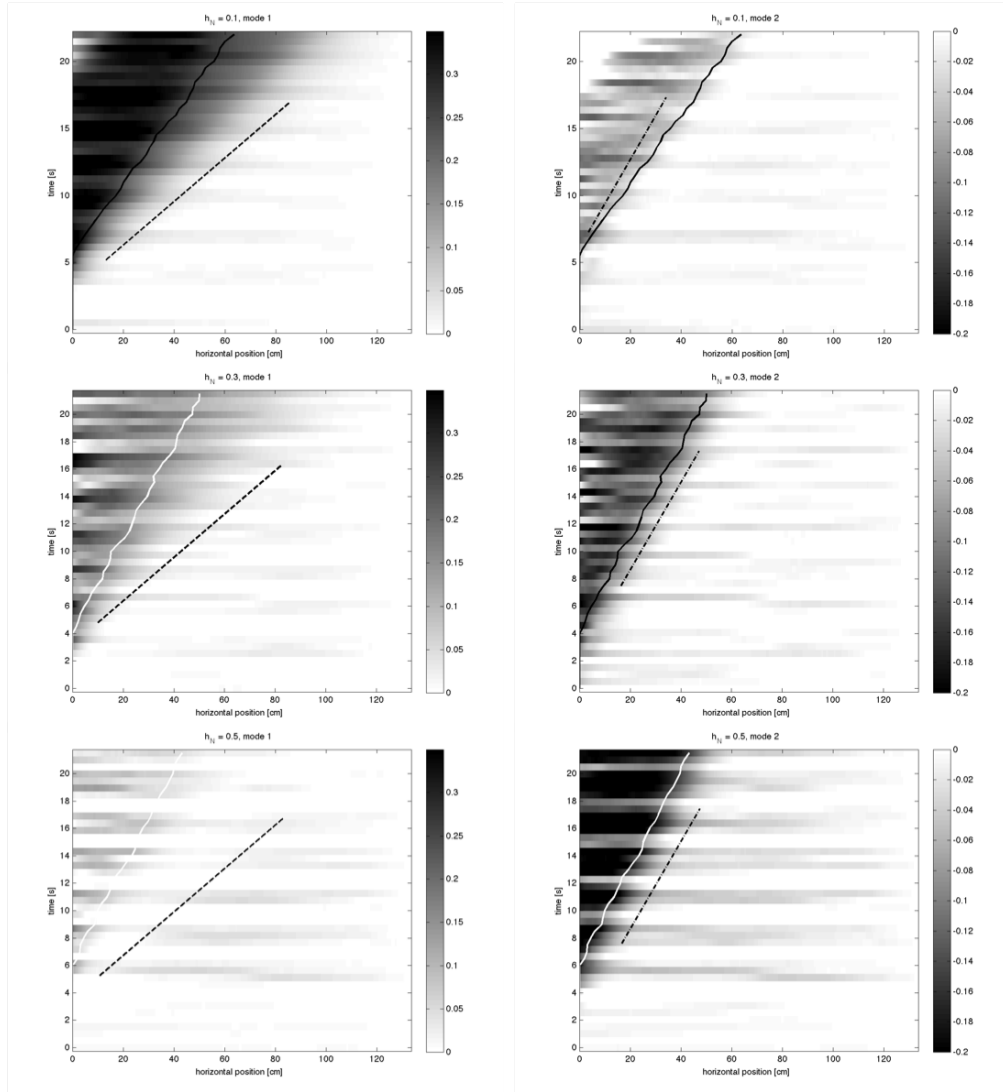


Figure 3.11: $x - t$ diagrams of the non-dimensional cosine decomposition coefficients, \hat{u}/NH , of the laboratory experiments for mode-1 (left) and mode-2 (right) and $h/H = 0.09$ (top), $h/H = 0.31$ (middle), and $h/H = 0.47$ (bottom). The observed IGC position is plotted by the solid line, while the theoretical wave speed for the relevant mode is overlaid with the dashed line (mode-1) or the dot dashed line (mode-2). Theoretical and observed mode speeds agree well. The periodic banding in the images is due to surface wave motion.

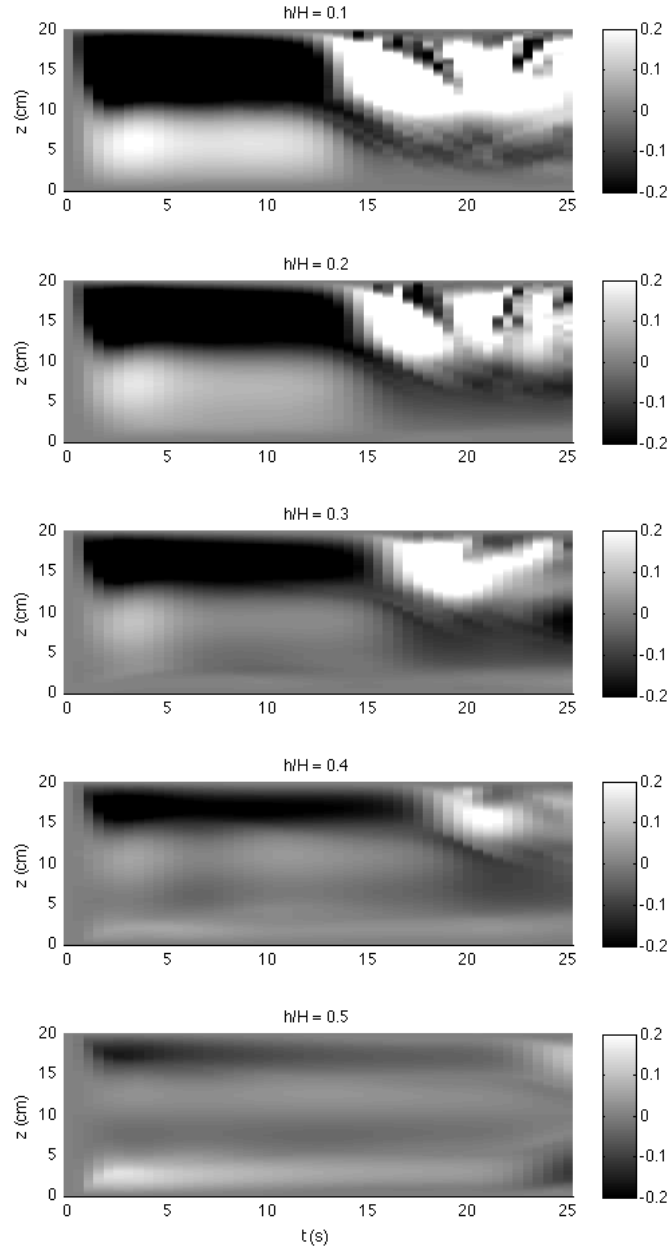


Figure 3.12: Plots of the horizontally averaged vertical flux of horizontal momentum, $\langle u'w' \rangle$, observed within the upstream control volume in numerical simulations as a function of time and vertical position. The magnitude of the fluxes decreases and the structure of the flux shifts from mode-1 to mode-2 as the level of neutral buoyancy approaches the midplane.

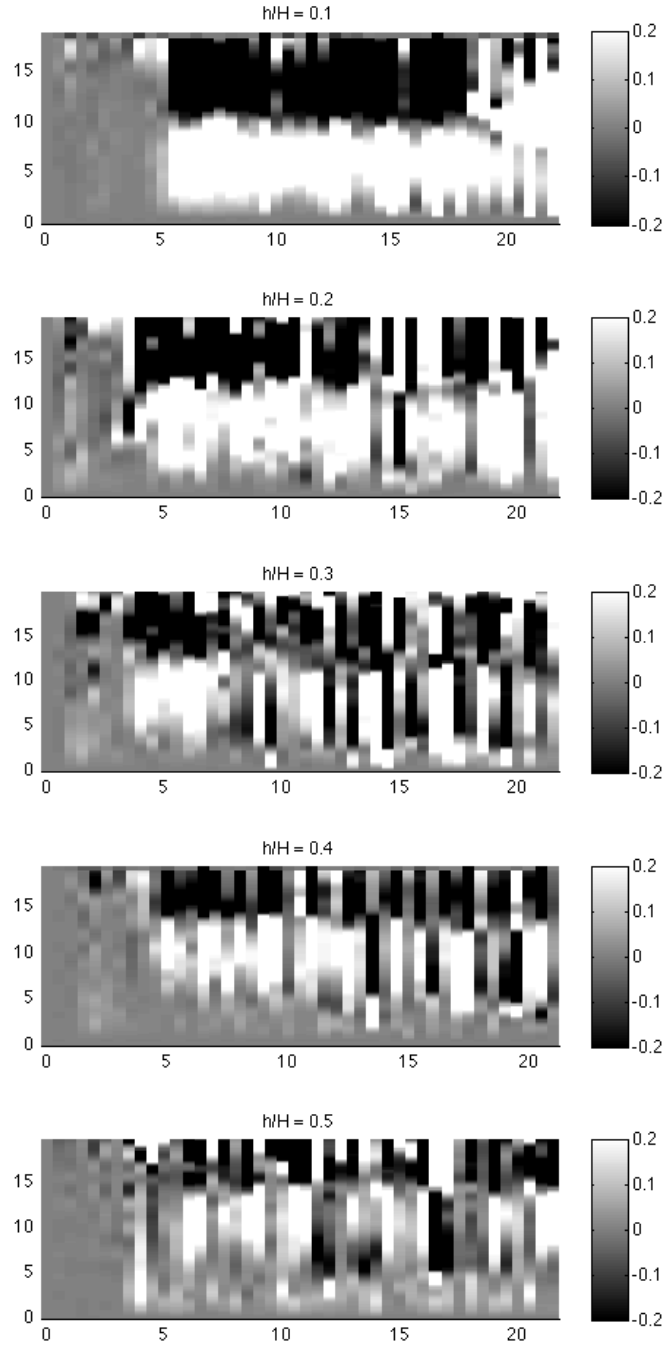


Figure 3.13: Plots of the horizontally averaged vertical flux of horizontal momentum, $\langle u'w' \rangle$, observed within the upstream control volume in laboratory experiments as a function of time and vertical position. The magnitude of the fluxes decreases and the structure of the flux shifts from mode-1 to mode-2 as the level of neutral buoyancy approaches the midplane. Vertical banding in the images is due to surface waves.

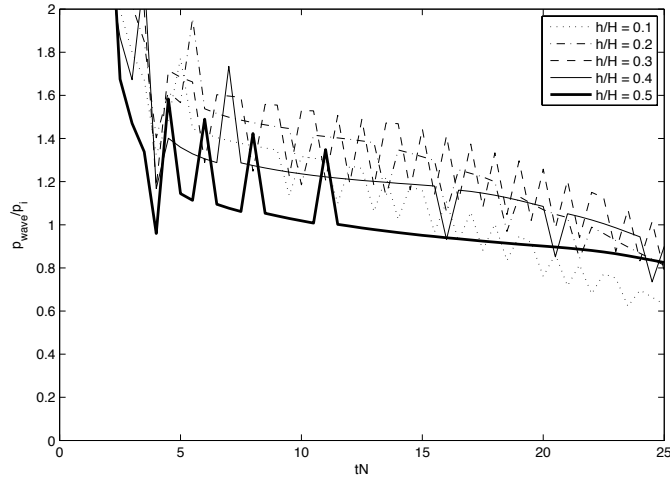


Figure 3.14: The ratio of horizontal momentum contained in the upstream waves to the horizontal momentum of the IGC p_{wave}/p_i as a function of time, showing approximately the same amount of momentum in the upstream wave field as in the current.

within the upstream control volume is described in figures 3.12 and 3.13 for simulations and experiments, respectively. For IGCs propagating near the boundaries, (e.g. $h/H = 0.1$) there is a much greater flux of momentum, which takes the shape of a mode one disturbance. Intrusions nearer the midplane $h/H > 0.4$ show a distinct mode-2 structure to the momentum flux, and have significantly lower magnitude than the asymmetrical intrusions. Experimental images suffer from noise created by the seiche motion introduced by removing the gate. However, the magnitude and structure of the momentum flux is in agreement with the numerical simulations. At later times, the sudden change in the structure of the internal wave field is associated with the arrival of the first mode at the far endwall (e.g. at $t \approx 13$ s for $h/H = 0.1$ in figures 3.12 and 3.10), and likely describes the reflection of the disturbance from the endwall.

Measurements of the upstream internal wave field from the simulations show a linear increase in total horizontal momentum with time. The total horizontal wave momentum measured from the numerical data is observed to be of the same magnitude as estimates of the total horizontal momentum of the current by (3.5),

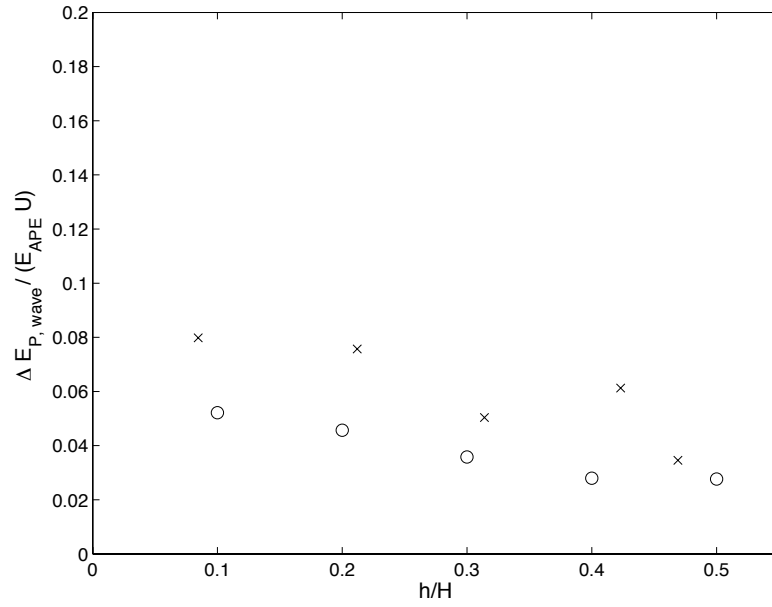


Figure 3.15: The normalized rate of increase in upstream potential wave energy against the level of neutral buoyancy for experiments (x's) and simulations (o's).

varying less than 50%, (see figure 3.14).

The rate of increase of potential, kinetic, and total wave energy in the control volumes is observed to be linear until the internal wave motion reaches the upstream endwall. We normalize this rate by an estimate of the slumping rate described by (3.6), and present $\Delta E_{P,wave}/(E_{APE}2U)$, $\Delta E_{K,wave}/(E_{APE}2U)$, and $\Delta E_{wave}/(E_{APE}2U)$, for the range of h/H in figures 3.15, 3.16, and 3.17. The total energy is observed to be equipartitioned between the kinetic and potential energy fields for all levels of neutral buoyancy. For well-mixed intrusions into a linearly stratified ambient fluid, approximately five to fifteen percent of the APE is converted into wave energy. Intrusions nearer the boundaries transfer a greater proportion of energy to the wave field.

3.5 Discussion

This chapter examines the internal wave field generated by well-mixed intrusive gravity currents propagating into a linearly stratified ambient fluid, inves-

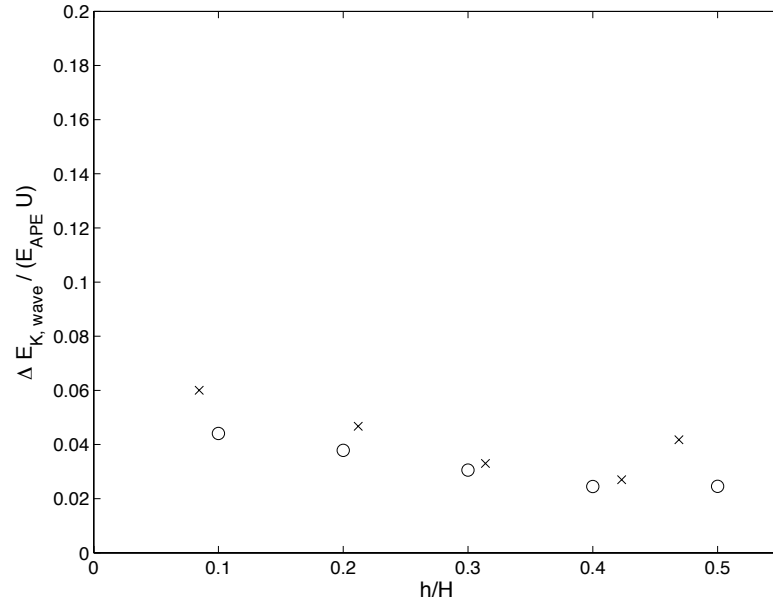


Figure 3.16: The normalized rate of increase in upstream kinetic wave energy against the level of neutral buoyancy for experiments (x's) and simulations (o's).

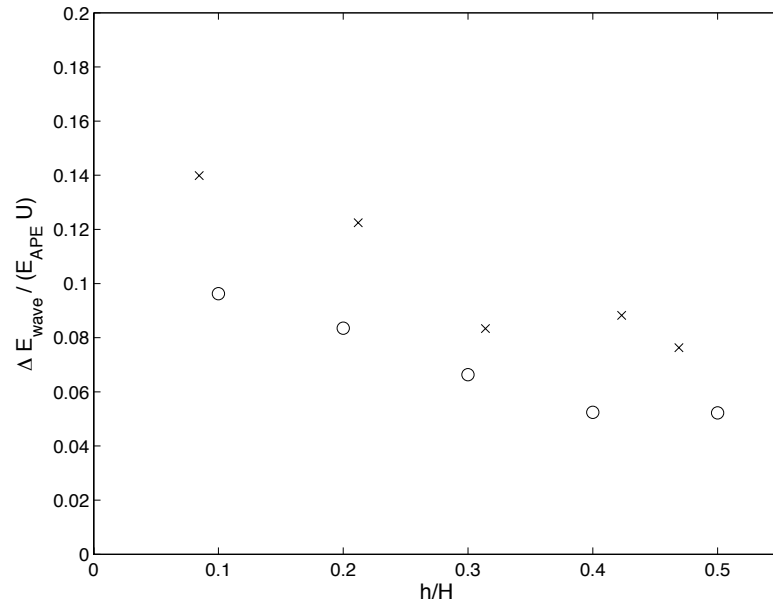


Figure 3.17: The normalized rate of increase in upstream total wave energy against the level of neutral buoyancy for experiments (x's) and simulations (o's).

tingating perturbations within a control volume upstream of the IGC front, and neglecting wave motion that is subcritical to the front speed of the IGC. Through synthetic schlieren laboratory experiments and two-dimensional numerical simulations, we have examined the internal wave response over a the range of neutral buoyancy levels $0.1 < h/H < 0.5$. The flow is Boussinesq, and so we expect the behavior for intrusions above the midplane to behave similarly as they depart from the equilibrium condition $h/H = 0.5$.

We successfully generated well-mixed intrusive gravity currents with speeds varying with h as predicted by (3.4) [4], and show that a linear internal wave response is excited by the intrusions. Comparing (3.4) and the group speed of internal long-wave modes described by (3.7), shows that all intrusions are all subcritical to mode-1 internal long-wave speeds, and intrusions propagating at height within $0.3 < h/H < 0.8$ are also subcritical to mode-2 internal long-waves. All intrusions are supercritical to mode-3 internal waves.

Upstream perturbations of the density and velocity fields, accessed through synthetic schlieren laboratory methods or numerical simulations, show a dependence of modal structure on the height of forcing h . Forcing at a level of neutral buoyancy near the horizontal velocity maximum of a particular wave mode preferentially excites that wave mode, transferring energy more efficiently upstream. For intrusions where h/H approaches the boundaries 0 and H , mode-1 is excited more strongly, and for IGCs where h/H approaches the midplane of the experiment, $H/2$, mode-2 is excited more strongly. Because mode-1 is supercritical to all intrusions, the absence of a mode-1 signal in the $h/H = 0.5$ intrusions (figures 3.10 and 3.11) can only be explained by inefficient forcing of mode-1. However IGCs are only subcritical to both modes 1 and 2 near the midplane of the fluid, $0.3 < h/H < 0.8$, and outside of this range only mode-1 perturbations travel fast enough to alter the environment upstream of the intrusion.

These linear internal wave modes propagate upstream at a velocity closely matching that predicted by (3.7). This agreement indicates that the angle of wave energy propagation θ is approximately null with respect to the horizontal. By the dispersion relation for linear internal waves $\sin \theta = \omega/N$, constant velocity IGCs

unaffected by the finite length of the lock can therefore be thought of as forcing the upstream wave field with a frequency of $\omega = 0$.

Investigation of the internal wave field generated upstream of intrusions in which the finite nature of the lock is relevant show a markedly different speed and structure of the generated wave field. Monroe *et al.* [28] showed that waves reflected from the lock endwall propagate upstream and dominate the wave field. These waves were observed to have similar amplitude but shorter wavelengths than the waves observed in this study, and to travel at speeds less than the theoretical long internal wave mode speeds. The authors found that approximately 10% to 20% of the Available Potential Energy was transferred into the wave field.

Our observations of the wave field unaffected by waves reflected from the back endwall of the lock show a transfer rate of approximately five to fifteen percent from APE into wave energy. This is of the same order as losses to dissipation in unstratified boundary currents Sutherland *et al.* ([36]) or the Boussinesq approximation. This finding is consistent with the success of energy scaling arguments in models of intrusive gravity currents propagating at constant speeds, such as those employed in Cheong *et al.* [6], Bolster *et al.* [4], or Maurer *et al.* [3].

Both the Available Potential Energy and the percentage of APE transferred to the upstream wave field increases with the asymmetry of the intrusions. Mode-1 waves propagate more quickly and possess a higher energy density, with higher isopycnal displacements and higher fluid motion velocities, than mode-2 waves. IGCs that more efficiently excite mode-1 show a greater percentage of APE transferred to the upstream wave field.

Though energy scaling models such as Bolster *et al.* [4] and Maurer *et al.* [3] successfully predict the speed of intrusive gravity currents in linearly stratified fluids, the dynamics of the flow remain unclear. We have shown that there is structured upstream transfer of both momentum and energy from these currents to supercritical internal wave motion, and that both the intrusion speed forcing and the upstream wave field response vary linearly with the ambient stratification NH . However, how these upstream perturbations interact with the advancing IGC front is beyond the scope of the work presented here. Instead this work

suggests the plausibility of an analytical model in the style of Flynn *et al.* [22]. Such a model could incorporate the upstream perturbations in a balance of mass, momentum, and energy to determine the speed of a well-mixed intrusive gravity current propagating into a linearly stratified ambient fluid and provide valuable insight into the dynamics actually controlling the speed of these currents.

Chapter 4

Adjacent continuous stratifications

4.1 Abstract

We present an experimental and numerical study of one stratified fluid propagating into another. The two fluids are initially at rest in a horizontal channel and are separated by a vertical gate which is removed to start the flow. We consider the case in which the two fluids have the same mean densities but have different, constant, non-zero buoyancy frequencies. In this case the fluid with the smaller buoyancy frequency flows into the other fluid along the mid-depth of the channel in the form of an intrusion, and two counter-flowing gravity currents of the fluid with the larger buoyancy frequency flow along the top and bottom boundaries of the channel. Working from the available potential energy of the system and measurements of the intrusion thickness, we develop an energy model to describe the speed of the intrusion in terms of the ratio of the two buoyancy frequencies. We examine the role of the stratification within the intrusion and the two gravity currents, and show that this stratification plays an important role in the internal structure of the flow, but has only a secondary effect on the speeds of the exchange flows.

4.2 Introduction

Intrusions or intrusive gravity currents occur when horizontal density gradients result in the intrusion of one fluid into another fluid at an intermediate depth. Intrusions are closely related to gravity currents which occur when one fluid flows

into another of different density along a horizontal boundary (Simpson[11]). The presence of vertical density stratification of the receiving fluid is a necessary condition for the existence of an intrusion, and the literature (e.g. Amen & Maxworthy [13], Faust & Plate [37], Ungarish [38], Bolster *et al.* [4], Nokes *et al.* [39]) has traditionally investigated gravity currents and intrusions containing of fluid uniform density into a stratified ambient fluid. However, in many natural and industrial flows the intruding fluid is also stratified and the role of this stratification and its influence on the exchange flow are the subject of this chapter.

For the case of an unstratified intrusion, the potential energy stored in the intrusion relative to the surrounding ambient fluid is converted into the kinetic energy of horizontal motion. This motion has been shown to be important to the transport of mass, energy, and particulate matter in environmental flows, from dust storms and seafloor turbidity currents to locust and plankton distributions (Simpson [11]). The intruding fluid carries material with it, and an unstratified intrusion has relatively little internal circulation, and any internal flow is traditionally ignored in the analysis of the flow (Lowe *et al.* [19]. For example, Benjamin's (1968) [5] classical analysis of a gravity current assumes that the current moves as a plug with an equal forward velocity at all points in the current.

When the intruding fluid itself is stratified there is the added possibility of vorticity being generated within the intrusion itself by the interaction of the pressure gradients and the density gradients – the so called ‘baroclinic generation of vorticity’. This internal circulation can be significant depending on the magnitude of the stratification within the intrusion. This work aims to extend our understanding of high Reynolds number, Boussinesq intrusive gravity currents to the case where stratification exists in *both* the ambient and the intruding fluids.

Intrusive gravity currents are often studied in the context of lock-release experiments, in which a finite volume of fluid is released into a larger body of stratified fluid by the rapid removal of a vertical barrier (e.g. Keulegan [40], Amen & Maxworthy [13]). We consider the case where the fluids on both sides of the barrier have the same depth H , their densities are linear functions of height, $\rho(z) = \rho(z_n) + (\rho_0/g)N^2z$, and their average densities $\rho_i(z_n) = \rho_a(z_n)$ are the same. Here

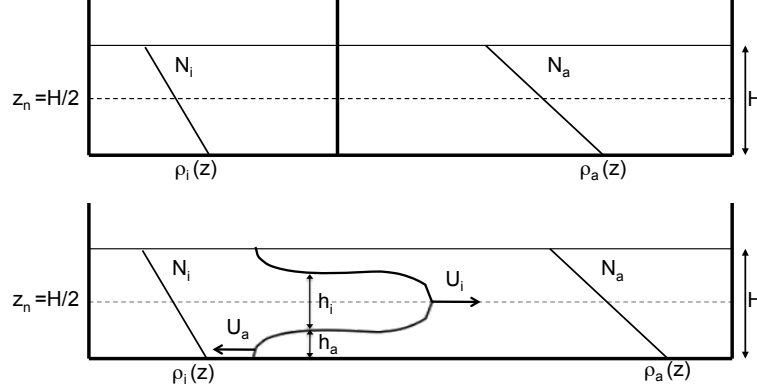


Figure 4.1: Schematic showing the initial conditions of lock-release of a linearly stratified intruding fluid of constant buoyancy frequency N_i , into a linearly stratified ambient fluid of buoyancy frequency N_a , where the average densities of both fluids are equal. When the barrier is removed, the intrusion propagates along the level of neutral buoyancy $z_n = H/2$ at a speed that is a function of the stratification ratio $S = N_i^2/N_a^2$.

z_n is the level of neutral buoyancy chosen to be the mid-depth of the channel for both fluids, ρ_0 is a reference density, g is gravity, and $N = \sqrt{-\frac{g}{\rho_0} \frac{\partial \rho}{\partial z}}$ is the buoyancy frequency of the stratification, where the subscripts i and a refer to the intruding and ambient fluids, respectively, and by definition $N_i < N_a$ (figure 4.1). When the barrier is removed at $t = 0$, the intrusion flows into the ambient fluid along the level of neutral buoyancy at the mid-depth of the ambient fluid, while two gravity currents of ambient fluid travel in the opposite direction, one along the upper and the other along the lower boundaries of the tank. The choice of linear stratification and equal mean densities means that the flow is vertically symmetric about the mid-depth of the tank. If this condition is relaxed then the fluid with the lower centre of gravity would tend to flow beneath the other producing a bulk circulation within the flow field.

In the present case after a brief period of acceleration, the intrusion travels into the ambient fluid at a constant speed for multiple lock lengths before decelerating, similar to observations by Maxworthy *et al.* [23] of well-mixed boundary currents in a stratified ambient fluid. We limit our study to this initial constant-velocity phase of propagation, during which the lock fluid is unaffected by the

presence of the endwall of the lock. At later times we expect the finite volume of the lock to become important and, at these times an unstratified intrusion decelerates. This is the so-called ‘similarity phase’ (Rottman & Simpson [18]). While we expect similar behavior to occur for a stratified intrusion, it has not been considered in this work.

For an unstratified ($N_i = 0$) mid-depth intrusion into a linearly stratified ambient fluid, dimensional analysis implies that, at high Reynolds numbers, the intrusion speed U_i during the initial constant velocity phase takes the form

$$U_i = FN_a H, \quad (4.1)$$

where F is a dimensionless Froude number. Treating the midplane intrusion as two symmetric well-mixed boundary gravity currents reflected about the midplane of the tank, Bolster *et al.* [4] extended findings by Maxworthy *et al.* [23] and Ungarish [38] to show that $F \approx 0.125$. Bolster *et al.* [4] also show that, during this initial constant-velocity phase of propagation, (4.1) is consistent with the constant rate of conversion of available potential energy to kinetic energy, and that such energy conversion also predicts the speed of intrusions that are not located at the mid-depth of the tank. Here, we extend the energy conversion model for mid-depth intrusions to incorporate the role of stratification in the intruding fluid, $N_i > 0$, and examine the effect of the consequent reduction in the available potential energy on the speed of the intrusion during the constant-velocity phase.

In section 4.3 we present the mathematical model, which in this case needs to take account of the varying intrusion thickness with N_i , and a prediction of the intrusion speed. We describe laboratory experiments and two-dimensional numerical simulations in section 4.4 and compare the results with the theory in section 4.5. In section 4.6 and section 4.7, we compare our results to the unstratified case and discuss the role of the stratification within the intrusion.

4.3 Model

Following the approach of Cheong *et al.* [6] and Bolster *et al.* [4], we consider an energy model relating the conversion of available potential energy of

the initial hydrostatic pressure imbalance before the lock is opened to the constant increase of kinetic energy in the current after the gate is removed.

The lock release can be described in terms of two dimensionless parameters: the Froude number F defined by (4.1) and the stratification ratio S of the intruding and ambient fluid stratifications

$$S \equiv N_i^2/N_a^2, \quad (4.2)$$

where, by definition, $0 \leq S \leq 1$. When $S = 0$, the intruding fluid is well-mixed and corresponds to the case described by Bolster *et al.* [4], where the intrusion travels at

$$U_i(S = 0) \approx 0.125N_aH. \quad (4.3)$$

When $S = 1$, $N_i^2 = N_a^2$, the densities of the two fluids on either side of the lock are identical and, obviously,

$$U_i(S = 1) = 0. \quad (4.4)$$

Dimensional analysis implies that

$$U_i = 0.125N_aHf(S), \quad (4.5)$$

where, the factor of 0.125 is to account for the value of the Froude number for unstratified intrusions $S = 0$, and the dimensionless function $f(S)$ of the stratification ratio S must satisfy the criteria imposed by (4.3) and (4.4) that $f(0) = 1$ and $f(1) = 0$.

In order to determine the form of $f(S)$, we examine the available potential energy (APE) as a function of the stratification ratio. Taking the level of neutral buoyancy as the reference level, the APE per unit volume is

$$E = g \int_{-H/2}^{H/2} (\rho_i - \rho_a) z dz, \quad (4.6a)$$

$$= \frac{gH^2}{6} (\rho_a - \rho_i) \Big|_{-\frac{H}{2}}, \quad (4.6b)$$

$$= \frac{\rho_0 H^3 N_a^2}{12} (1 - S). \quad (4.6c)$$

We normalize E by the available potential energy $\frac{1}{12}\rho_0 H^3 N_a^2$ of a well mixed intrusion, (Bolster *et al.* [4]). This leads to a non-dimensional form E^* of the APE

per unit volume in terms of the stratification ratio S

$$E^* = (1 - S). \quad (4.7)$$

As the simplest extension of the analysis of an unstratified intrusion (Bolster *et al.* [4]), we first neglect the motion in the counterflowing gravity currents and assume that the intrusion thickness is independent of S . Assuming that the rate of conversion of APE to the intrusion kinetic energy (proportional to U^2) is constant in time, then

$$f(S) \sim (1 - S)^{\frac{1}{2}}. \quad (4.8)$$

However, we observe (see section 4.5) that the thickness of the intrusions varies with S . At high Reynolds number, the thickness h_i of an unstratified intrusion $S = 0$ is observed to be approximately one-half the total depth of the fluid, $h_i(S = 0) = \frac{H}{2}$. For the case where the buoyancy frequencies of both the intruding fluid and the ambient fluid are equal, the current can be viewed as having a current thickness equal to the full height of the fluid, $h_i(S = 1) = H$. For intermediate values of S , the vertical distance between isopycnals in the ambient fluid corresponding to the minimum and maximum densities of the intrusion varies linearly with S . Therefore, as a first approximation, we assume a linear increase in the thickness of the intrusion with S ,

$$h_i = \frac{H}{2}(1 + S). \quad (4.9)$$

Still ignoring the counterflowing gravity currents, but now relating the kinetic energy of the current to the available potential energy while taking into account the variation of the intrusion thickness with S , we find that

$$f(S) \sim \left(\frac{1 - S}{1 + S} \right)^{\frac{1}{2}}. \quad (4.10)$$

However, the counterflowing gravity currents above and below the intrusion also carry kinetic energy. In order to account for the energy in the counterflowing currents we note that (4.9) implies

$$h_a = \frac{H}{2}(1 - S). \quad (4.11)$$

Since there is no net volume flux across a vertical plane the speed of the counter-flows U_a is given by

$$U_a = \frac{h_i}{2h_a} U_i. \quad (4.12)$$

Finally, scaling the kinetic energy of both the forward and backwards propagating flows of varying thickness with the APE we obtain

$$f(S) \sim \frac{(1 - S)}{(1 + S)^{\frac{1}{2}}}. \quad (4.13)$$

The energy scaling models in (4.8), (4.10) and (4.13) will be compared to the results of laboratory experiments and numerical simulations in section 4.5.

4.4 Methods

4.4.1 Laboratory Experiments

Laboratory experiments were conducted in a channel with an ambient fluid with a fixed stratification $N_a = 1.47 \pm 0.02 \text{ s}^{-1}$, and for six values of the stratification ratio $S = \{0, 0.23, 0.38, 0.49, 0.65, 0.77\}$. The Reynolds number, based on the observed propagation speed and intrusion thickness, of the slowest propagating intrusion ($S = 0.77$) was found to be in excess of 10^3 , the value above which unstratified gravity currents are considered inviscid (Simpson [11]).

The experimental channel was 182 cm long, 23 cm wide, and 30 cm deep, with a vertical gate dividing the tank at a distance $L_{lock} = 63$ cm from an endwall. Removing the gate vertically set the two fluids into motion. The position of the gate was chosen to maximize the duration of the constant-velocity phase, while providing sufficient runout in the ambient fluid to observe the intrusion speed unaffected by internal waves reflected from the endwall of the tank. Sodium chloride was added to water to vary the density between 1.010 and 1.060 g cm^{-3} . Stratification was created using the double-bucket method (Oster [32]), and sponge floats were used to fill both sides of the lock gate simultaneously to $H = 20$ cm depth. Water samples were drawn every 2 cm in height from both fluids, and the densities were verified with an Anton-Paar 5000 DMA density meter with an accuracy of

$10^{-8} \text{ kg m}^{-3}$. Only density profiles with levels of neutral buoyancy deviating less than $\pm 2 \text{ mm}$ from $H/2$ were included.

The channel was illuminated by a vinyl light sheet placed against the back wall. A CCD camera (1390 x 1024 pixel resolution) was positioned normal to, and 5 m away from, the front wall. Sucrose-based food coloring, with a molecular diffusion coefficient approximately one third that of sodium chloride, was added to the lock-fluid double-bucket system as a passive tracer of density. Images of the current were recorded directly onto a PC via DigiFlow software (Dalziel [34]) at 12 frames per second. The same software was used to track the horizontal and vertical extent of the dyed intrusion. The attenuation of the light passing through the tank was measured and used, via calibration, to provide a width-averaged measure of the density. Mixing at the boundaries of the current decreases the dye concentration and therefore the light attenuation. To provide a conservative estimate of the thickness of the current, we defined the current edges by a 25% reduction in the light attenuation of the intruding fluid relative to the average initial light attenuation in the lock.

The intrusion thickness was measured at each frame as the horizontal average of the thickness of a 10 cm-long section of intrusion, as determined by the vertical extent of the dyed region, centered 7 cm behind the lock gate. Distance-time $x-t$ plots of the position of the front of the intrusion were created by projecting the density field onto the horizontal axis at each frame. A linear regression was then fitted to the plot to estimate the constant velocity of the progressing density front (Sutherland [36]).

4.4.2 Numerical Simulations

Direct numerical simulations of lock releases were conducted in two dimensions for two values of the ambient buoyancy frequency $N_a = 0.5 \text{ s}^{-1}$ and 1.0 s^{-1} , and for eleven equally spaced values of the stratification parameter $S = 0, 0.1, \dots, 1$.

For the simulations reported here, the kinematic viscosity $\nu = 0.01 \text{ cm}^2\text{s}^{-1}$ and $Sc = 1$. For salt water $Sc \gg 1$ and, although the choice of $Sc = 1$ leads to an overestimation for the diffusivity of salt, this choice is necessary to maintain

numerical stability. This is standard practice in these type of calculations and appears not to lead to significant changes in the dynamics of the flow, see e.g. Härtel *et al.* [35]. Mass transfer from the current is determined by the Péclet number $Pe = \frac{N_a h_i^2}{\kappa}$, where κ is the molecular diffusivity of mass. At high values of $Pe \gg 1$, molecular transport is not important and instead the density of the current changes, if at all, by mixing with the ambient fluid. At high Reynolds numbers the choice of $Sc = 1$ means that the Péclet number is also large so that the effects of mass diffusion, like those of viscosity, are expected to be small.

A slightly modified version of the open source DNS algorithm Diablo (full details available at <http://renaissance.ucsd.edu/fccr/software/Diablo.html>) was used to solve the above equations. The code in its current form requires periodic boundary conditions in the streamwise direction, and the flow here is not periodic in the streamwise direction. In order to achieve periodicity, and enable a Fourier decomposition of the flow variables in this direction, a domain twice the length of the domain shown in figure 4.1 was chosen. This allows reflectional symmetry about the vertical mid-plane in the initial condition (i.e. lock fluid starts in the middle and propagates equally in both horizontal directions). In the vertical direction periodicity does not occur. Derivatives in this direction were evaluated using centered finite-differences with no-slip boundary conditions at the top and bottom boundaries.

A mixed method using third-order, low-storage Runge-Kutta-Wray (RKW3) scheme and a Crank-Nicholson (CN) scheme was used to advance the flow in time with $\Delta t = 0.001$ s. Diffusive terms in the wall-normal direction were treated implicitly, while all other terms are treated implicitly. Uniform grids were selected in all directions.

As with the laboratory experiments, the flow is stationary at $t = 0$. In order to minimize Gibbs phenomena in the streamwise direction, the vertical interfaces that define the lateral boundaries of the lock were smoothed using a hyperbolic tangent profile.

Parameters were chosen so that the Reynolds number, $Re = \frac{N_a h_i^2}{\nu}$, based on the intrusion thickness h_i , is sufficiently large (i.e. $> 10^4$) that viscous effects

are negligible and the flow exhibits the characteristic features of two-dimensional turbulent gravity currents such as the roll up of Kelvin-Helmholtz billows behind the gravity current head.

The numerical simulations were allowed to progress until the finite length of the domain began to influence the intrusion. In the same manner as in the experiments, the intrusion thickness was estimated at each frame as the horizontal average of a 10 cm section of intrusion thickness centered 7 cm behind the lock gate.

4.5 Results

Simulations for $N_a = 0.5 \text{ s}^{-1}$ and $N_a = 1 \text{ s}^{-1}$ and experiments for $N_a = 1.47 \pm 0.02 \text{ s}^{-1}$ were conducted over the range of stratification ratios $0 \leq S < 1$. An example of the current at various times from the numerical simulations is shown in figure 4.2 for $S = 0.2$ and $S = 0.8$. A similar series from the experiments at the same dimensionless times is shown in figure 4.3 for $S = 0.23$ and $S = 0.77$. Ignoring the exaggerated billows in the two-dimensional simulations, which in practice breakdown as a result of three-dimensional instabilities that are precluded from the calculations, we observe excellent agreement between the experimental and numerical images. The shapes of the simulated intrusions agree well the experimental images, although the front of the intrusion is more ragged at $S = 0.8$ in the experiments. The reduction in the intrusion speed and its increase in thickness as S increases are seen in both the experiments and the simulations. Quantitatively, the experiments and the simulations agree well, even though they are for different values of N_a . This agreement, achieved by non-dimensionalizing time with the ambient buoyancy frequency, supports the dimensional analysis leading to (4.5).

The intrusions taper towards the front similar to those observed for unstratified intrusions (Bolster *et al.* [4] – see also figure 4.6. There is no evidence of a ‘head’ typical of gravity currents in unstratified environments. Close inspection of the edges of the stratified intrusions shows some irregular structures. These have not been observed on either gravity currents or unstratified intrusions and are a



Figure 4.2: Snapshots of the numerical simulations for $S = 0.20$ (left) and $S = 0.80$ (right) for $N_a = 1 \text{ s}^{-1}$ at $N_a t = 10, 20$, and 30 . The dashed gray line denotes the initial position of the gate. The motion of the lock fluid is visualized using a passive tracer.

result of the internal stratification within the intrusion. We will examine them further below.

In order to test the predictions (4.8), (4.10) and (4.13) for the variation of front speed with S , we need to measure how the thickness of the intrusion varies. As observed in figures 4.2 and 4.3, the thickness of the intrusion increases with increasing S , while the thicknesses of the backflows decrease. As noted above, the thickness is not uniform in x , and we observe sloping boundaries between the intruding and ambient fluid narrowing toward the front of the intrusion. It is for this reason that we chose to measure a representative thickness taken to be the spatial and temporal average thickness of a 10 cm-long region centered 7 cm back from the gate position. The consequences of choosing an alternative location for the thickness measure are discussed in section 4.7.

A plot comparing the intrusion thickness h_i as a function of S for the laboratory experiments and numerical simulations, to the assumed linear variation in current thickness (4.9), is presented in figure 4.4. At lower values of $S < 0.5$, both the numerical and experimental results agree within the error bounds, which for the simulations are large as a result of the billows referred to above, and they agree well with the linear approximation (4.9). At higher values of S the agreement is not as good: the experimental thicknesses are less than the simulations, and the latter show better agreement with (4.9) over the entire range of stratification ratios.

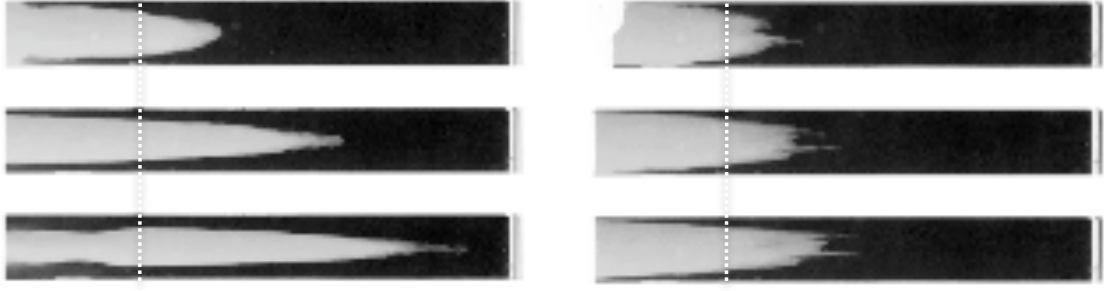


Figure 4.3: Snapshots of the laboratory experiments for $S = 0.23$ (left) and $S = 0.77$ (right) for $N_a = 1.5 \text{ s}^{-1}$ at the same dimensionless times $N_a t = 10, 20$, and 30 as in figure 4.2. The dashed white line denotes the initial position of the gate. The intrusion fluid is visualized with dye.

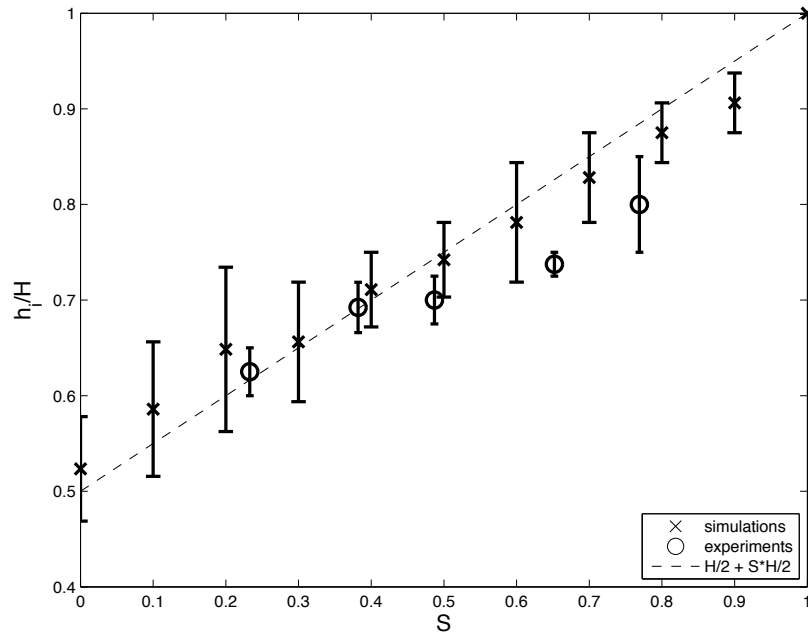


Figure 4.4: A comparison between dimensionless intrusion thickness h_i/H , where H is the total fluid depth, as a function of the stratification ratio S for experiments (circles), simulations (crosses) and the thickness assumed in the energy balance model (4.9) (dashed line). The thickness in the experiments was measured at each time as the 10 cm spatial average of intrusion thickness centered 7cm behind the lock gate and the resulting time averages and standard deviations are shown.

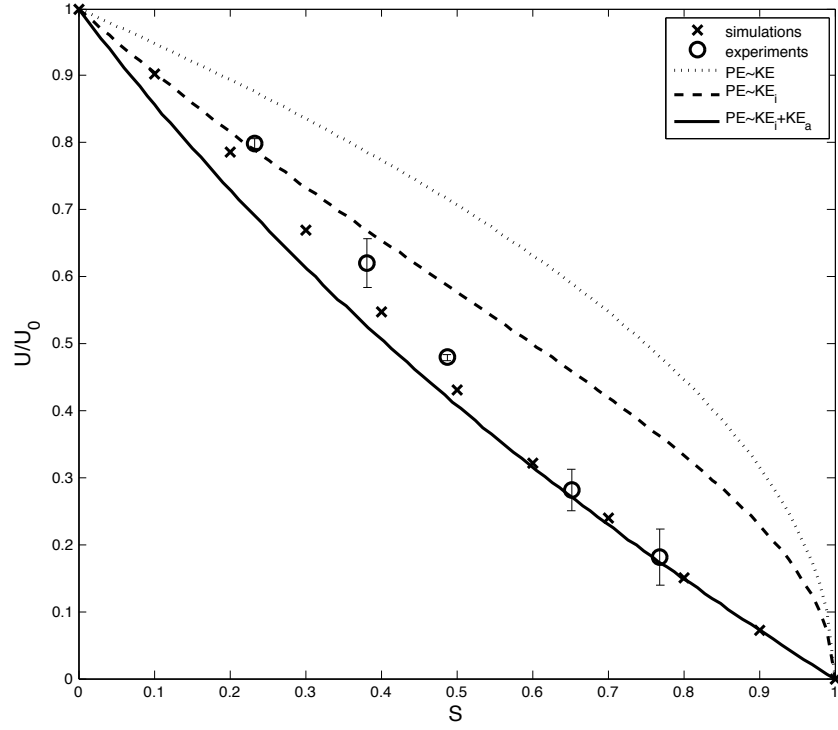


Figure 4.5: A comparison between dimensionless intrusive gravity current speed in the experiments (circles), simulations (pluses), and model predictions (curves) as a function of stratification ratio S . The three models of increasing complexity approximate the variation of U_i with S , directly from the potential energy (4.8, dotted line), and scaled by a linear increase in current thickness with S (4.10, dashed line), and incorporating the counterflow (4.13, solid line). U_0 is taken to be the speed of a well-mixed intrusion $U_0 = 0.125N_aH$.

As in the case of unstratified intrusions into a linearly stratified ambient fluid (Bolster *et al.* [4]), the stratified intrusions were observed to travel at a constant speed after an initial period of acceleration once the lock gate was removed. Figure 4.5 displays the dimensionless front speed as a function of S . Intrusion speeds measured in the laboratory experiments and numerical simulations agree well over the entire range $0 \leq S < 0.8$. As noted in section 4.3 the bounds for the velocity are given by Bolster *et al.* [4] for $S = 0$, and by inspection ($U_i = 0$) at $S = 1$. Between these bounds, the available potential energy, and therefore the intrusion velocity, decreases monotonically with increasing S , as observed.

Curves corresponding to the predictions (4.8), (4.10) and (4.13) are given in figure 4.5. The simplest case, (4.8), in which only the motion of the intrusion itself is included, and which ignores changes in intrusion thickness with S , over-predicts the speed at all values of $S > 0$. When the variation in intrusion thickness is included (4.10) the model predictions improve but still over-estimate the observed and calculated speeds particularly at large S .

The theoretical estimate (4.13) that includes both the variation in intrusion thickness and the kinetic energy of both the intrusion and the two counterflowing gravity currents, provides the best agreement with the observed and calculated speeds. Agreement between the first order model and the experimental and numerical results is better than 5%, over the range $0.3 \leq S < 0.9$. Further, the curvature of (4.13) has the opposite sign to the two simpler estimates (4.8) and (4.10), and is consistent with the curvature observed in the data at large S . For values of $S < 0.3$, the data lie between the curves given by (4.10) and (4.13).

4.6 Role of internal stratification

Compared to unstratified intrusions in a linearly stratified ambient fluid studied by Bolster *et al.* [4], the presence of stratification in the intruding fluid changes both the shape and the speed of the intrusion. Figure 4.6 shows a comparison between intrusions for $S = 0, 0.23$ and 0.77 . For the unstratified intrusion $S = 0$, the front takes the shape of a classical rounded plug-of-fluid shape first

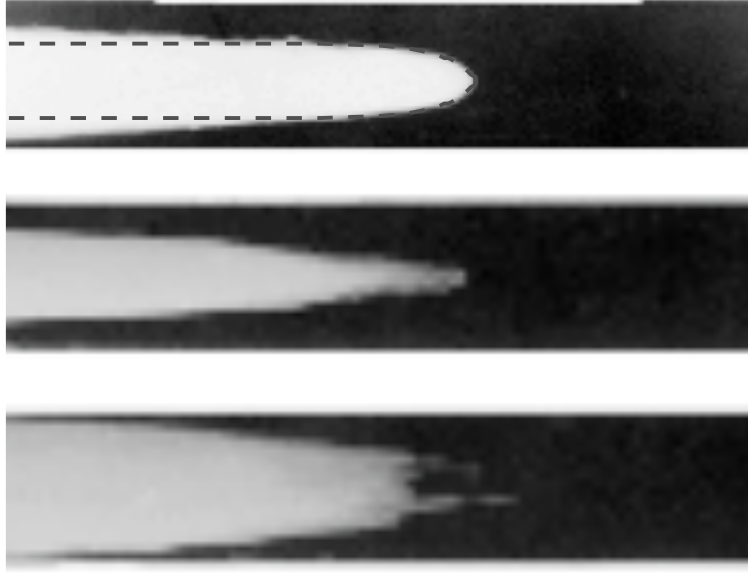


Figure 4.6: A comparison of the front shape in laboratory experiments at $N_a = 1.47 \pm 0.02 \text{ s}^{-1}$ for three different stratification ratios, $S = 0, 0.23$ and 0.77 . The presence of stratification within the intrusion generates internal circulation within the intrusion and its thickness increases with increasing S . The shape of an irrotational gravity current given by Benjamin [5] is superimposed on the unstratified intrusion $S = 0$.

described by Benjamin [5]. The theoretical shape predicted by Benjamin [5] for an irrotational gravity current and ignoring any internal flow within the current, which is also a good approximation for the shape of an interfacial intrusion on a sharp density interface (Lowe *et al.* [19]), is superimposed on the unstratified intrusion in figure 4.6. The rounded front of the intrusion agrees well with this shape, suggesting that there is little relative flow within the intrusion. Further back from the front the top and bottom surfaces of the intrusion continue to slope and the intrusion continues to increase in thickness towards the rear, in contrast to the gravity current.

In addition to increasing in thickness as S increases, stratified intrusions do not exhibit the rounded front observed in the $S = 0$ case. The front is more pointed for the case $S = 0.23$, and shows an almost vertical face with some smaller intrusions of dye fluid for the case $S = 0.77$. The unstratified intrusion flows along

the isopycnal surface in the ambient fluid corresponding to its internal density and that isopycnal splits along the top and bottom surfaces of the intrusion. When $S > 0$, this simple splitting of the ambient fluid above and below the intrusion is not possible, since the density stratification within the intrusion implies that a range of the ambient density field is within the density variations within the intrusion.

Figure 4.7 shows the calculated density contours for stratified intrusions $S = 0.2$ and $S = 0.8$. The contours shown in each case correspond to the full density range within the intrusion and the same isopycnals in the ambient fluid. So, in the $S = 0.2$ case, only isopycnals near the mid-depth of the ambient fluid are marked. In this case, small density inversions occur at the edges of the intrusion as heavier fluid is raised above the intrusion and lighter fluid is pushed below it. These inversions are distinct from the larger-scale billows caused by shear instability on the edges of the intrusion (figure 4.2). They can be seen in the experimental images of the stratified intrusions in figures 4.3 and 4.6, and in the simulations shown in figure 4.2. These inversions occur because of the variation of density within the intrusion, since, for example, the density of the mid-depth isopycnal in the ambient, which bifurcates at the intrusion front, is greater than all of the fluid in the upper half of the intrusion.

Distortions of the isopycnal surfaces upstream of the intrusion are also seen in figure 4.7. As the intrusion forcing is centered about the midplane of the tank, we expect mode 2 waves to be strongly forced. Bolster *et al.* [4] determined that well-mixed intrusions in a linearly stratified ambient fluid travel at speeds subcritical to mode 1 and mode 2 waves. The introduction of stratification in the intruding fluid reduces its speed, and indeed, the spreading apart of the isopycnals above and below the midplane in the ambient fluid upstream of the current is consistent with the presence of a mode 2 disturbance.

For the more stratified intrusion $S = 0.8$, the adjustment of the isopycnals is less than for the $S = 0.2$ case. There is some compression of the intrusion isopycnals near the front of the intrusion and an upstream disturbance in the form of a mode 2 wave. There is an adjustment region ahead of the intrusion front, but

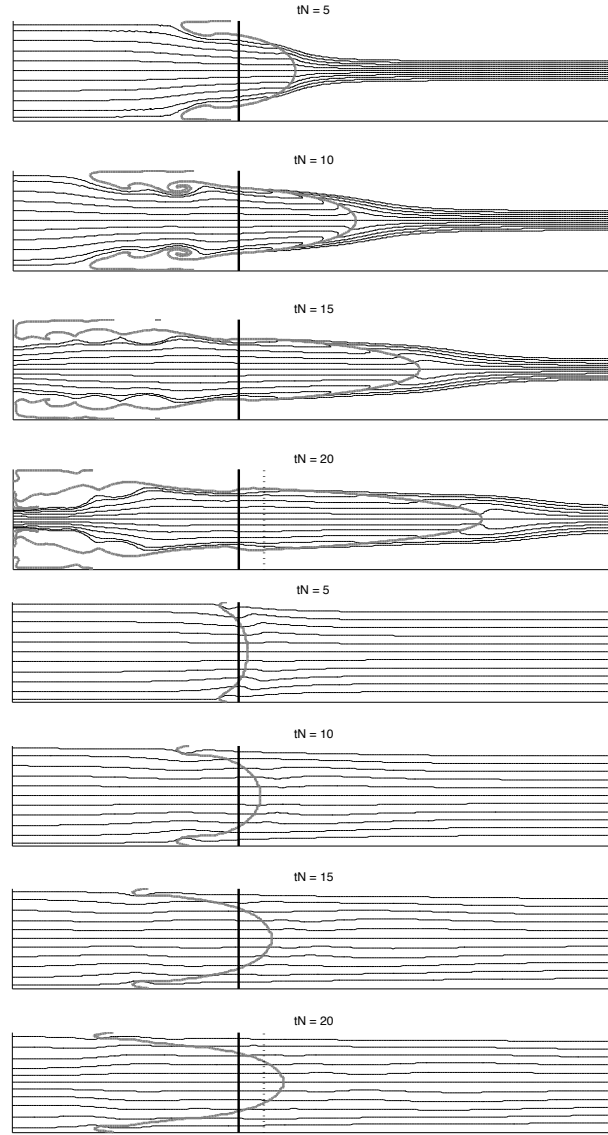


Figure 4.7: Snapshots of the density contours for $S = 0.20$ and $S = 0.80$ ($N_a = 1 \text{ s}^{-1}$) at $N_a t = 5, 10, 15$, and 20 , calculated from the simulation data. The black lines denote density contours evenly spaced across the entire range of intrusion densities, and the corresponding isopycnals in the ambient fluid. The gray lines denote the boundary between the intrusive and the ambient fluids, the black line denotes the initial position of the gate, and the dashed black line denotes the vertical transect described in figure 4.8. Note the pronounced step in the density contours at the transition between the two fluids in the more energetic $S = 0.2$ case, the horizontal gradients in density created within and ahead of the intrusion, and finally the adjustment of the upstream ambient stratification.

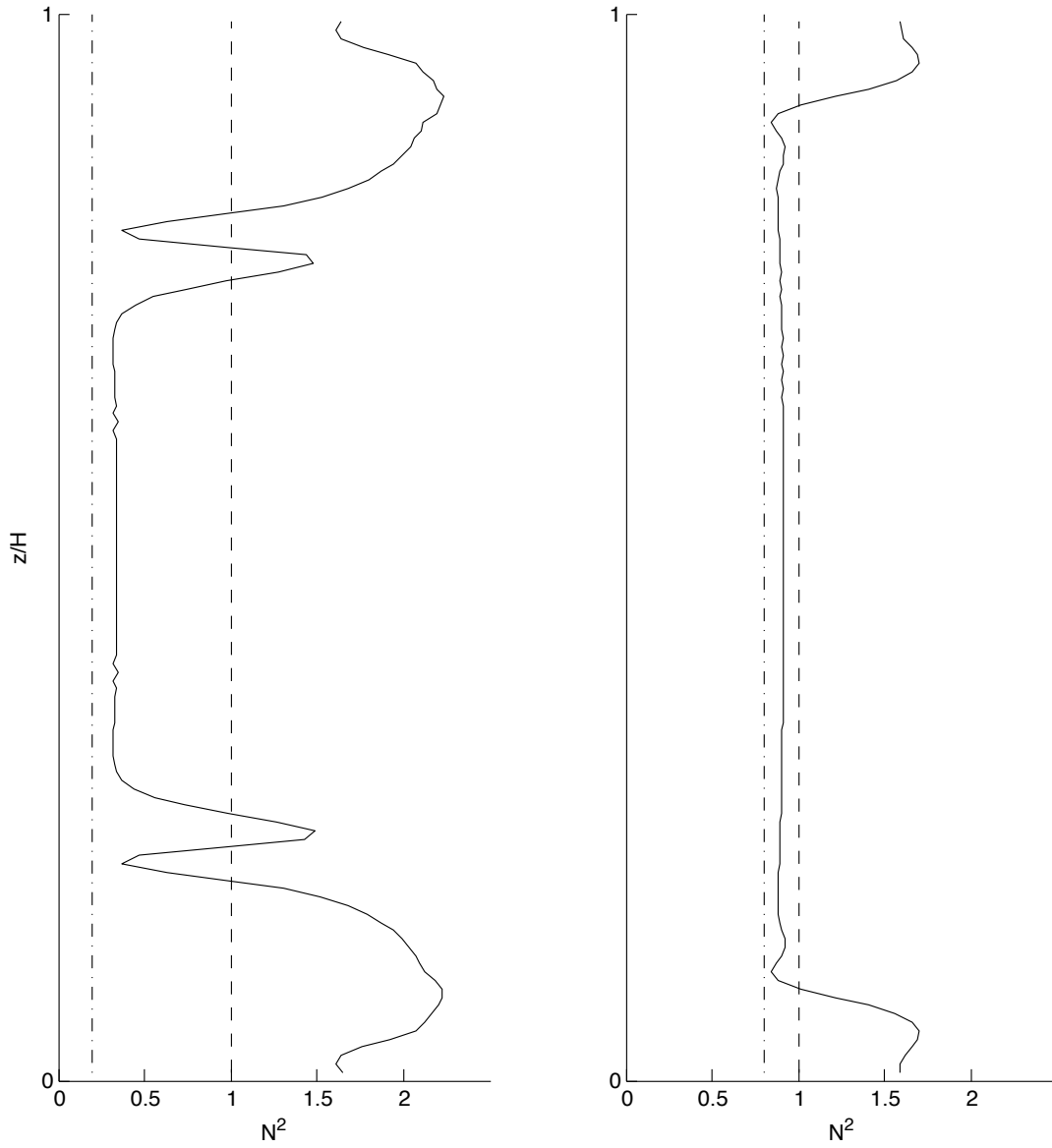


Figure 4.8: Vertical transects of the buoyancy frequency, for $S = 0.2$ (left) and $S = 0.8$ (right), taken 5 cm into the ambient fluid from the gate position at $N_a t = 20$ (See figure 4.7). The dash-dotted line and the dotted lines denote the initial buoyancy frequency profiles of the intruding and ambient fluids, N_i and N_a , respectively. The solid line is the instantaneous buoyancy frequency as a function of height at the given x location. Note that the buoyancy frequency of the intruding fluid (closer to the mid-depth) reaches an intermediate value between the N_i and N_a , while the counter-flowing boundary gravity currents also display an increased buoyancy frequency.

no evidence in this case of overturning or statically unstable regions, even though some are observed on the images in figures 4.2 and 4.3. It appears that the dye distortions remain after the instabilities that generated them have decayed.

The compression of the isopycnals within the intrusion and also in the counterflowing gravity currents above and below the intrusion change the stratification in those flows. Figure 4.8 shows vertical profiles of buoyancy frequency N at a location ahead of the original lock gate position (see figure 4.7) at $N_a t = 20$. Also shown on the figure are the values of the initial buoyancy frequencies in the intrusion and the ambient fluid, N_i and N_a , respectively. In both cases the stratification within the intrusions remains linear and increases from its initial value to a constant value of N between N_i and N_a . The ambient fluid in the counterflowing gravity currents also increases in stratification as the fluid above and below the intrusion is compressed vertically. The edges of the intrusion are marked by rapid increases and decreases in N associated with the local distortion of the density field.

The horizontal density gradients that occur within the intrusion as a result of the compression of the isopycnals towards the front generate internal flow. Vorticity is produced by the baroclinic generation term $\nabla p \times \nabla \rho$, and the sign of this term is such as to produce positive vorticity in the upper half of the intrusion and negative vorticity in the lower half. This produces a dipole-like flow towards the front of the intrusion along the middle and return flow along the top and bottom boundaries. This internal flow is consistent with an elongation of the front of the intrusion from the irrotational shape observed in the unstratified case (figure 4.6), and the return flow is consistent with the distortion of the isopycnals observed for the case $S = 0.2$ (figure 4.7).

4.7 Discussion and conclusions

This chapter examines the mutual adjustment of two stratified fluids instantaneously brought into contact in a channel by the removal of a vertical barrier. The fluids are stratified with linear variations of density with depth, but with dif-

ferent vertical density gradients. We have restricted attention to the case where the two fluids have the same mean densities which occur at the same depth, in this case the mid-depth of the channel. In this case the centers of mass of the two fluids are at the same height, and the fluids have no tendency to flow one under the other. The motion is vertically symmetrical about the mid-depth of the tank with the less stratified fluid flowing into the more strongly stratified fluid as an intrusion centered at the mid-depth. The more stratified fluid flows in the opposite direction as two stratified gravity currents, one above the intrusion along the upper boundary of the fluid and one below along the lower boundary.

This configuration has two limits. The first is when one of the fluids is unstratified, in which case the flow is that of an unstratified intrusion propagating along the mid-depth of a stratified fluid. This case has been studied previously (Bolster *et al.* [4]) and its properties are known. The other limiting case is when the density gradients of the two fluids are the same. In this case the two fluids are indistinguishable and nothing happens.

Through lock-exchange laboratory experiments and two-dimensional numerical simulations we have examined the behavior of the system between these two limits in terms of the stratification ratio $S \equiv \frac{N_i^2}{N_a^2}$. The unstratified intrusion corresponds to $S = 0$ and the two identical fluids to $S = 1$. In all cases $S < 1$ we observe that the flow takes the form of an intrusion of the less stratified fluid (N_i) into the more strongly stratified fluid. This intrusion propagates along the mid-depth of the channel and two counterflowing gravity currents flow above and below the intrusion.

One objective was to predict the speed of the intrusion as a function of S . We observed that the intrusion travelled at a constant speed, which decreased as a function of increasing S , and found good agreement between the measured speed in the experiments and that calculated in the simulations. We developed a model for the exchange flow that assumes that the available potential energy of the initial configuration is converted at a constant rate into the kinetic energy of the intrusion and the gravity currents. As expected the model also predicted a reduction in speed with S , and gave reasonably good agreement with the experimental and numerical

data (figure 4.5).

The model relies on an estimate of the thickness of the intrusion and the counter-flowing gravity currents. We observed that the intrusion thickness increased with S , which is to be expected as the extreme densities within the intrusion correspond to a wider region about the mid-depth of the ambient fluid as S increases. We approximated this increase as a linear function of S , which is consistent with the width of the corresponding region in the ambient fluid, and found reasonable agreement with the data (figure 4.4).

The sloping boundaries of the intrusions introduce variability to the measurements of the current thickness as a function of horizontal location. Measurements of the current thickness within the lock are at a thicker part of the current, and therefore likely to be an overestimate. To examine the sensitivity to the choice of the horizontal position at which the thickness is measured, we reduce the assumed intrusion thickness (4.9) by a factor $c < 1$, and write the intrusion thickness as

$$h_i = c \frac{H}{2} (1 + S). \quad (4.14)$$

By the same energy argument presented in (4.13), we arrive at an expression for the dependence of the velocity on S

$$f(S) \sim \frac{(1 - S)}{(1 + S)} \frac{(1 - \frac{\epsilon}{2}(1 - S))}{(1 - \frac{\epsilon}{2})}. \quad (4.15)$$

The modeled speeds for various values of c are plotted in figure 4.9. Compared with the case presented in section 4.5 ($c = 1$), the speeds predicted using a reduced thickness are faster over the range of intermediate stratification ratios as c decreases. At lower stratification ratios, $S < 0.5$, the use of a reduced current thickness predicts intrusion speeds in closer agreement with experimental and numerical observations. The boundaries of low S intrusions are more sloped (figures 4.3 and 4.6), and so are better represented by a reduced thickness than that used in section 4.5, while intrusions at higher stratification ratios $S > 0.5$ are better described by the full-thickness energy balance models. In any event these changes are small and the sensitivity to the exact value chosen for the intrusion thickness is small: a reduction of the assumed current thickness by 40% results in

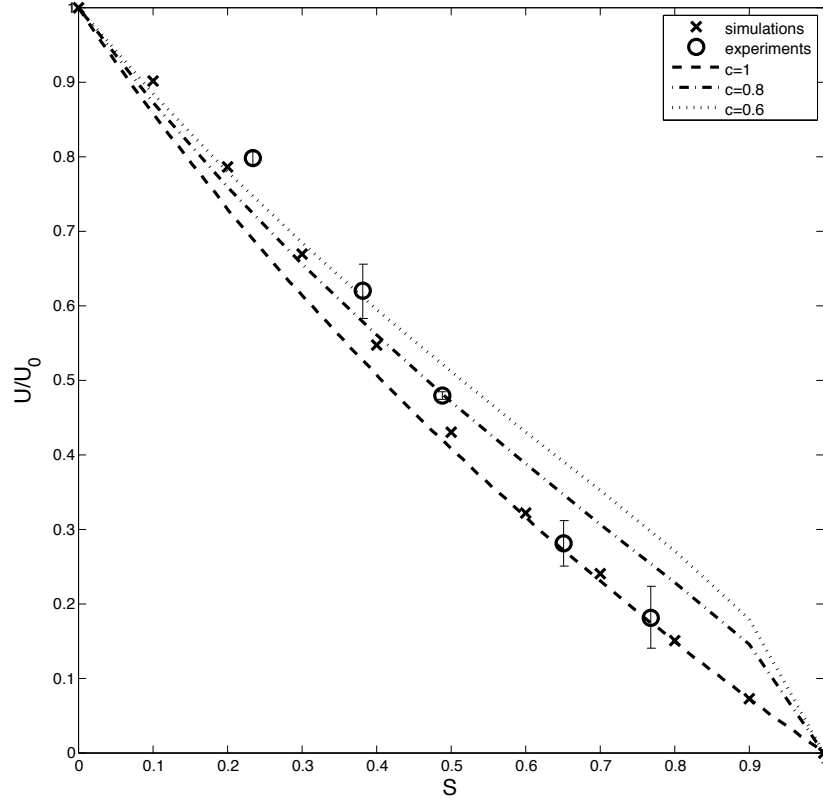


Figure 4.9: A comparison between modeled dimensionless intrusive gravity current speed presented in figure 4.5 (dashed line) and speeds predicted based upon a reduced intrusion thicknesses. Energy balance model predictions of intrusion speed where the well-mixed intrusion thicknesses is $0.5H$, $0.4H$, and $0.3H$ ($c = 0.8$ and 0.6) are shown as dashed, dash-dotted, and dotted lines, respectively. Note that relatively large reductions in the thickness of the intrusion results in a less significant increase in predicted speed, and that at lower values of S , this reduced thickness provides an improved fit to the numerical and laboratory data.

a maximum change in predicted speed of less than 15%, indicating the model is relatively robust to inaccuracies in the assumed current thickness.

The agreement between this energy-conserving model and the experiments and simulations is consistent with previous work on interfacial intrusions (Cheong *et al.* [6]) and unstratified intrusions in a linearly stratified ambient fluid (Bolster *et al.* [4]). This conversion of available potential energy to kinetic energy of the intrusion and ambient flows ignores dissipative processes such as turbulence and mixing (and viscosity, but this is small at the high Reynolds numbers we are considering). It also ignores energy escaping into upstream waves, which are undoubtedly present in these flows. We conclude, that while these processes occur, their impact on the overall energetics is small and can be ignored to first order.

As noted in section 4.6 internal waves are present in the stratified ambient fluid. They occur both upstream of the intrusions which are subcritical to, at least, long waves of vertical modes 1 and 2. Waves are also present in the ambient fluid behind the front of the intrusion. It is also likely that there are internal waves within the stratified intrusion itself, although they have not been clearly identified. The effect of these waves needs further study, which is also the case for unstratified gravity currents (Maxworthy *et al.* [23]) and intrusions (Bolster *et al.* [4]). As in the present study, the speed of the gravity current and intrusion could be predicted while ignoring the internal waves entirely. On the other hand, for unstratified intrusions recent experiments by Monroe *et al.* [28] show quite different behavior which appears to result from the influence of internal waves reflected from the back of the lock, causing little evidence of a constant-velocity phase.

The model also ignores the internal circulation that results from the internal stratification in the intrusion. We observe that baroclinic generation of vorticity generates a dipolar internal flow that distorts the isopycnals within the intrusion and changes the shape from the unstratified intrusion which is well represented by an irrotational interior. We also observe that adjustment of the isopycnals leads to small regions of static instability along the top and bottom of the intrusions. All of these features are excluded from the bulk model that we have presented.

Consequently, they seem to play only a secondary role in the bulk adjustment process of two stratified fluids.

Finally, we note that in the case $S \rightarrow 1$, the interchange between the two fluids decreases and the flows become weak. While it may seem that this limit is of little practical relevance as everything evolves very slowly relative to the smaller values of S , one should be cautious before disregarding it. In certain practical cases it has been shown that slow exchange flows are the source of unexpected coastal pollutants (Bolster *et al.* [41]).

Material drawn from this chapter has been published in the *Journal of Fluid Mechanics*, (2010), Maurer, B. D., Bolster, D. T., and Linden, P. F. (Cambridge University Press).

Chapter 5

Adjacent discrete stratifications

5.1 Abstract

We present a primarily numerical study of the gravity-driven interleaving of two stable discretely stratified fluids at high Reynolds numbers. The two fluids are initially at rest in a horizontal channel and are separated by a vertical barrier which is removed to start the flow. We consider the case in which the layers of constant density are of equal thickness, density interfaces within one fluid are vertically staggered by half the layer thickness relative to the second fluid, and the density differences between vertical adjacent layers are all equal. The resulting flow consists of multiple interleaving interfacial gravity currents (IfGCs). Studies of a single intrusion propagating into a two-layer ambient fluid by Cheong *et al.* [6] and Flynn & Linden [22] show that the speed of an IfGC is independent of the density of the intrusion, and determined instead by the vertical density difference between the ambient layers. Varying the average density of one fluid relative to another while maintaining equal vertical density differences between layers, we show that a simple extension of these findings to the interleaving of multiple IfGCs fails, and suggest that this failure is due to the coupling of interfacial waves across constant density layers.

5.2 Introduction

Interfacial gravity currents (IfGCs) occur when lateral differences in density drive horizontal flow along a sharp density interface between two ambient fluid layers. Strong pycnoclines can be found in the atmosphere, oceans, seas, lakes, as well as industrial and architectural flows. Examples include atmospheric inversions,

the thermocline at the base of the mixed layer in the ocean, the halocline beneath riverine inputs into ocean, seas, or lakes, and the strong temperature stratification created by modern low-energy architectural ventilation schemes. The presence of laterally adjacent fluid of an intermediate density, perhaps created by diapycnal mixing, drives interfacial gravity currents along these density interfaces, transporting mass, momentum, energy, and particulates (e.g. nutrients, phytoplankton, or pollutants) (Simpson [11]).

In the laboratory, interfacial gravity currents can be created via a lock release experiment, where the intruding fluid density ρ_i is less than the lower ambient layer density ρ_L and greater than that of the upper ambient layer density ρ_U . Removing the barrier between the lock and the ambient fluids allows the intrusion to propagate along the pycnocline between the upper and lower fluid layers (see figure 5.1). After a brief period of acceleration, the IfGC propagates at a constant velocity U (Britter & Simpson [20]). In channel lock release experiments, cross-tank variations are observed to be small in comparison to streamwise variations, allowing the problem to be considered in two dimensions. Since seminal work by Holyer & Huppert [16], a number of studies have examined interfacial gravity currents into two-layer ambient fluids, such as Britter & Simpson [20], Faust and Plate [37], Mehta *et al.* [42], Lowe *et al.* [19], Sutherland *et al.* [17], Ungarish [38], Cheong *et al.* [6], Flynn & Linden [22], Sutherland & Nault [43], Ooi *et al.* [44], Flynn *et al.* [45], and Nokes *et al.* [39]).

For the simple case of a boundary gravity current with density ρ_i propagating along the lower boundary of an ambient fluid of density ρ_a and depth d , dimensional analysis suggests that the constant speed of the current U be a function of ρ_i , ρ_a , and d (Yih [2]).

$$U = Fr_0 \sqrt{g'_{iU} d} \quad (5.1)$$

where $g'_{iU} \equiv \frac{g(\rho_i - \rho_a)}{\rho_0}$ is the reduced gravity between the two fluids and ρ_0 is a reference density. Benjamin [5] reasoned that $Fr_0 = \frac{1}{2}$ for energy-conserving inviscid boundary currents. Sutherland *et al.* [36] found empirically $Fr \sim 0.48$ for high Reynolds number boundary gravity currents, ($Re \geq 2000$, Simpson & Britter [26]).

This simple boundary case can be extended to doubly symmetric interfacial

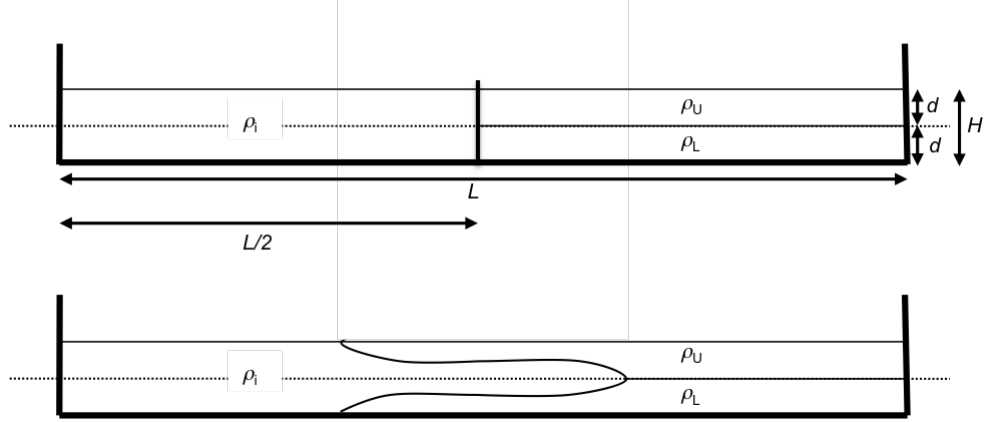


Figure 5.1: Schematic showing the initial conditions (above) for a lock-release of a single ‘doubly symmetric’ interfacial gravity current. Here, the ambient fluid is made up of two-layers of equal depth $d = H/2$, and the density of the intruding fluid is the average of the two ambient fluid layer densities $\rho_i = (\rho_L + \rho_U)/2$. At time $t = 0$, the gate is removed, and the IfGC propagates along the interface in the ambient fluids with velocity U (below). The interfacial gravity current is symmetric about the dotted line and behaves as two symmetric boundary currents in a fluid of depth d .

gravity currents in a fluid of depth H , where the lower-layer depth d_L is equal to the upper-layer depth d_U , and the density of the intruding fluid is the average of the two-layer densities, $\rho_i = (\rho_L + \rho_U)/2$. Taking the IfGC to be composed of two symmetric inviscid boundary gravity current exchanges reflected about the midplane of the experiment as in Lowe *et al.* [19], the relevant heights and density differences scales are now d and $g'_{Li} \equiv g \frac{(\rho_L - \rho_i)}{\rho_0}$, $g'_{iU} \equiv g \frac{(\rho_i - \rho_U)}{\rho_0}$. Defining a reduced gravity of the interface, $g'_{LU} \equiv g \frac{(\rho_L - \rho_U)}{\rho_0}$, Lowe *et al.* [19] note that for this doubly symmetric case, $d = H/2$ and $g'_{Li} = g'_{iU} = g'_{UL}/2$. The predicted IfGC velocity is therefore,

$$U = Fr_0 \sqrt{g'_{Li} d}, \quad (5.2)$$

$$= Fr_0 \sqrt{g'_{iU} (H - d)} \quad (5.3)$$

$$= Fr_0 \frac{1}{2} \sqrt{g'_{UL} H}, \quad (5.4)$$

implying a Froude number for doubly symmetric interfacial intrusions, $Fr = \frac{1}{2} Fr_0 = 0.25$.

For a “singly symmetric” IfGC, where the ambient layer depths are equal but the intrusion density is not the depth-weighted average of the ambient layer densities, the interfacial gravity current sinks or rises relative to the interface depth, propagating at a speed that is independent of the intrusion density ρ_i . The first accurate predictions of asymmetrical IfGC speeds came from a heuristic energy scaling argument advanced by Cheong *et al.* [6], who noted that the available potential energy of an interfacial gravity current entering a two-layer ambient fluid departs quadratically from the equilibrium solution at the half-height. They scaled the current speed U by this available potential energy, taking the appropriate limits of the doubly symmetric IfGC to (5.4), and IfGCs at the boundaries to (5.1) at the lower and upper boundaries, 0 and H . In doing so, they arrived at the expression describing the IfGC speed as a function of interface height and reduced gravities:

$$U_h = Fr_0 \sqrt{\left(\frac{h}{H}\right)^2 - 2\left(\frac{h}{H}\right)\left(\frac{g'_{iU}}{g'_{LU}}\right) + \left(\frac{g'_{iU}}{g'_{LU}}\right)} \sqrt{g'_{LU}H}. \quad (5.5)$$

The authors note that when $h/H = 1/2$, (5.5) is independent of the intrusion density ρ_i , collapsing to (5.4).

These “singly symmetric” IfGCs generate upstream interfacial waves, as first noted by de Rooij *et al.* [21]. Early efforts to develop analytical models of IfGCs ignored this upstream displacement, and resultingly overestimated the front speed, (e.g. Holyer & Huppert [16]). A Benjamin-style [5] IfGC model incorporating the upstream displacement of the interface in a balance of mass, momentum, and energy was developed by Flynn & Linden [22]. They found that though little energy was lost to the upstream displacement of the interface, the wave serves to change the local front conditions driving. For example, “heavy” currents sink relative to the interface, displacing mass in the lower-layer which, by continuity, must raise the interface upstream of the current. Elevating the interface increases the average density into which the current propagates, reducing the local hydrostatic pressure difference at the front. This results in a decrease in speed of the current, maintaining (5.4).

Though many models of interfacial gravity currents have explicitly incorporated the reciprocal propagation of *boundary* gravity currents at the upper and

lower boundaries, such as Holyer & Huppert [16], Flynn & Linden [22], Maurer *et al.* [3]; to our knowledge, none have extended their models to include the interleaving of high Reynolds number Boussinesq interfacial gravity currents. This study aims to describe the interleaving process of multiple IfGCs as it varies with the difference between the average densities of the two stably stratified fluids. We restrict our scope to adjacent discrete stratifications where the initial conditions can be conceptually simplified so as to allow the application of (5.4) for the IfGC at each density interface (details provided in section 5.3)

In section 5.3 we present our velocity model which assumes a linear addition of a background flow to the locally determined interfacial gravity current velocity. We describe the 2-D direct numerical simulations and laboratory experiments in subsection 5.4.1 and subsection 5.4.2. Section 5.5 presents the results of the numerical experiments in detail and compares the results with the theory developed in section 5.3. We outline our conclusions in section 5.6.

5.3 Model

Similar to the approaches presented in section 5.2, we consider a scaling argument about lines of symmetry to simplify a multiply layered problem. As such, we expect this model to apply to any even number of interleaving inviscid IfGCs. Within this section, and for results we present in detail in section 5.5.2 we have chosen a system of ten interleaving IfGCs.

We consider two adjacent discretely layered stratified fluids of equal total depth H and equal lengths $L/2$, where L is the total length of the channel. Each fluid is made up of six layers. To the left of the gate, the uppermost layer is of thickness $d = H/11$, and all other layers within the lock are of thickness $2d$. Similarly, to the right of the gate, the bottommost layer is of thickness d , and all other layers are of thickness $2d$. This serves to stagger the stratifications such that the interfaces of the fluid to the left of the gate are at the middle of the fluid layers to the right of the gate and *vice versa*. Both fluid bodies are stably stratified, such that $\rho_1 > \rho_2 > \dots > \rho_{12}$, and the density step between vertically adjacent layers,

$\Delta\rho$, is everywhere equal, (see figure 5.2).

When the gate is removed at $t = 0$, we expect these layers to interleave at a constant velocities after a brief period of acceleration. This interleaving process should involve five interfacial intrusions and one boundary current propagating in both the rightward and leftward direction.

This system can be considered to consist of 11 boundary gravity currents exchanges, each in a fluid of height d subject to a local reduced gravity $g'_{RL} \equiv g \frac{(\rho_R - \rho_L)}{\rho_0}$, where ρ_R and ρ_L refer to the densities of the right and left fluids within that layer. In this system, there are 10 horizontal lines, one at the initial height of each density interface, above and below which the flow is a symmetric reflection over a vertical distance d . By (5.1), the speed of each of these local intrusions should therefore be:

$$U = Fr_0 \sqrt{g'_{RL} d}, \quad (5.6)$$

When the densities of each layer are the average of its two horizontally adjacent neighbors (e.g. $\rho_3 = (\rho_2 + \rho_4)/2$) throughout, g'_{RL} is everywhere the same. Because the layer depths have been constrained to be equal, the speeds of individual intrusions are therefore also equal. In this “doubly symmetric” system of interleaving interfacial gravity currents, we expect the two boundary currents and the ten interfacial intrusions to propagate at the same speed.

Each of the ten interfacial intrusions propagates into a two-layer ambient that can be considered to have an interface height of d and a total depth of $2d$. By (5.5), the density of the intruding fluid does not affect the IfGC speed because the receiving fluid layers are of equal heights. The local IfGC speed is therefore,

$$U_{local} = Fr_0 \frac{1}{2} \sqrt{g'_\Delta 2d}, \quad (5.7)$$

where $g'_\Delta \equiv g \frac{\Delta\rho}{\rho_0}$ is the local reduced gravity (e.g. intruding fluid from layer 3 experiences a reduced gravity defined by the density difference between layers 2 and 4). The system has been constrained such that $\Delta\rho$ is the same at every vertical density interface, and by (5.7), the IfGC speeds should therefore also be the same.

In the “triply symmetric” case, $\delta\rho = 0$, and the average or bulk density of the left-hand fluid is equal to that of the right-hand fluid. However, perturbing all

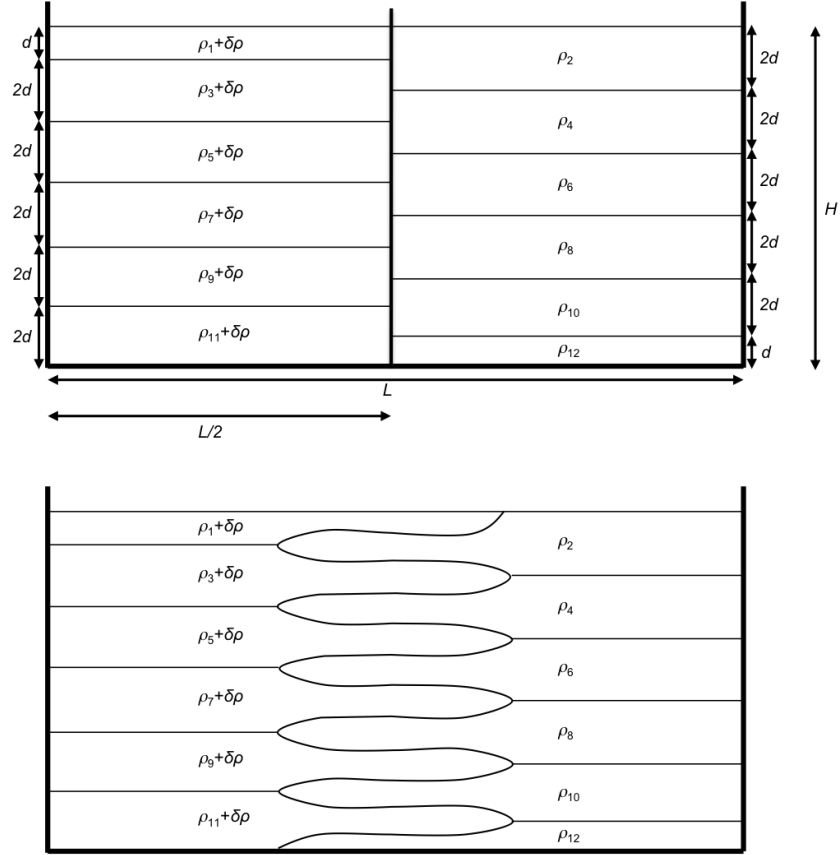


Figure 5.2: Schematic showing the initial conditions (above) for a lock-release of ten interleaving interfacial intrusions. In each of the two stably stratified fluids, there are six layers: one of thickness d and five of $2d$. There is a consistent density difference of $\Delta\rho$ between vertically adjacent layers. In the “triply symmetric” case, where $\delta\rho = 0$ each layer density is the average of the densities of its two horizontally adjacent neighbors and there is no bulk density difference between the fluids to the right and left of the gate. We deviate away from this equilibrium case by increasing the density of each of the left-hand fluid layers (left) by a consistent amount $\delta\rho$. At time $t = 0$, the gate is removed, and the layers interleave at constant velocities (below). For the “triply symmetric” case (shown), all currents interleave at the same observed speed.

left-hand fluid layer densities by $\delta\rho$ creates a bulk density difference of $\delta\rho$ between the two sides of the gate. This perturbation ranges from the equilibrium case $\delta\rho = 0$ to the case where the intruding fluid is of the same density as the lower-layer $\delta\rho = \frac{1}{2}\Delta\rho$. We hypothesize that there is background exchange flow associated with this net density difference that can be superimposed on the locally determined speeds of the individual intrusions (5.7). For simplicity, we argue that,

$$U_{obs} = U_{local}(\Delta\rho) + u_s(\delta\rho, z) \quad (5.8)$$

where U_{obs} is the observed current speed in the laboratory frame of reference and u_s is the background flow. Note that U_{local} does not depend on $\delta\rho$, but instead on $\Delta\rho$, which remains constant as we perturb each layer depth equally by $\delta\rho$.

Given that the interleaving stratification will likely suppress any larger scale overturning, we anticipate this background flow to be a shear flow. We anticipate this flow to scale similarly to a simple boundary gravity current, where dimensional analysis yields:

$$u_s(z) \sim \sqrt{g'_\delta H}, \quad (5.9)$$

where $g'_\delta \equiv g \frac{\delta\rho}{\rho_0}$ is the average reduced gravity between the two fluids. Here the background speed varies as the square root of the density difference.

5.4 Methods

5.4.1 Numerical simulations

Direct numerical simulations were conducted in two dimensions for a ten IfGC (and a five IfGC) system at eleven values of $\delta\rho/\Delta\rho$ equally spaced between 0 and 0.5. Reynolds numbers of the “triply symmetric” intrusions were in excess of 1.5×10^3 .

Simulations were conducted in a 2-dimensional domain of 366 cm length and 38.5 cm (20 cm) height. A uniform grid of 1024 x 512 points was used to discretize two symmetric 183 x 38.5 (20 cm) lock releases reflected about a central vertical line of symmetry (Sutherland *et al.* [30]). A division between the two stratifications was at $L_{lock} = 91.5$ cm in each simulated domain. The density was

varied between $\rho = 1.000$ and 1.100 g cm^{-3} , at intervals of 9.1 g cm^{-3} , resulting in a density step between vertically adjacent layers of $\Delta\rho = 18.2 \text{ g cm}^{-3}$. The central (left-hand in the laboratory frame) fluid of all densities was marked with a passive tracer.

A slightly modified version of the open source DNS algorithm Diablo (full details available at <http://renaissance.ucsd.edu/fccr/software/Diablo.html>) was used to solve the 2-D, incompressible Boussinesq equations, where the kinematic viscosity $\nu = 0.01 \text{ g cm}^{-3}$ and a Schmidt number, $Sc = 1$ (see Härtel *et al.* [35]) for justification of the increased molecular diffusivity). Symmetry about the back endwall of the left-hand fluid allowed periodic boundary conditions and therefore for the spectral evaluation of flow variables in the horizontal direction. To minimize Gibbs phenomenon, density steps in the horizontal direction were initially smoothed with a hyperbolic tangent profile; vertical density profiles were not smoothed. Vertical derivatives were evaluated using second-order centered finite differences. Boundary conditions were no-slip at the upper and lower fluid surfaces. The flow was set into motion at $t = 0$ and allowed to progress until interfacial waves encountered the ends of the domain at $t = \frac{L/2}{\sqrt{g'_{UL}h}}$. Only vertical diffusive terms were treated implicitly. The flow was advanced with a combination of a third-order, low-storage Runge-Kutta-Wray scheme and a Crank-Nicholson scheme at $\Delta t = 0.001 \text{ s}$.

We recovered density, ρ , velocity, \mathbf{u} , and passive tracer concentration, C fields at 0.5 s intervals. A tracer concentration greater than 50% of the left-hand fluid was used to identify left-hand fluid, and estimate its horizontal position. Tracking the individual front positions over time provided a measure of current speeds.

5.4.2 Laboratory Experiments

Laboratory experiments on a five IfGC systems were performed for $\delta|\rho/\Delta\rho = [0.00, 0.13, 0.24, 0.28, 0.34, 0.41] \pm .01$. Reynolds numbers of the “triply symmetric” interfacial gravity currents were in excess of 1.5×10^3 .

The experimental channel was 182 cm long, 23 cm wide, and 30 cm deep, with a vertical gate dividing the tank midway from either endwall. Sodium chloride

was added to water to vary the density between 1.010 and 1.070 g cm^{-3} . Sponge floats were used to fill both sides of the gate simultaneously to $H = 21 \text{ cm}$ depth. To the left of the gate, the stratification consisted of three layers of equal thickness $h = 7 \text{ cm}$. To the right of the gate, layers at the upper and lower boundaries were $h = 3.5 \pm 0.2 \text{ cm}$ thick and two intermediate layers were $h = 7 \pm 0.2 \text{ cm}$. The density step between all vertically adjacent layers was $\Delta\rho = 0.020 \text{ g cm}^{-3} \pm 0.001$. Interface thicknesses were observed to be less than 0.3 cm . Water samples were drawn every $2 \pm 0.2 \text{ cm}$ in height from both fluids, and the densities were verified with an Anton-Paar 5000 DMA density meter with an accuracy of $10^{-8} \text{ kg m}^{-3}$.

The experiments were illuminated by a vinyl light sheet placed against the back wall of the channel. A CCD camera (1390×1024 pixel resolution) was positioned normal to, and 5 m away from, the front wall. Sucrose-based food coloring, with a molecular diffusion coefficient approximately one-third that of sodium chloride, was added to the left-hand-fluid as a passive tracer of density.

Removing the gate vertically set the two fluids into motion. Images of the current were recorded directly onto a PC via DigiFlow software (Dalziel [34]) at twelve frames per second. The front position of each individual current was tracked in time using MATLAB. A linear regression was used to determine the U_{obs} once the individual fronts had accelerated to a constant speed.

5.5 Results

5.5.1 Five interleaving interfacial gravity currents

Our initial investigations into interleaving currents involved a system of five interleaving interfacial gravity currents, where three interfacial gravity currents propagated rightward, and two interfacial gravity currents and two boundary currents propagated leftward, (see figure 5.3). All interleaving currents were observed to reach a constant speed after a brief period of acceleration. The interleaving IfGCs in the “triply symmetric” cases for both the laboratory and the numerical simulations displayed symmetry about the respective density interfaces over a vertical distance d and traveled at the speed predicted by (5.5). Increasing the density

of the fluid to the left of the gate by $\delta\rho$ creates a linear variation in the observed speeds of the intrusions u_{obs} with height z . As the density perturbation increases, the thickness of the intrusions is observed to increase until becoming a block-like structure at $\delta\rho = 0.5$.

There is good agreement between the laboratory and numerical images for the five IfGC system (figure 5.4). The evident differences are caused by removing the gate vertically in the experiments, which results in a time delay in the release of the individual currents that increases with height, and also in the introduction of interfacial waves seen in the dyed layers of the left-hand fluid.

Individual speeds in this five IfGC system significantly influenced by friction at the boundaries. Though not immediately evident in these images, the boundary gravity currents and interfacial gravity currents interacting sharing an interface with boundary gravity currents are affected. This is more evident in the ten layer experiments (see for example figures 5.5 and 5.8), as the position and speed of the two currents nearest each boundary are substantially different than the intermediate IfGCs.

Though more difficult to discern in the experiment images, there is a leftward boundary gravity current along the upper fluid surface that increases in speed and size as the density perturbation increases. As there is no reciprocal boundary gravity current propagating rightward along the bottom of the tank, this represents an asymmetry and a sagging of the left-hand fluid relative to the right-hand fluid.

In an effort to avoid error introduced by the removal of the gate in experiments and to minimize the affects of drag and the complexity introduced by the boundary current asymmetry and we chose to pursue numerical models of a ten interleaving IfGC system.

5.5.2 Ten interleaving interfacial gravity currents

In this section, we present our numerical results from a system of ten interleaving IfGCs. As in the five IfGC case, all individual interfacial gravity currents were observed to reach a constant velocity phase (even if the current was station-

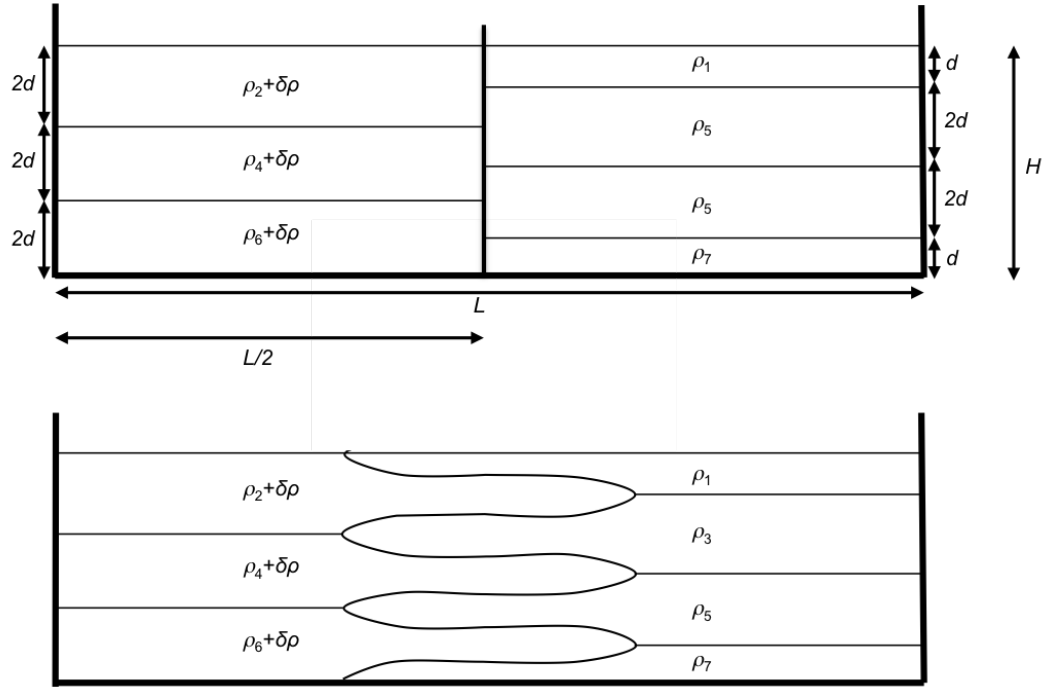


Figure 5.3: Schematic showing the initial conditions (above) for a lock-release of five interleaving interfacial intrusions. To the left of the gate, there are three layers of thickness $2d$. To the right of the gate, there are two intermediate layers of thickness $2d$ and two-layers at the boundaries of thickness d . There is a consistent density difference of $\Delta\rho$ between vertically adjacent layers. In the “triply symmetric” case, where $\delta\rho = 0$ each layer density is the average of the densities of its two horizontally adjacent neighbors and there is no bulk density difference between the fluids to the right and left of the gate. We deviate away from this equilibrium case by increasing the density of each of the left-hand fluid layers (left) by a consistent amount $\delta\rho$. At time $t = 0$, the gate is removed, and the layers interleave at constant velocities (below). For the “triply symmetric” case (shown), all currents interleave at the same observed speed.

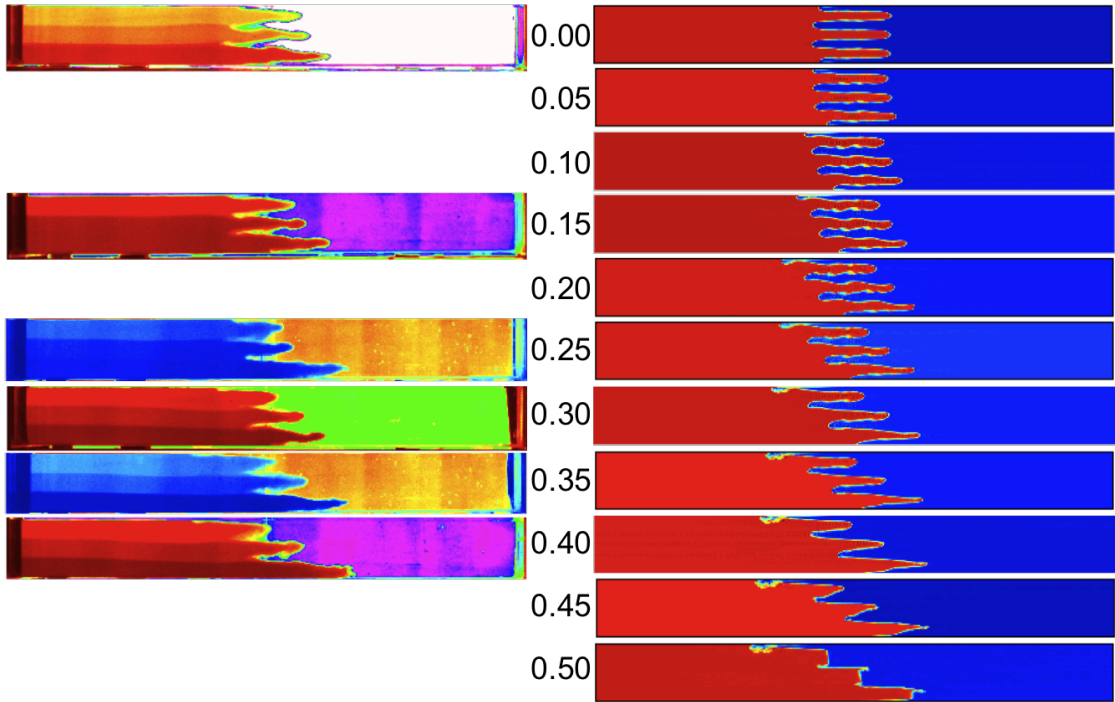


Figure 5.4: Corresponding images from the laboratory experiments and the numerical experiments over the range of $\delta\rho/\Delta\rho$ at $t = 6s$, showing excellent qualitative and quantitative agreement in intrusion shape and evident background shear flow between the experimental results and the numerics.

ary) after a brief period of adjustment and acceleration. The speed and shape of these intrusions was observed to vary as the average density of the fluid to the left of the gate was increased relative to the average density of the fluid to the right of the gate (see figure 5.5).

In the ‘triply symmetric’ case, where $\delta\rho/\Delta\rho = 0$, the intrusions are each symmetric about the interface along which they propagate. The $x - t$ diagram in figure 5.6 shows that these intrusions travel at a constant speed, the same to within two percent, and closely match the theoretical two-layer IfGC speed predicted by (5.4) shown as the dashed line. As the density of the fluid to the left of the intrusion increases, the shapes and speeds of the individual intrusions change (figure 5.5). Above the half-height of the experiment ($z = 19.25$), increasing $\delta\rho/\Delta\rho$ causes a decrease in the speed of rightward propagating currents and an increase in the speed of the leftward propagating currents relative to the equilibrium case. The converse is true below the half-height of the experiments. This variation in front speed appears to vary linearly with height.

Figure 5.7 presents plots of the observed velocity u_{obs} of the individual IfGC fronts as a function of the non-dimensional density perturbation. Boundary currents and the IfGCs directly contacting them are omitted in this figure. By experimental design, there is symmetry between the rightward propagating currents, (IfGCs 3, 5, 7, 9), and the leftward propagating currents, (IfGCs 4, 6, 8, 10). For the equilibrium case $\delta\rho/\Delta\rho = 0$ the speeds are all equal. All currents have a significant decrease in velocity relative to the equilibrium IfGC velocities at high density perturbations, with some fronts becoming stationary or reversing direction for $\delta\rho/\Delta\rho > 0.4$. For intermediate ranges, the speeds of IfGCs nearer the boundaries (currents 3 and 10) show an increase in magnitude. The predicted U_{local} is plotted as a dashed line for reference.

Plotting the intrusion speeds versus the heights of the interfaces along which they intrude in figure 5.8, we see that the velocity of the rightward and leftward propagating currents varies linearly with height for currents 3 through 10 over the entire range of density perturbation. For each value of $\delta\rho/\Delta\rho$, we fit lines to these velocity profiles of the leftward and rightward propagating velocities by

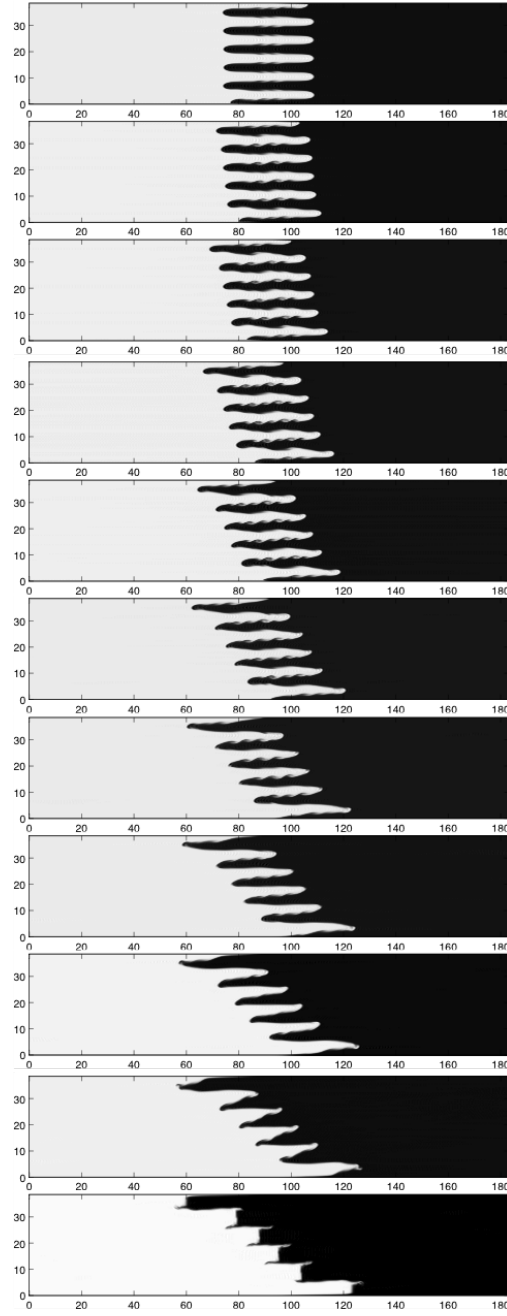


Figure 5.5: Snapshots of the simulation tracer fields at $t = 7s$. From top to bottom, $\delta\rho/\Delta\rho = [0, 0.05, 0.10, 0.15, 0.20, 0.25, 0.30, 0.35, 0.40, 0.45, 0.50]$. As $\delta\rho/\Delta\rho$ increases, the rightward IfGCs sink relative to the interface along which they propagate, while the leftward propagating IfGCs rise relative to the interface. For intrusions in both directions, the surface of the intruding fluid nearest the interface flattens with increasing density perturbation, while the opposite surface of the intrusion becomes more angled towards the vertical. $\delta\rho/\Delta\rho = 0$ shows interleaving symmetric intrusions of the same velocities in both directions, while $\delta\rho/\Delta\rho = 0.5$ shows step-function profile with height.

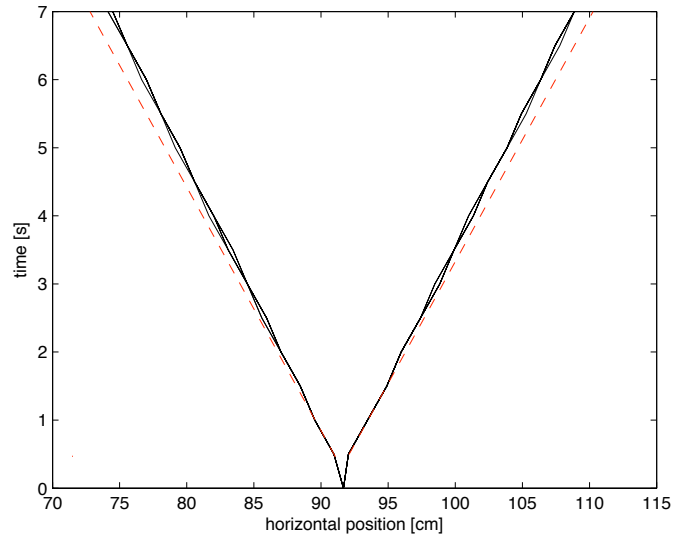


Figure 5.6: $x - t$ diagram of the ten $\delta\rho/\Delta\rho = 0.0$ interleaving IfGCs (solid black lines) compared to the theoretical 'triply symmetric' IfGC speed (dashed red lines) predicted from local parameters, $U_{local} = Fr_{\frac{1}{2}} \sqrt{g'_{\Delta} 2d}$ with no background shear flow $u_s = 0$. All five curves in both directions are plotted, but are so close in position that they are indistinguishable.

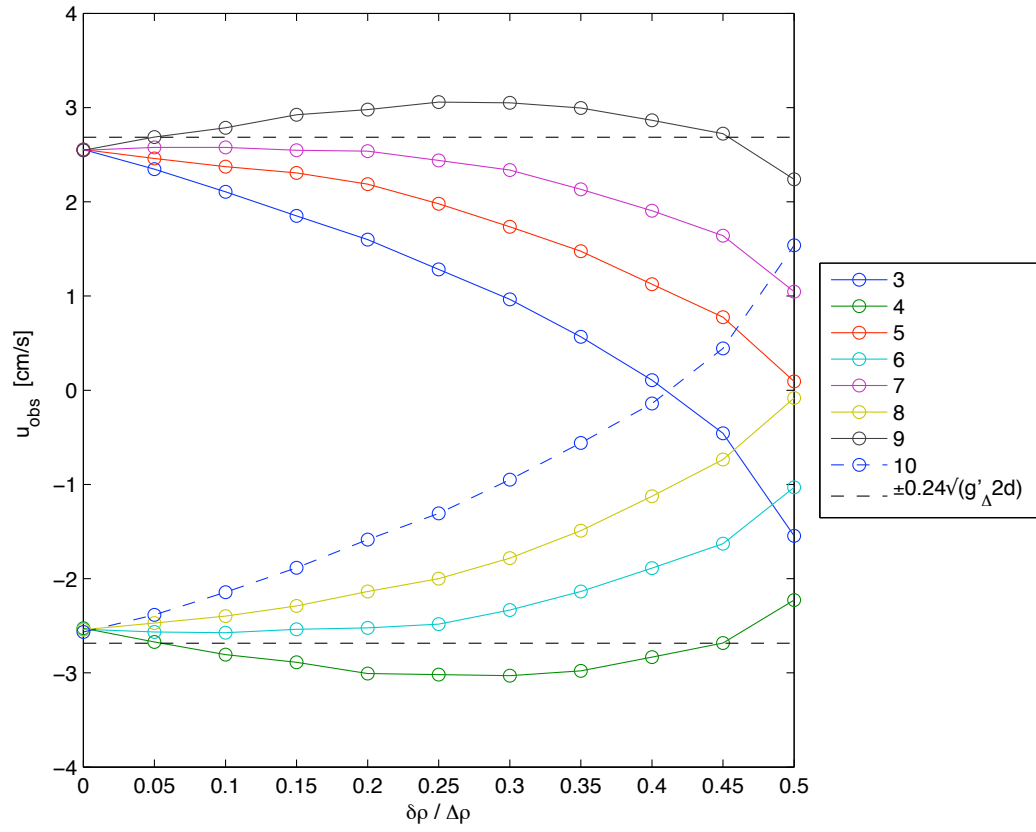


Figure 5.7: The variation in the observed velocity u_{obs} as a function of the density perturbation $\delta\rho/\Delta\rho$. The theoretical individual current speed U_{local} is marked as the dashed black line. The observed velocity u_{obs} does not display the expected $\sqrt{\delta\rho}$ dependence.

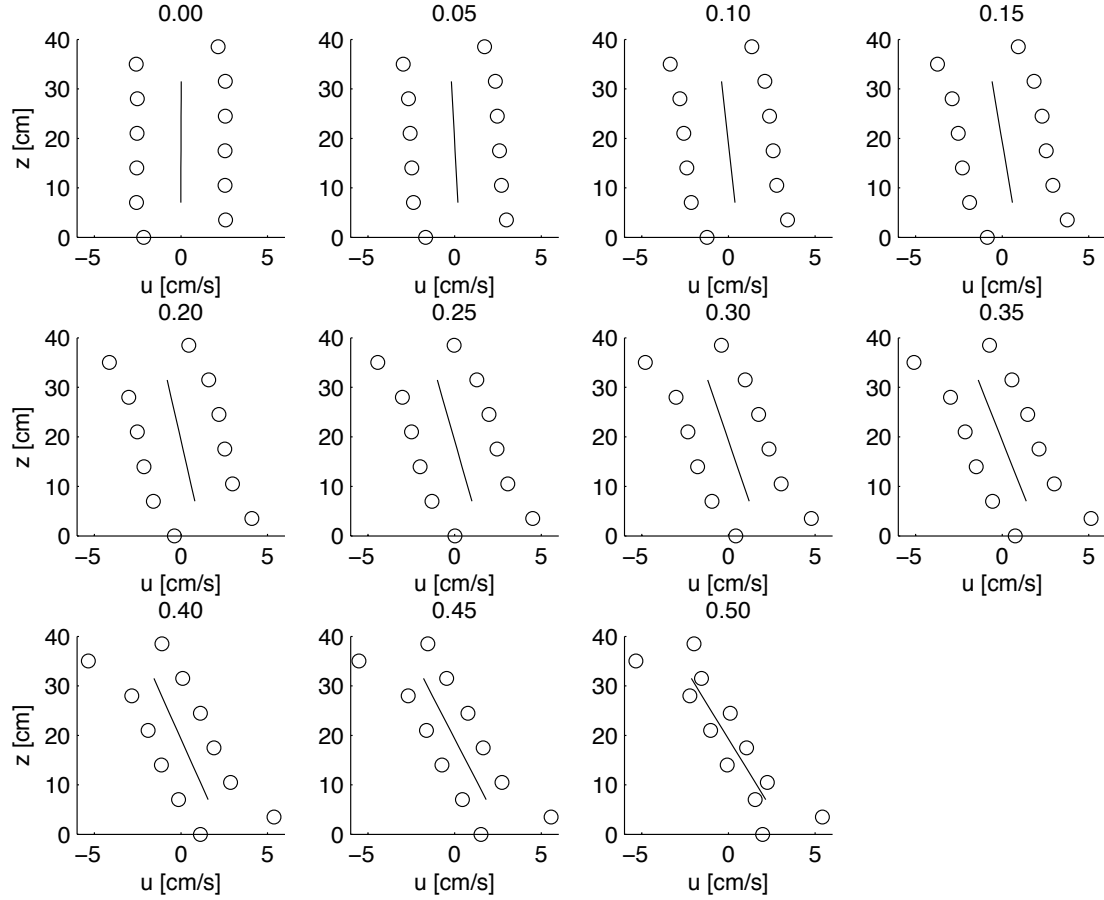


Figure 5.8: Observed velocities u_{obs} of the individual interleaving IfGCs as a function of height. A line is fitted to the IfGC speeds (away from the boundaries) as an estimate of the background shear u_s . The background velocity is observed to increase in magnitude as the difference in the average densities of the two fluids increases. The individual IfGC velocities decrease in their difference from the background shear flow as the density perturbation $\delta\rho/\Delta\rho$ increases.

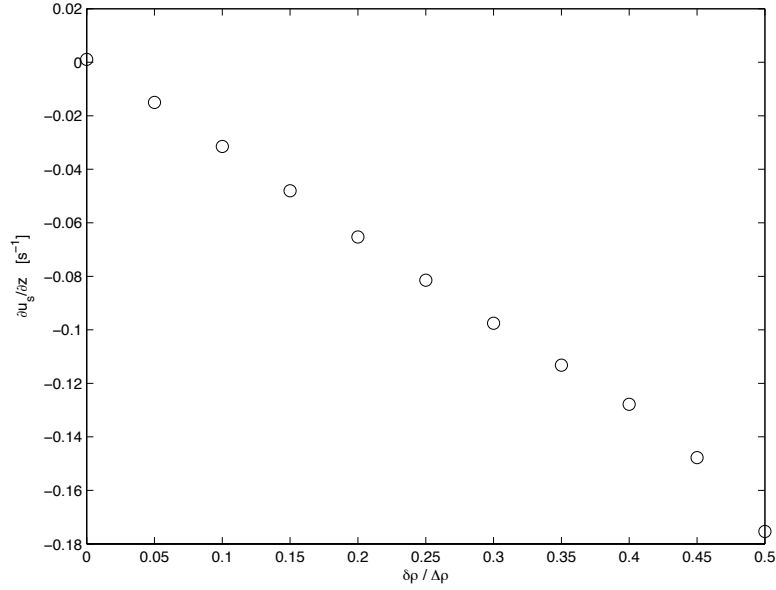


Figure 5.9: A plot of the fitted shear velocity gradient $\partial u_s / \partial z$ as a function of the density perturbation $\delta\rho / \Delta\rho$. The background shear is observed to vary linearly with the density perturbation.

linear regression. Taking the average of the two slopes and the two intercepts, we obtained an estimate for the background shear flow u_s , plotted as continuous lines. The vertical gradient of the background shear velocity $\partial u / \partial z$ increases as the density perturbation increases, while the difference between the observed velocities u_{obs} and the shear velocity velocity u_s decreases.

The vertical gradient in shear velocity varies linearly with the density perturbation, as shown in figures 5.9 and 5.11. Figure 5.11 presents an estimate of the background shear velocity at the boundaries calculated from this gradient, and compares it to the predicted front velocity of a boundary gravity current between fluids of height H and a density difference $\delta\rho$ via (5.1). The two curves are similar in order of magnitude but differ in dependence on the density perturbation.

Because the observed velocity profiles are linear in z and symmetric about the fitted background shear flow profile, we take the mean difference between observed IfGC velocity u_{obs} and the estimated background shear flow u_s to be the local IfGC speed U_{local} . Though the equilibrium IfGC speed $U_{local}(\delta\rho / \Delta\rho = 0)$

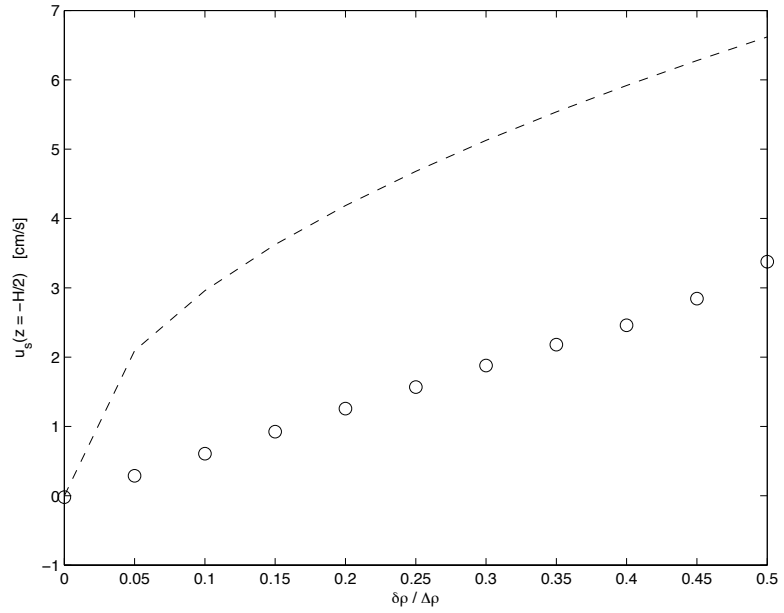


Figure 5.10: A plot of the fitted shear velocity calculated at $z/H = 0$ (circles) as a function of the density perturbation $\delta\rho/\Delta\rho$. The speed of an analogous gravity current based on (5.1) and the average densities of the two fluids is plotted as a dashed line.

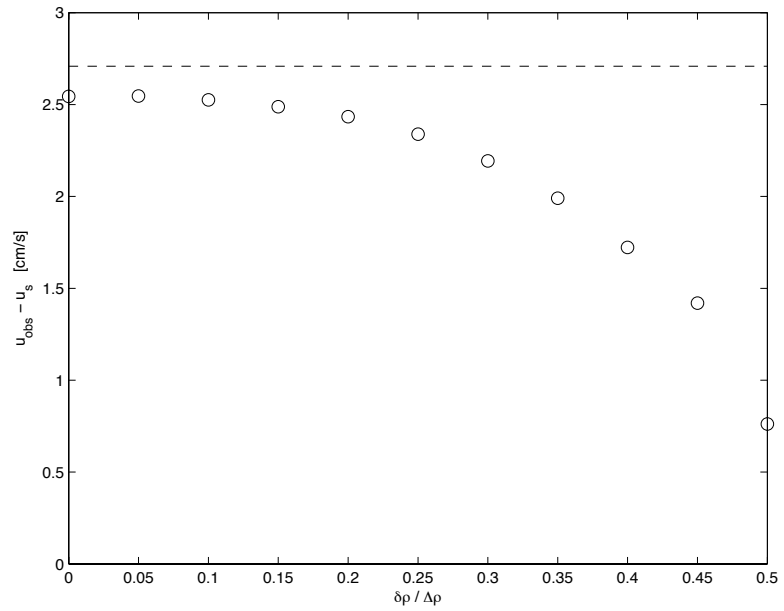


Figure 5.11: A plot of $u_{obs} - u_s$ as a function of $\delta\rho/\Delta\rho$ showing a quadratic decrease in speed with increasing density perturbation.

is near the speed predicted by (5.4), U_{local} varies with the density perturbation, decreasing nonlinearly with the increase in $\delta\rho/\Delta\rho$. The speed predicted by (5.4) is shown as a dashed line.

Figure 5.12 presents snapshots of the density field over the range of density perturbations at $t = 7$. The position of the individual currents marked by the black contour. Individual intrusions in the equilibrium case $\delta\rho/\Delta\rho = 0$ propagate along interfaces that are unperturbed by interfacial wave motion. Perturbing away from the equilibrium case, the presence of interfacial waves is immediately evident. The amplitude of these disturbances is observed to increase as the density perturbation increases.

5.6 Discussion

This chapter examines the interleaving process of two discretely stratified fluids. For simplicity, we have focused our attention on a highly idealized case in which there are an even number of interleaving intrusions. We have further restricted our scope to include only initial stratifications where the individual layer thickness are equal, density interfaces within one fluid are vertically staggered by half the layer thickness relative to the second fluid, and the density differences between vertical adjacent layers are equal. These restrictions were made to simplify the parameterization of the system, potentially allowing the reduction of the system to multiple interleaving IfGCs each behaving as the two-layer system described by Cheong *et al.* [6].

The system was then perturbed from equilibrium by increasing the density of each layer in the left-hand fluid by a fraction of the vertical density difference between layers, thereby increasing the density of the left-hand fluid relative to the right-hand fluid by the same fraction. This density perturbation was varied from the equilibrium case in which the density of the intruding is equal to the average of the two receiving fluid densities, to the case in which the density of the left-hand fluid layer matches that of the lower receiving layer within the right-hand fluid.

We hypothesized that the resulting flow would be a linear combination

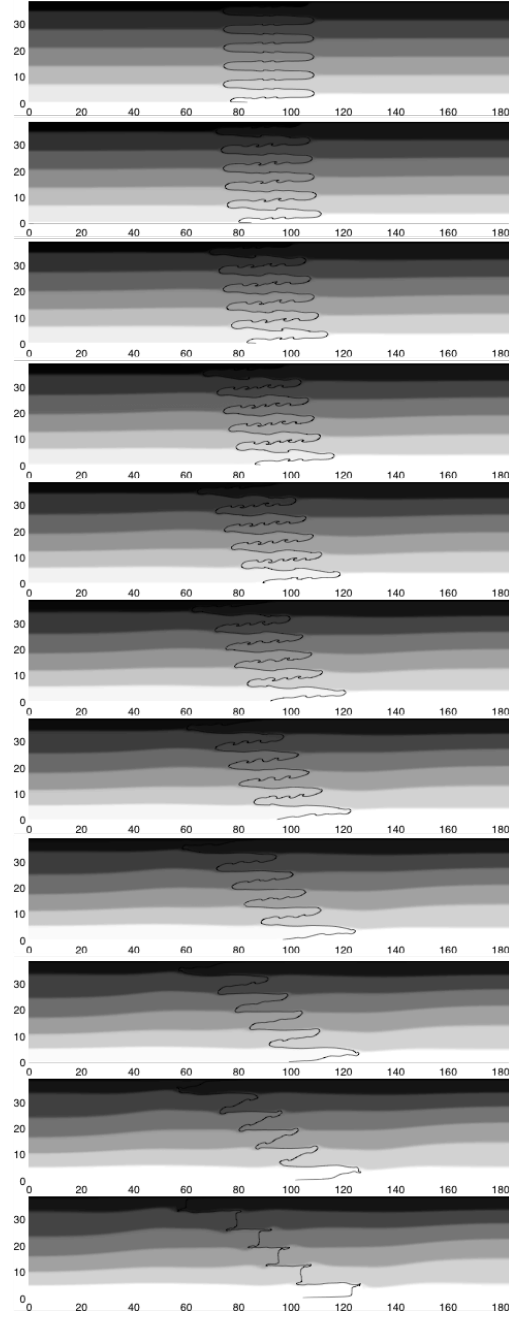


Figure 5.12: Snapshots of the simulation density fields at $t = 7s$, with contour of the passive tracer marking the location of the individual interleaving IfGCs. From top to bottom, $\delta\rho/\Delta\rho = [0, 0.05, 0.10, 0.15, 0.20, 0.25, 0.30, 0.35, 0.40, 0.45, 0.50]$. The “triply symmetric” case shows no displacement of the interfaces. However, simulations of $\delta\rho/\Delta\rho > 0$ show evidence of interfacial waves. The amplitude of these disturbances appears to increase with the density perturbation.

of a local intrusion speed $U_{local}(\Delta\rho)$ and a background shear flow $u_s(\delta\rho)$. From experiments and simulations by Cheong *et al.* [6] we expected the IfGC to be independent of the density perturbation $\delta\rho$ and therefore invariant in our system. From dimensional arguments, we further anticipated the background shear flow to vary with the square root of $\delta\rho$ as would a gravity current based on the total height and average densities of the two fluids. We conducted limited laboratory experiments and more extensive numerical simulations to investigate systems of five and ten interleaving IfGCs .

Locally and globally, these flows are Boussinesq: density differences between layers $\Delta\rho$ and between the right and left fluids $\delta\rho$ are small in comparison to any of the densities involved in the system. For this reason, we expect a symmetry in behavior about the individual interfaces and about the half-height $z = H/2$ of the fluids, were we to *decrease* the density of each left-hand fluid layer by $\delta\rho$. Explicitly, the rightward propagating currents would rise relative to the interfaces rather than sink, and the background horizontal velocities would reverse direction. Moving away from the equilibrium case to $\delta\rho < 0$ would produce U_{local} and u_s of the same magnitudes, but opposite signs. Systems consisting of an even number of IfGCs also possess *rotational* symmetry about $(x = L/2, z = H/2)$ at π . This additional symmetry prevents the sinking of the heavier stratification relative to the other, (as seen in subsection 5.5.1), which allowing data for both rightward and leftward propagating currents to be used interchangeably. For this reason, we concentrate on systems of an even number of interleaving interfacial gravity currents, choosing ten in an effort to minimize bias introduced by drag at the upper and lower boundaries.

In the “triply symmetric” or equilibrium case, the fluid layer depths are equal, the IfGC densities are the average of the horizontally adjacent fluid layers, and there is no net difference in density between the two fluids. As expected, the individual IfGCs each propagate at the same speed, there is no displacement of the interface upstream of the intrusions, and no background flow is evident. The speed of the individual fronts agrees well with predictions by Cheong *et al.* [6] for a single intrusion doubly symmetric equation (5.5).

Increasing the density perturbation $\delta\rho/\Delta\rho$ away from the equilibrium case, however, the observed velocities of the individual IfGC fronts do not behave according to our hypothesis (5.8), which implies $u_{obs} = A + B\sqrt{\delta\rho} z$, where A and B are constants and z is the initial height of the relevant interface. Instead, there appears to be a gradual slowing and or reversal of currents *at all heights* within the experiment. Though some IfGCs show a temporary increase in magnitude with increasing density perturbation, all currents eventually exhibit observed speeds u_{obs} slower than the individual intrusion speed U_{local} which was assumed to be invariant in the experiments.

By conservation of mass, the background shear flow u_s cannot directly account for this slowing of intrusion speeds with increasing density perturbation. Individual front speeds in both directions decrease in magnitude over the entire range of height. However, it may still be possible to consider the local and background flows separately. Profiles of the individual rightward and leftward front speeds for each simulation exhibit the same linear dependence of velocity on vertical position and show a consistent difference between the observed current speeds and the fitted background flow over the range of intermediate heights.

Considering first the contribution of the background flow, we note that there is a linear dependence of the magnitude of the shear $\partial u/\partial z$ on the density perturbation. This is in contrast to the form expected by (5.9), where the background shear flow depends on the square root of the density perturbation. As the individual currents become more asymmetric, the magnitude of the background shear flow speed goes as the square of the contribution hypothesized in section 5.3.

However, the observed flow still decreases in speed as density perturbation increases, indicating that there is a corresponding slowing of the individual IfGC speeds. Indeed, moving away from the equilibrium case there is a decrease in the difference between the observed velocities and the estimated background shear flow velocity at each height. Plots of this difference as a function of density perturbation reveal a strong nonlinear dependence, with individual IfGC speeds decreasing to approximately twenty percent of the equilibrium values over the range investigated.

We suggest that this difference is due to the increasing magnitude of inter-

facial waves upstream of the intrusions. A rigorous analytical model of an IfGC in a two-layer ambient fluid by Flynn & Linden [22] found that the upstream interfacial wave modulates the intrusion speed by altering the upstream conditions. By continuity, the sinking of “heavy” IfGCs displaces mass in the lower-layer, which in turn elevates the interface upstream of the wave, decreasing the net horizontal density gradient over the height of the front. This results in a decrease in the hydrostatic pressure differences locally driving flow, thereby slowing the current.

In a system of interleaving IfGCs, this slowing effect of upstream interfacial waves is compounded by the existence of multiple layers. In Flynn & Linden’s [22] model, only the sinking or rising of a current caused the displacement of the upstream interface. In a system of interleaving intrusions, interfacial waves are coupled. Mass in each layer is displaced not just by the advancement of a “heavy” or “light” current, but also by waves along both its upper and lower boundaries. The upstream wave therefore has a correspondingly greater amplitude than the analogous two-layer experiment, proportionally decreasing the speed of the current.

The hydrostatic pressure differences between the two stratified fluids store the potential energy of the system, which is converted to the kinetic energy of the ensuing flow in the form of the interleaving IfGCs, the background flow, turbulence, and wave motion. We suggest that the coupling of waves at multiple interfaces inhibits the interleaving process, which maintains a net horizontal pressure gradients between the two fluids, thereby increasing the rate of energy transfer into the background shear flow. We leave validating such a balance to future studies.

Chapter 6

Conclusions and summary of present contribution

This dissertation explores the dynamics of constant velocity gravity-driven intrusions in stratified fluids, focusing on intrusions in which the dynamics are governed by the balance between buoyancy and inertial forces. We investigated well-mixed and stratified intrusive gravity currents propagating a linearly stratified ambient fluid and a system of interleaving interfacial gravity currents.

Intrusive gravity currents excite waves in the continuous ambient stratification. The front speed of intrusions in a continuously stratified fluid is always subcritical to internal wave propagation speeds. All well mixed intrusive gravity currents in a linearly stratified ambient fluid are subcritical to mode-1 internal wave motion (Bolster *et al.* [4]), but only some are subcritical to mode-2 wave propagation. Vertical profiles of mode-1 horizontal velocity correspond closely to velocity profiles generated in and above boundary gravity currents. Intrusions generate horizontal velocity profiles over the height of the fluid that closely resemble the horizontal velocity structure of mode-2 internal waves.

Through synthetic schlieren laboratory experiments and two-dimensional direct numerical simulations of lock releases, chapter 3 explored the role of intrusion density in the structure, momentum, and energy of the wave field within an upstream control volume. We found that this wave field consisted of horizontally propagating internal long wave modes well described linear wave theory. Both level of neutral buoyancy and the speed vary with the intrusion density as predicted by Bolster *et al.*, and each has an observable effect on the excitation of modes-1 and -2. The momentum of the upstream wave field is of the same order of magnitude as the momentum of the IGC, while the energy lost to the upstream wave field

was found to be on the same order as losses to dissipation.

There is no existing analytical model of well-mixed intrusions into linearly stratified ambient fluid. A heuristic energy scaling model by Bolster *et al.* in the spirit of Cheong *et al.* [6] shows excellent agreement with experiments and simulations, but offers little insight into the dynamics of the flow. Our work describing the systematic disturbance of the density field, and the upstream transfer of momentum and energy is meant to be the foundation of future analytical models describing this flow, similar to Flynn & Linden’s [22] model incorporating interfacial waves into a model of interfacial gravity current propagation.

In chapter 4 we developed a heuristic model similar to those of Cheong *et al.* and Bolster *et al.* to investigate the effect of stratification within an intrusion. All natural fluid bodies stratify. Vertical stratification within an intrusion represents a reduction in the horizontal density gradients at the front relative to a well mixed intrusion. This in turn is a reduction in the baroclinic torque locally driving the current.

We present the first model predicting the front speed of an intrusion propagating from one constantly stratified fluid into another constantly stratified fluid of a different buoyancy frequency, limiting our scope to the case where the mean densities of the two fluids are equal. As in Cheong *et al.* we scaled the intrusion velocity by the Available Potential Energy of the system and empirical measurements (of intrusion thickness). Appropriate limits were taken from the work of Bolster *et al.* and inspection. The heuristic model developed shows excellent agreement with laboratory experiments and two-dimensional direct numerical simulations we conducted over the parameter range.

We intend the energy scaling model presented in chapter 4 to provide a foundation for future analytical work describing the dynamics of intrusions between stably stratified fluids. An accurate Benjamin-style [5] model of such a flow would need to incorporate the adjustment of the density field *within* the intrusion as well as in the ambient fluid (noted in chapter 3) in the balance of mass, momentum, and energy.

Contrary to the case presented in chapter 4, adjacent *discrete* density strat-

ifications have the potential to interleave as a system of interfacial gravity currents. Single interfacial gravity currents in a two-layer ambient are well understood. In the case where the two-layer depths are equal the front speed Cheong *et al.* shows that the front speed of the intrusion is independent of the density of the intrusion. We attempted to extend this finding to a highly idealized case, using primarily two-dimensional direct numerical simulations of systems of an even number of interleaving intrusions.

Equally perturbing the density of each layer to one side of gate, increases the average density of that fluid relative to the fluid to the other side of the gate. By extension from the two-layer model, the local IfGC speed should vary only with the density difference between vertically adjacent layers. Preserving this difference, we vary the average density of one fluid, hypothesizing that this difference will be expressed as a background shear flow that scales as a boundary gravity current.

Increasing the average density of one fluid relative to the other does generate a background shear flow. However, this shear flow does not depend on the density as expected, and the individual intrusion speeds are found to vary with the density of the intrusion. We propose that the failure of our model is the inhibition of the individual currents by coupled interfacial waves. In the two-layer case, the role of these waves is to alter the upstream conditions slowing the current (Flynn & Linden [22]). The coupling of these waves across density layers would represent an increased slowing of these individual currents relative to the two-layer case. Slowing the individual currents would maintain bulk horizontal pressure gradients between the two stratifications, driving the background flow more strongly than anticipated a simple gravity current scaling.

Bibliography

- [1] O. Sigurjónsson, “Weather images: The Eyjafjallajökull ash cloud (Figure 2. The Eyjafjallajökull eruption plume rises above low cloud on 17 may 2010),” *Weather*, vol. 66, no. 2, p. 42, 2010.
- [2] C.-S. Yih, *Dynamics of Nonhomogeneous Fluids*. Macmillan Company, New York, 1st ed., 1965.
- [3] B. D. Maurer, D. T. Bolster, and P. F. Linden, “Intrusive gravity currents between two stably stratified fluids,” *J. Fluid Mech.*, vol. 647, no. -1, pp. 53–69, 2010.
- [4] D. T. Bolster, A. Hang, and P. F. Linden, “The front speed of intrusions into a continuously stratified medium,” *J. Fluid Mech.*, vol. 594, pp. 369–377, 2008.
- [5] T. B. Benjamin, “Gravity currents and related phenomena,” *J. Fluid Mech.*, vol. 31, no. 02, pp. 209–248, 1968.
- [6] H. B. Cheong, J. J. P. Kuenen, and P. F. Linden, “The front speed of intrusive gravity currents,” *J. Fluid Mech.*, vol. 552, pp. 1–11, 2006.
- [7] J. E. Simpson and P. F. Linden, “Frontogenesis in a fluid with horizontal density gradients,” *J. Fluid Mech. Digital Archive*, vol. 202, pp. 1–16, 1989.
- [8] D. T. Georgi, “Finestructure in the antarctic polar front zone: its characteristics and possible relationship to internal waves,” *Journal of Geophysical Research*, vol. 83, pp. 4579 – 4588, 1978.
- [9] M. H. Alford, M. C. Gregg, and E. A. D’Asaro, “Mixing, 3d mapping, and lagrangian evolution of a thermohaline intrusion,” *J. Phys. Oceanogr.*, vol. 35, pp. 1689 – 1711, 1980.
- [10] R. W. Griffiths and E. J. Hopfinger, “The structure of mesoscale turbulence and horizontal spreading at ocean fronts,” *Deep Sea Research Part A. Oceanographic Research Papers*, vol. 31, no. 3, pp. 245 – 269, 1983.
- [11] J. E. Simpson, *Gravity Currents*. Cambridge University Press, 2nd ed., 1997.

- [12] J. . Wu, “Mixed region collapse with internal wave generation in a density-stratified medium,” *J. Fluid Mech.*, vol. 35, pp. 531–544, 1969.
- [13] R. Amen and T. Maxworthy, “The gravitational collapse of a mixed region into a linearly stratified fluid,” *J. Fluid Mech.*, vol. 96, no. 1, pp. 65–80, 1980.
- [14] P. C. Manins, “Intrusions into a stratified fluid,” *J. Fluid Mech.*, vol. 74, pp. 547–560, 1973.
- [15] T. W. Kao, H.-P. Pao, and C. Park, “Surface intrusions, fronts, and internal waves: a numerical study,” *J. Geophys. Research*, vol. 83, no. C9, pp. 4641 – 4650, 1978.
- [16] J. Y. Holyer and H. E. Huppert, “Gravity currents entering a two-layer fluid,” *J. Fluid Mech.*, vol. 100, no. 04, pp. 739–767, 1980.
- [17] B. R. Sutherland, P. J. Kyba, and M. R. Flynn, “Intrusive gravity currents in two-layer fluids,” *J. Fluid Mech.*, vol. 514, pp. 327–353, 2004.
- [18] J. W. Rottman and J. E. Simpson, “Gravity currents produced by instantaneous release of a heavy fluid in a rectangular channel,” *J. Fluid Mech.*, vol. 135, pp. 95–110, 1983.
- [19] R. J. Lowe, P. F. Linden, and J. W. Rottman, “A laboratory study of the velocity structure in an intrusive gravity current,” *J. Fluid Mech.*, vol. 456, pp. 33–48, 2002.
- [20] R. E. Britter and J. E. Simpson, “A note on the structure of the head of an intrusive gravity current,” *J. Fluid Mech.*, vol. 112, pp. 459–466, 1981.
- [21] F. de Rooij, P. F. Linden, and S. B. Dalziel, “Saline and particle-driven interfacial intrusions,” *J. Fluid Mech.*, vol. 389, pp. 303–334, 1999.
- [22] M. R. Flynn and P. F. Linden, “Intrusive gravity currents,” *J. Fluid Mech.*, vol. 568, pp. 193–202, 2006.
- [23] T. Maxworthy, J. Leilich, J. E. Simpson, and E. H. Meiburg, “The propagation of a gravity current into a linearly stratified fluid,” *J. Fluid Mech.*, vol. 453, pp. 371–394, 2002.
- [24] M. Ungarish and H. E. Huppert, “On gravity currents propagating at the base of a stratified ambient: effects of geometrical constraints and rotation,” *J. Fluid Mech.*, vol. 521, pp. 69–104, 2004.
- [25] B. R. Sutherland, A. N. F. Chow, and T. P. Pittman, “The collapse of a mixed patch in stratified fluid,” *Physics of Fluids*, vol. 19, no. 11, p. 116602, 2007.

- [26] J. E. Simpson and R. E. Britter, “The dynamics of the head of a gravity current advancing over a horizontal surface,” *J. Fluid Mech.*, vol. 94, pp. 477–485, 1979.
- [27] M. Ungarish and H. E. Huppert, “On gravity currents propagating at the base of a stratified ambient,” *J. Fluid Mech.*, vol. 458, pp. 283–301, 2002.
- [28] J. R. Munroe, C. Voegeli, B. R. Sutherland, V. Birman, and E. H. Meiburg, “Intrusive gravity currents from finite length locks in a uniformly stratified fluid,” *J. Fluid Mech.*, vol. 635, pp. 245–273, 2009.
- [29] A. H. Schooley and B. A. Hughes, “An experimental and theoretical study of internal waves generated by the collapses of a two-dimensional mixed region in a density gradient,” *J. Fluid Mech.*, vol. 51, pp. 159–175, 1972.
- [30] B. R. Sutherland, M. R. Flynn, and K. Dohan, “Internal wave excitation from a collapsing mixed region,” *Deep Sea Research, Part II*, vol. 51, no. 25-26, pp. 2889–2904, 2004.
- [31] B. L. White and K. R. Helfrich, “Gravity currents and internal waves in a stratified fluid,” *J. Fluid Mech.*, vol. 616, pp. 327–356, 2008.
- [32] G. Oster, “Density gradients,” *Sci. Am.*, vol. 213, pp. 70–76, 1965.
- [33] S. B. Dalziel, G. O. Hughes, and B. R. Sutherland, “Whole-field density measurements by ‘synthetic schlieren’,” *Experiments in Fluids*, vol. 28, pp. 322–335, 2000.
- [34] S. B. Dalziel, *Digiflow Manual*, 1st ed., 2004.
- [35] C. Härtel, E. Meiburg, and F. Necker, “Analysis and direct numerical simulation of the flow at a gravity-current head. part 1. flow topology and front speed for slip and no-slip boundaries,” *J. Fluid Mech.*, vol. 418, pp. 189–212, 2000.
- [36] J. O. Shin, S. B. Dalziel, and P. F. Linden, “Gravity currents produced by lock exchange,” *J. Fluid Mech.*, vol. 521, pp. 1–34, 2004.
- [37] K. M. Faust and E. J. Plate, “Experimental investigations of intrusive gravity currents entering stably stratified fluids,” *J. of Hydraulic Research*, vol. 22, no. 5, pp. 315–325, 1984.
- [38] M. Ungarish, “Intrusive gravity currents in a stratified ambient: shallow-water theory and numerical results,” *J. Fluid Mech.*, vol. 535, pp. 287–323, 2005.
- [39] R. I. Nokes, M. J. Davidson, C. A. Stepien, W. B. Veale, and R. L. Oliver, “The front condition for intrusive gravity currents,” *J. of Hydraulic Research*, vol. 0, no. 0, pp. 1–14, 2008.

- [40] Keulegan, “The motion of saline fronts in still water,” *Natl Bur. Stnd. Rep.*, vol. 5813, 1958.
- [41] D. T. Bolster, D. Tartakovsky, and M. Dentz, “Analytical models of contaminant transport in coastal aquifers,” *Adv. Water Resour.*, vol. 30, pp. 1962–1972, 2007.
- [42] A. Mehta, B. R. Sutherland, and P. J. Kyba, “Interfacial gravity currents: Part ii - wave excitation,” *Phys. Fluids*, vol. 14, pp. 3558–3569, 2002.
- [43] B. R. Sutherland and J. T. Nault, “Intrusive gravity currents propagating along thin and thick interfaces,” *J. Fluid Mech.*, vol. 586, pp. 109–118, 2007.
- [44] S. K. Ooi, G. Constantinescu, and L. Weber, “A numerical study of intrusive compositional gravity currents,” *Physics of Fluids*, vol. 19, no. 7, p. 076602, 2007.
- [45] M. R. Flynn, T. Boubarne, and P. F. Linden, “The dynamics of steady, partial-depth intrusive gravity currents,” *Atmosphere - Ocean*, vol. 46, no. 4, pp. 421 – 432, 2009.